Universidade Vigo

Departamento de Física Aplicada

Facultade de Ciencias do Mar

Universidade de Vigo

---

# ESTIMACIÓN MEDIANTE SIMULACIÓN MOLECULAR DE LAS PROPIEDADES INTERFACIALES DE FLUIDOS IMPLICADOS EN LA EXTRACCIÓN FORZADA DE GAS NATURAL

---

Memoria presentada por

**Jose Manuel Míguez Díaz**

para optar al Grado de

**Doctor por la Universidad de Vigo con Mención Internacional**

Vigo, Febrero de 2012

Universidade Vigo

José Luis Legido Soto, Catedrático de Física Aplicada, Manuel Martínez Piñeiro y Diego González Salgado, Profesores Titulares del Departamento de Física Aplicada de la Universidad de Vigo,

AUTORIZAN:

al Licenciado en Física **D. Jose Manuel Míguez Díaz** a presentar la memoria titulada: **"Estimación mediante simulación molecular de las propiedades interfaciales de fluidos implicados en la extracción forzada de gas natural"** que para optar al Grado de Doctor por la Universidad de Vigo con mención Internacional, realizó bajo nuestra dirección en el Departamento de Física Aplicada.

En Vigo, a 4 de diciembre de 2012

José Luis Legido Soto  Manuel Martínez Piñeiro  Diego González Salgado

CAMPUS DE VIGO
Teléfono 986 81 40 70 - Fax 986 81 40 69 - Facultade de Ciencias do Mar
Campus Universitario Lagoas Marcosende s/n
36310 VIGO- Pontevedra

A la memoria de mis Abuelos

# Agradecimientos

Quiero expesar mi agradecimiento a todas las personas que de un modo u otro me han ayudado y han hecho posible el desarrollo de esta Tesis:

En primer lugar, a mis directores, el Catedrático D. José Luis Legido Soto y los Profesores Titulares de Universidad, D. Diego González salgado y D. Manuel Martínez Piñeiro , especialmente a este último por haberme dado la oportunidad de realizar este trabajo y haberme ayudado, comprendido y animado en este largo trabajo.

Al grupo de personas que componen el laboratorio de TermoFísica de Ourense, el catedrático D. Luis Romaní Martínez y los profesores Titulares de Universidad, D. José Peleteiro Salgado, D. Gerardo Domarco Álvarez, D. Claudio Cerdeiriña, D. Jacobo Troncoso Casares y Dña. Clara Asunción Tovar Rodríguez por su amistad y los buenos momentos que compartimos durante mi paso por este departamento.

A todos los que han sido mis compañeros en el Departamento a lo largo de estos años, y con los que tan buenos ratos he pasado.

A toda la gente que conocí durante mis estancias en el Departamento de Física Aplicada de la Universidad de Huelva y en el Laboratoire des Fluides Complexes de la Université de Pau et des Pays de l'Adour, especialmente a los profesores Titulares de Universidad, D. Felipe Jimenez Blas y D. Bruno Mendiboure, por permitirme desarrollar en ellas gran parte de este trabajo.

Al programa de "Formación de Profesorado Universitario" dependiente del Ministerio de Ciencia e Innovación, beca $n^{\circ}$ AP2007-02172 por la financiación recibida.

A mis amigos, gracias por estar siempre ahí.

A mis padres y hermanos, por su apoyo incondicional.

A Paula, por todo.

Y a todas aquellas personas que hayan contribuido de alguna manera en la realización de este trabajo.

GRACIAS

# Contents

## CONTENTS

# List of Figures

## LIST OF FIGURES

## LIST OF FIGURES

# Chapter 1

# Introducción

## 1.1 Yacimientos no convencionales de gas natural

En la actualidad los combustibles fósiles siguen constituyendo uno de los pilares fundamentales en la producción de energía a escala global. Sin embargo, y a pesar de que esta posición predominante como principal fuente de producción no ha variado, sí que lo ha hecho en gran medida la estrategia de explotación y las técnicas extractivas. En este ámbito, se sigue produciendo un desarrollo constante, y se presentan sin cesar nuevas técnicas y avances científicos que han significado un notable progreso respecto a los procedimientos tradicionales. Los motivos que impulsan la innovación en este campo son diversos, pero tienen un peso fundamental el crecimiento de la demanda, especialmente por parte de países de economía emergente, y el agotamiento de muchos yacimientos clásicos, que ha obligado a explorar nuevas alternativas.

Entre los distintos tipos de hidrocarburos fósiles, en lo que respecta en particular al gas natural se denominan fuentes no convencionales a aquellas que no se explotaban tradicionalmente debido a su difícil acceso o bajo rendimiento. Estos condicionantes implicaban unos costos de producción elevados, que en la mayor parte de los casos hacía inviable su explotación comercial. En la actualidad, el esfuerzo en el desarrollo científico y tecnológico que se está realizando está transformando en rentables estas nuevas fuentes de producción, con lo que su explotación es ya una realidad. Entre estas nuevas fuentes pueden destacarse los *hidratos de gas*, donde las moléculas de metano se encuentran

atrapadas en la estructura cristalina de hielo, existiendo depósitos con cantidades de gas muy elevadas, principalmente en los fondos oceánicos y en suelos helados en las regiones polares. Otro tipo de depósitos son aquellos donde el gas se encuentra retenido en estructuras geológicas de porosidad elevada. En esta situación se distinguen varios casos diferentes: el gas de esquisto o *shale gas*, que se extrae de terrenos donde abundan los esquistos, el denominado *tight gas*, donde el gas se encuentra atrapado en sustratos de arenas compactas, y el *coal bed methane*, que se sitúa en mantos de carbón. En todos estos casos el gas natural no se presenta en forma de bolsas, sino que se encuentra adsorbido sobre sustratos de roca de distinta naturaleza y estructura porosa, y por tanto sus moléculas están atrapadas por una interacción sólido-fluido de elevada intensidad, que provoca que su movilidad sea muy reducida.

Los métodos de extracción necesarios para explotar estos yacimientos no convencionales son complejos, y las soluciones técnicas son un desafío de ingeniería de primera magnitud, todavía no resuelto de forma completamente satisfactoria. A diferencia de los yacimientos convencionales, muy localizados, de elevada productividad y larga vida, los yacimientos no convencionales se encuentran en general muy distribuidos, lo que obliga la implantación de un modelo de producción en serie, con gran cantidad de pozos horizontales de baja productividad individual y agotamiento rápido. Este hecho implica la exigencia de elevados estándares de eficiencia y calidad, y el necesario manejo de economías de escala. Una de las técnicas extractivas implicadas en las

que más se ha avanzado es la conocida como fractura hidráulica, o *fracking*, que es un procedimiento para optimizar la extracción que consiste en la inyección a presión de agua con arena en el terreno, con el objetivo de ampliar las fracturas existentes en el sustrato rocoso que encierra el gas o el petróleo, provocando así su flujo y salida al exterior. Ocasionalmente se pueden emplear también espumas o mezclas de gases, incluyendo distintos componentes de naturaleza polar. Aunque el método es efectivo porque mejora las tasas de recuperación existe una gran controversia sobre el peligro medioambiental asociado. Además de un enorme consumo de agua, es habitual que junto con la arena se incluya un elevado número de compuestos químicos, cuya finalidad es favorecer la fisuración o incluso la disolución de la roca, y que pueden contaminar tanto el terreno como los acuíferos subterráneos. Otro condicionante es la liberación del gas, no siempre controlada, con lo que pueden producirse importantes fugas a la atmósfera de gases con un potencial de efecto invernadero muy elevado.

Tras su descubrimiento como potencial fuente de energía, la cantidad de reservas de este tipo que se han ido descubriendo en los últimos años ha aumentado a un ritmo vertiginoso. Teniendo en cuenta los riesgos ambientales asociados a su extracción, ha surgido una gran controversia, y se han manifestado dos posiciones enfrentadas. Por un lado, países o regiones con legislación ambiental más laxa como Estados Unidos o América Latina han permitido su extracción, y por tanto la actividad en torno a este nuevo nicho de negocio

es frenética. Frente a esta postura Europa lidera la posición opuesta, que ha preferido actuar con cautela al abordar este estudio, estableciendo restricciones o incluso la prohibición absoluta de explotación.

En el caso del *shale gas*, como ejemplo representativo, la postura flexible de la administración en Estados Unidos ha producido una gran expansión en su exploración. Esto ha llevado a que hayan podido cuantificarse reservas recuperables de gas no convencional en un rango comprendido entre 11,9 a 34,8 trillones de metros cúbicos (tmc). Estas reservas estimadas son muy superiores a las de cualquier otro país, lo que le supondría pasar de ser el primer país importador de gas natural del mundo a poder exportar parte de este producto en un plazo de tiempo considerablemente corto, según las estimaciones de la Energy Information Administration (EIA). Estos datos muestran que si en el año 2008 el gas no convencional suponía apenas el 6% del consumo estadounidense, en el 2035, podría alcanzar el 56,8% de la producción total, asegurando el suministro de gas al mercado norteamericano durante un siglo[35].

En cambio, en Europa el desarrollo del negocio va más de una década por detrás de Estados Unidos debido a que la legislación vigente es más restrictiva que la de este país, donde el propietario de un terreno lo es también del subsuelo. Aún así, en Polonia se ha iniciado ya la exploración de este tipo de yacimientos. En España, también se han descubierto depósitos de gas no convencional en amplias áreas del Cantábrico, Pirineos y Aragón, lo que representa un hecho realmente destacable en un país que importa prácticamente

el 100% del petróleo y es absolutamente dependiente en materia energética. Como ejemplo significativo, en Álava, se ha descubierto una zona de 1.400 $km^2$, explorada en el marco del proyecto *Gran Enara*, y que según algunas estimaciones podría suponer una cantidad cuya cota máxima se encontraría en torno al equivalente al consumo de 5 años en toda España. Esta magnitud se puede considerar de especial importancia en un país que no dispone de ningún recurso energético fósil a excepción del carbón, muy cuestionado actualmente por el impacto medioambiental de sus emisiones. Sin embargo, en este caso particular la forma de explotación más rentable económicamente incluye una perforación que puede atravesar el acuífero subterráneo de Subijana, cuya cuenca se extiende sobre 170 $km^2$, por lo que está encontrando una gran oposición en los colectivos ecologistas, lo que está retrasando y eventualmente podría incluso descartar su explotación.

Otra de las fuentes no convencionales de gas natural citadas, que ocupa un papel de especial importancia, son los denominados *Tight Gas Reservoirs (TGR)*. Los TGR son depósitos de hidrocarburos de baja permeabilidad sobre sustrato poroso, que puede ser arena o roca, de los que puede extraerse principalmente gas natural. Debido al confinamiento del fluido en el sustrato poroso, estos depósitos deben ser fracturados mecánicamente para que su explotación sea rentable, tras lo cuál la extracción debe ser estimulada mediante la inyección forzada de una gran cantidad de fluido externo de base acuosa[36]. Los TGR se han encontrado en numerosas localizaciones geográficas, y se estima de

forma aproximada que suponen unas reservas globales de entre 300 y 500 tmc de gas, siendo por tanto un recurso esencial como alternativa de producción. A pesar de esto, debe destacarse el hecho de que el desconocimiento actual de su geología, estructura, comportamiento del fluido a extraer en condiciones reales, y demás características resultan en que con las técnicas actuales las tasas de recuperación son inferiores al 10%. Este hecho contrasta con que el 25% del gas natural utilizado en la actualidad en Estados Unidos provenga ya de este tipo de yacimientos[37], poniendo de manifiesto tanto su importancia actual como el margen de mejora existente para optimizar su extracción.

Estos hechos demuestran que la investigación sobre la caracterización precisa de este tipo de yacimientos es un tema de crucial importancia en la actualidad por su impacto económico en el sector energético[38], y su evolución futura hacia un protagonismo mucho mayor. De hecho, el estudio de los TGR es uno de los ámbitos de trabajo más activos en la actualidad en PetroFísica[39], involucrando a geólogos, ingenieros mecánicos, químicos e ingenieros químicos, ingenieros de materiales y físicos.

Esta situación estratégica, y la magnitud del reto tecnológico que involucra, contrasta con el conocimiento muy parcial que se tiene todavía sobre el comportamiento de las propiedades termofísicas y el equilibrio de fases de fluidos complejos. En particular, para el caso de fluidos no homogéneos, incluyendo interfases fluidas, contacto con sustratos sólidos, sean planos o estructurados, adsorción, capilaridad, etc. las herramientas de estimación teórica existentes

son todavía muy limitadas. Esto resulta en que en general no es posible obtener una descripción *a priori* del comportamiento, y en particular las propiedades interfaciales de un fluido complejo como el gas natural en las condiciones reales de este tipo de yacimientos no convencionales. Teniendo en cuenta que estas propiedades determinan en gran medida el comportamiento del fluido en estas condiciones, un aspecto crucial para contribuir a optimizar la explotación es, sin duda, la determinación precisa del comportamiento del gas natural en el interior del yacimiento.

Por las características de baja permeabilidad citadas, la física del fluido en estas condiciones está gobernada por la adhesión y adsorción sobre el sustrato poroso, con lo que la extracción está absolutamente condicionada por las propiedades de interfase entre el fluido y el sustrato sólido poroso. Desde un punto de vista microscópico, cuando un fluido entra en contacto con un sustrato o superficie sólida, la competencia entre las fuerzas intra e interatómicas y las interacciones de las moléculas con la superficie conllevan un cambio drástico en el comportamiento del fluido, afectando en particular a las transiciones de fase del fluido libre. En muchos casos se produce la aparición de nuevas fases no presentes en el fluido libre, y la configuración de puntos o líneas críticas puede cambiar completamente. De este modo, estas interacciones pueden promover fenómenos como la ordenación de las moléculas en la proximidad de la superficie, creación de una capa adsorbida, o bien fenómenos de capilaridad y mojado (*wetting*). Esto pone de manifiesto la importancia de

la determinación precisa de propiedades interfaciales como tensión superficial, perfiles de densidad y presión, coeficientes de adsorción, y efectos de capilaridad y mojado en las condiciones reales de presión y temperatura en este tipo de sistemas.

Otro aspecto clave para conseguir una tasa de extracción elevada es conocer la alteración de la estructura de la interfase sólido fluido debida a la inyección del fluido acuoso externo. Este fluido inyectado tiene base acuosa, pero la adición de componentes polares como el $CO_2$ consigue producir una adsorción selectiva sobre el sustrato sólido, induciendo la desorción y por tanto, la mejora en la recuperación del gas natural (donde el metano es el compuesto mayoritario) retenido en el depósito. La adición de $CO_2$ proporciona otra de las claves del interés del proceso, ya que la extracción podría llevar asociado el almacenaje en depósitos geológicos profundos del $CO_2$ utilizado, como efecto secundario ideal. El interés en este punto de las compañías petrolíferas es optimizar el proceso para conseguir un almacenaje máximo de $CO_2$ por interacción con el sustrato poroso, una cuestión fundamental en las políticas internacionales de lucha contra el cambio climático, ya que puede representar una de las alternativas más viables como finalización de los procesos de recuperación y almacenaje de gases de elevado efecto invernadero. En este escenario, y a pesar de que el gas natural real incluye muchas otras moléculas además del metano, como primera aproximación el análisis detallado del equilibrio de fases y propiedades interfaciales de una mezcla fluida conteniendo al

menos metano, agua y dióxido de carbono, en condiciones de fluido libre y de confinamiento, es un objetivo de utilidad incuestionable. Como se demostrará a lo largo de este trabajo, a pesar de tratarse de moléculas ubicuas y estudiadas en profundidad desde muchas perspectivas, el objetivo planteado está lejos de haber sido resuelto de forma satisfactoria.

## 1.2 Técnicas de Simulación Molecular

El estudio de sistemas fluidos con presencia de varias fases, bien sea de una sustancia pura o de una mezcla multicomponente, es uno de los más claros ejemplos del desarrollo experimentado por los métodos de modelización desde el punto de visto atómico y molecular en las últimas décadas. En efecto, este es un ámbito de investigación de extraordinaria actividad, donde la constatación de la creciente versatilidad y fiabilidad de estas técnicas ha aumentado con gran rapidez su demanda por parte de la industria. Además, la ventaja competitiva de su reducido coste económico comparado con la realización de medidas experimentales, especialmente en rangos de condiciones extremas de presión y temperatura, ha convertido la simulación molecular en una de las principales herramientas prospectivas desde un punto de vista aplicado.

Los factores que sin duda han contribuido a la gran expansión sufrida por los métodos de simulación molecular son, en primer lugar, la aparición constante de nuevos métodos teóricos basados tanto en la Mecánica Cuántica

como en la Estadística, que con la utilización de potenciales de interacción cada vez más precisos permiten abordar problemas de mayor complejidad, y se aproximan cada vez más a la descripción de sistemas reales. Por otro lado, el aumento de la velocidad de proceso y la memoria de los ordenadores hace accesible el cálculo en sistemas no abordables hasta fechas recientes.

Por estas razones, las técnicas de simulación molecular de Monte Carlo y Dinámica Molecular destacan entre los métodos de modelización más conocidos y ampliamente utilizados en la actualidad. Sin duda, se han convertido en una de las herramientas más poderosas de la Mecánica Estadística para abordar el estudio de sistemas realistas desde un punto de vista microscópico, permitiendo así el acceso a la información del sistema a escala atómica para el cálculo de propiedades, como las interfaciales, que han permitido entender el comportamiento anómalo de ciertos fluidos, corroborando y aportando una justificación teórica formal a observaciones experimentales, y en ocasiones permitiendo el contraste con otras aproximaciones teóricas, como ecuaciones de estado u otro tipo de modelos Termodinámicos o Estadísticos.

En el ámbito de la Termodinámica de Fluidos, han sido clave en el desarrollo de las técnicas de simulación molecular los siguientes factores:

- El hecho aceptado de que la simulación molecular produce resultados exactos, si las condiciones de cálculo se establecen con rigor, para las propiedades macroscópicas de un fluido teórico derivadas de la elección de un conjunto de potenciales de interacción a escala atómica o molecu-

lar. La simulación se considera desde esta perspectiva como un experimento virtual ("*in silico*"), o banco de pruebas para comprobar la validez de teorías Termodinámicas o Estadísticas que parten del mismo modelo molecular y se desarrollan a través de la asunción de una serie de aproximaciones. Esta estrategia ha provocado una evolución destacable por ejemplo en las ecuaciones de estado, siendo cada vez más eficientes y realistas por la posibilidad de contrastarlas rápidamente con datos exactos del modelo sobre el que se fundamentan. Esta comparación reemplaza en muchos casos a la comparación con datos experimentales, que además de ser costosos o incluso inaccesibles, no se corresponden en rigor con el mismo modelo molecular asumido por una teoría dada. Las teorías, de esta forma, se comprueban comparando con la simulación molecular de su modelo microscópico exacto, y luego se ajustan para reproducir con la mayor fidelidad posible los datos experimentales.

- La comparación con datos experimentales ha guiado por su parte la evolución hacia modelos moleculares cada vez más realistas, indicando cuáles deben ser los fenómenos descritos por un modelo dado y hasta que grado de detalle o complejidad debe crecer para capturar la Física observada de un sistema. Así, se ha llegado a dar explicaciones cada vez más satisfactorias a fenómenos físicos y químicos tan importantes como por ejemplo la estructura y las transiciones de fase de fluidos complejos, la formación de micelas o el pliegue de proteínas.

- La constatación de las limitaciones que encuentran algunas leyes macroscópicas empíricas clásicas cuando se aplican a escala nanométrica, incluyendo conceptos de la Termodinánica de superficie de Gibbs[40]: tensión superficial, propiedades de superficie de exceso y las ecuaciones de Laplace, Kelvin, Young, etc... ha resultado en un nuevo aliciente para la aplicación de técnicas de simulación molecular para explorar los límites de validez de estas teorías.

### 1.2.1 Historia

El método de Monte Carlo es un método de muestreo estadístico propuesto con el objetivo inicial de resolver numéricamente las ecuaciones de la Mecánica Estadística. Los primeros objetivos de su aplicación se enmarcaban dentro de la industria militar. En sus inicios, fue aplicado para buscar soluciones de problemas deterministas, bien establecidos desde un punto de vista teórico, y para los que no existía una estrategia de resolución numérica eficiente. En estos problemas, se consideraba que la materia estaba compuesta por átomos o moléculas que interaccionaban entre sí mediante una energía potencial intermolecular conocida, obedeciendo las leyes de la Mecánica Estadística. Ya en sus inicios, los científicos del gobierno estadounidense, que fueron los primeros en tener acceso a ordenadores electrónicos, empezaron a tener conciencia de la potencia del método al darse cuenta que los resultados obtenidos tenían una precisión proporcional a la precisión utilizada en el potencial de interacción

molecular[41–44].

En 1934, Enrico Fermi fue uno de las primeros científicos que usó el método de Monte Carlo para estudiar la difusión de neutrones, pero las calculadoras mecánicas de la época no eran lo suficientemente potentes para realizar cálculos tan pesados como los que se requerían, por lo que no existe ninguna publicación científica que constate su utilización, sólo el relato de su antiguo estudiante Emilio Segre[45]. Con anterioridad ya Lord Kelvin, con la ayuda de su asistente William Anderson, quién realizó a mano el cálculo de al menos 5000 colisiones, usó este método de muestreo estadístico para analizar la trayectoria de partículas bajo colisiones elásticas para comprobar el Teorema de Equipartición, uno de los pilares de la Mecánica Estadística[46]. Estos fueron los primeros ensayos de un método cuya aplicación estaba limitada entonces por la potencia de las calculadoras mecánicas y electromecánicas de la época.

Sin embargo, a mediados de los años 40 se produjo un hecho que provocó el ímpetu necesario para seguir desarrollando y extendiendo la aplicación del método, que fue la aparición de los primeros ordenadores, los ENIAC (Electronic Numerical Integrator and Computer), desarrollados en la Universidad de Pensilvania, y que eran 100 veces más rápidos que la mejor calculadora electromecánica de la época. En 1946, Stan Ulam le dió su aplicación más conocida hasta el momento, utilizando un método basado en números aleatorios para estudiar la distancia que atravesarían los neutrones en diferentes materiales. Esta aplicación era clave en el proyecto Manhattan, que perseguía

la descripción precisa de los procesos de fisión nuclear, con el infausto objetivo de construir la bomba atómica. Los científicos de la base militar de Los Alamos habían fracasado hasta ese momento en su búsqueda de un método de resolución del sistema de ecuaciones hidrodinámicas acopladas que describía el problema usando métodos matemáticos convencionales. Este trabajo secreto requería un nombre en clave, y fue Nicholas Metropolis, quién colaboró en dicho proyecto con Stan Ulam, quien le asignó su denominación por la relación entre el azar de la generación de números aleatorios y el Casino de Monte Carlo. Las simulaciones del método de Monte Carlo desempeñaron un papel fundamental en el proyecto Manhattan, haciéndose muy popular una vez concluida la segunda guerra mundial, en paralelo al desarrollo de los primeros ordenadores electrónicos, lo que generalizó su uso en múltiples campos de investigación de la Física y la Química.

A lo largo del tiempo, muchos científicos trabajaron en el desarrollo del método, pero hubo que esperar hasta 1953, cuando Metropolis et al.[43] publicaron el primer artículo científico que sentó las bases de este método, y donde se introdujo por primera vez la idea de las *cadenas de Markov*, para garantizar la ergodicidad del método.

### 1.2.2 Descripción del método

Las *cadenas de Markov* son un tipo de series discretas estocásticas en las que la probabilidad de que ocurra un evento depende del evento inmediatamente

anterior. Por tanto la diferencia entre este tipo de cadenas y las series de eventos independientes, tales como el ejemplo clásico de lanzar una moneda al aire, radica en que las primeras memorizan el último evento y esto condiciona los posibles eventos futuros.

Supongamos una serie consecutiva de variables aleatorias $\{X_1, X_2, ..., X_s, ...\}$ que forman una cadena de Markov. Los posibles valores de las variables $X_i$ forman un conjunto finito R={1,2,...,m,...,n,...,r} denominado *espacio de estados de la cadena*. Los cambios de estado del sistema se llaman *transiciones*, y las probabilidades asociadas con estos cambios de estado, *probabilidades de transición*, que son almacenadas en una matriz $\pi$, denominada *matriz de transición*, donde el elemento $\pi_{mn}$ representa la probabilidad de transición del estado $m$ al $n$. Con el fin de tener una cadena de Markov ergódica, tal y como la definieron Metropolis et al.[43], se necesita que esta matriz de transición $\pi$ cumpla la *condición de balance detallado* o *reversibilidad microscópica*, que se definirá posteriormente. La principal característica de este tipo de cadenas, que las hace tan útiles desde el punto de vista físico, es que llegado un determinado paso de la cadena, ésta converge a una determinada distribución de probabilidad $p$, es decir, a partir de un cierto instante los estados sucesivos se seleccionan con la misma probabilidad, la probabilidad límite $p$.

Desde el punto de vista de la Mecánica Estadística, que es la disciplina que se ocupa del estudio del comportamiento de sistemas macroscópicos a partir de su descripción a escala microscópica, puede afirmarse que llegado un

determinado momento el sistema está transitando por los microestados compatibles con un macroestado dado, denominados *microestados accesibles*, lo que nos permite calcular el valor de las propiedades físicas objeto de interés mediante el promedio de su evaluación en cada uno de los microestados explorados. Por tanto, la Mecánica Estadística en combinación con una cadena de Markov ergódica proporciona el marco perfecto para hacer estimaciones de propiedades macroscópicas a partir de las configuraciones microscópicas, estableciendo un nexo entre ambas escalas.

Al conjunto de estados microscópicos compatibles con un macroestado dado se le conoce con el nombre de *colectivo*. Así, el colectivo estadístico es una idealización de un gran número de copias de un sistema, todas ellas representando un posible estado en el que el sistema real podría hallarse. Existen diferentes colectivos estadísticos, en función de las diferentes situaciones físicas que se pueden presentar, y éstos se etiquetan con las mismas variables termodinámicas o variables de estado que definen el macroestado, como por ejemplo, la temperatura $T$, la presión $P$, el volumen $V$, el número de partículas $N$, la entalpía $H$, etc. Cada colectivo está formado por tanto por el conjunto de microestados compatibles con un macroestado dado en el que se han fijado los valores de unas determinadas variables termodinámicas, que en los casos más relevantes para este estudio son:

- **Colectivo microcanónico {NVE}**. Son invariables el número de partículas $N$, el volumen que ocupan $V$ y la energía total del sistema $E$.

Cada microestado se describe mediante las variables canónicas.

- **Colectivo canónico {NVT}**. Son invariables el número de partículas $N$, el volumen que ocupan $V$ y la temperatura $T$. En este colectivo, cada microestado se describe también mediante las variables canónicas.

- **Colectivo isotérmo - isobárico {NPT}**. Son invariables el número de partículas $N$, la presión $P$ y la temperatura $T$, y cada microestado se describe mediante las variables canónicas y el volumen $V$.

- **Colectivo Gran Canónico {$\mu$VT}**. Son invariables el potencial químico $\mu$, el volumen del sistema $V$ y la temperatura $T$. Cada microestado se describe mediante las variables canónicas. Este colectivo tiene una aplicación fundamental en el cálculo de la cantidad adsorbida de una determinada sustancia en una superficie impuesta, ya que el dispositivo experimental es reproducido por un depósito ficticio que intercambia partículas y energía con la celda de simulación donde se encuentra el adsorbente. Al alcanzar el equilibrio termodinámico los valores del potencial químico y la temperatura en la celda de simulación son iguales a los del depósito ficticio.

Existen en la literatura un gran número de excelentes monografías que explican con todo detalle las distintas técnicas de simulación molecular desarrolladas hasta el momento, incluyendo su fundamentación teórica, descripción de su algoritmia e implementación, y las aplicaciones más adecuadas en cada

caso. Sin ánimo de exhaustividad, pueden citarse como textos de referencia en el ámbito que ocupa a este trabajo las obras de Allen y Tildesley[47], Frenkel y Smit[48], Landau y Binder[49], Sadus[50], Rapaport[51], Heyes[52], o Ungerer *et al.*[53], entre otros. Las obras citadas describen las técnicas de simulación molecular aplicadas en el marco de la Mecánica Estadística clásica, que es el utilizado a lo largo de este trabajo, pero es conveniente recordar que en Física Computacional tiene también una gran relevancia la combinación de estas técnicas de simulación con la Mecánica Cuántica, que constituye un ámbito de investigación de extraordinaria relevancia en la actualidad[54,55].

A modo de presentación de la estructura de los cálculos de simulación molecular incluidos en este trabajo, se expone a continuación una descripción esquemática del método de Monte Carlo para el caso de una sustancia pura en el colectivo canónico. Según se ha descrito, en este colectivo la simulación se realiza manteniendo constante el número de partículas, volumen y temperatura {NVT}.

Se considera para empezar una caja de simulación cúbica de lado $L$ donde se introducen, de forma aleatoria o bien con una configuración inicial que se corresponda con una red cristalina, $N$ partículas o moléculas, representando la sustancia objeto de estudio. Así, el sistema de partículas se encuentra en su estado inicial definido por un conjunto de coordenadas $(x^N)_m \equiv (x_1, x_2, ..., x_n)_m$ que contienen toda la información necesaria (posiciones, ángulos orientacionales, etc.) para especificar la configuración molecular de este sistema formado por

$N$ partículas. A partir de esta configuración inicial, cuya distribución inicial aleatoria en su caso se justifica por el hecho de que las propiedades de la cadena de Markov son independiendes del estado de partida, se crea una cadena de microestados por los que el sistema va transitando, procediendo de la siguiente forma:

- En primer lugar, se genera una nueva configuración aleatoria $n$ a partir del estado anterior $m$. Esta nueva configuración $n$ se obtiene a partir de la elección de una partícula al azar, que es rotada o trasladada una distancia o ángulo seleccionados también al azar, y que está definida por el conjunto de coordenadas $(x^N)_n \equiv (x_1, x_2, ..., x_n)_n$.

- A continuación, se evalúa el cambio en la energía potencial configuracional que experimenta el sistema en su tránsito de la configuración $m$ (inicial) a la $n$ (final), mediante el campo de fuerzas al que están sometidas las partículas, $\Delta U = U_n - U_m$. Finalmente, el movimiento se acepta o se rechaza de acuerdo con la ley de distribución de probabilidad a la que está sometido el colectivo estadístico objeto de estudio, en este caso, el colectivo canónico, y sujeta a la condición de balance detallado.

La condición de balance detallado impone que la probabilidad de transición del estado $m$ al $n$ debe ser igual a la de transición del estado $n$ al $m$, es decir, que la cadena de Markov es reversible y que por tanto el sistema se encuentra en equilibrio termodinámico. Todos los algoritmos de Monte Carlo

deben obedecer este principio independientemente del movimiento realizado o del colectivo estadístico usado, ya que en cualquier otro caso el sistema no se encontraría en equilibrio. Matemáticamente esta condición se expresa mediante la siguiente ecuación, fundamental en el método de Monte Carlo[47,48]:

$$\frac{p_{mn}(m \to n)}{p_{nm}(n \to m)} = \frac{\rho_n}{\rho_m} \tag{1.1}$$

donde $p_{mn}(m \to n)$ y $p_{nm}(n \to m)$ expresan la probabilidad de aceptación del movimiento en el paso de la configuración $m$ hasta la $n$, y de la $n$ hasta la $m$, respectivamente, y $\rho_m$ la probabilidad de que el sistema se encuentre en la configuración o microestado $m$.

En el colectivo canónico, la probabilidad de que el sistema se encuentre en la configuración $n$ viene dada por la ley de distribución de Boltzmann:

$$\rho_n = \frac{e^{-U/k_B T}}{Q} \tag{1.2}$$

donde Q es la función de partición canónica:

$$Q = \sum_n e^{-U/k_B T} \tag{1.3}$$

y la probabilidad de aceptación del intento de movimiento desde la configuración $m$ hasta la $n$, relativa al movimiento inverso, del $n$ al $m$, viene dada

por:

$$\frac{p_{mn}(m \to n)}{p_{nm}(n \to m)} = \frac{\rho_n}{\rho_m} = exp\{-\beta \left[U(x^N)_n - U(x^N)_m\right]\} = exp\{-\beta \Delta U\} \quad (1.4)$$

Así, siguiendo el esquema de Metropolis et al.[43], si la configuración final tiene una menor energía potencial que la inicial se cumple que $\Delta U < 0$ y $\rho_n/\rho_m > 1$, y por lo tanto el movimiento es aceptado siempre. En el caso contrario, si la energía del sistema se incrementa, $\Delta U > 0$, la configuración final tiene mayor energía potencial atractiva, es decir, $\rho_n/\rho_m < 1$, y el movimiento es aceptado con probabilidad $\rho_n/\rho_m$=$exp\{-\beta \Delta U\}$. Esto puede resumirse escribiendo la probabilidad de aceptación para un movimiento de Monte Carlo, $P_{acc} = p_{mn}(m \to n)$, como,

$$P_{acc} = min\left[1, exp\left(-\frac{\Delta U}{k_B T}\right)\right] \quad (1.5)$$

De esta forma, repitiendo este procedimiento se genera una cadena de Markov que explora el espacio de configuraciones del sistema. El caso más habitual es que la configuración de partida seleccionada no se corresponda con las condiciones de equilibrio asociadas a los valores de la variables termodinámicas fijadas en el colectivo de trabajo (en este caso, número de partículas, volumen y temperatura). Si esto es así, el sistema necesitará de una fase de cálculo de equilibrado, o evolución hacia el equilibrio. Esta etapa de equilibrado consta de un número variable de ciclos de simulación, que debe ajustarse hasta

garantizar que las variables de estado del sistema se estabilizan fluctuando en torno a valores promedio. En ese momento, en el que el sistema se considera estabilizado, es cuando se puede iniciar la fase de producción del cálculo. A partir de este punto, si en el proceso se recorre un número de estados estadísticamente significativo se puede realizar el cálculo de las propiedades termodinámicas de equilibrio del sistema (energía configuracional, capacidad calorífica, propiedades estructurales, etc.), promediando directamente sobre los valores individuales de dichas propiedades en los microestados explorados.

Cuando el objetivo que se persigue es comparar los resultados de la simulación de Monte Carlo de un fluido con datos experimentales reales referidos a las moléculas que se están representando durante el cálculo, el colectivo canónico puede no ser el más adecuado. El caso más frecuente es que en experimentos de laboratorio con fluidos sean invariables la cantidad de materia presente, presión y temperatura, con lo que el colectivo que representa estas condiciones es el isotermo-isobárico {NPT}. En este caso, la principal modificación que afecta al método con respecto al colectivo canónico es que el paso de una configuración $m$ a otra $n$ no está limitado a un cambio en las coordenadas moleculares, sino que puede incluir la fluctuación del tamaño de la celda de simulación, o volumen del sistema, como movimiento adicional. Esto convierte al colectivo {NPT} en el adecuado para el cálculo de propiedades de equilibrio de mezclas, donde los experimentos se realizan a presión constante en vez de a densidad constante. En cambio, en experimentos de adsorción,

la naturaleza anisótropa del sistema resulta en una estructura microscópica del fluido inhomogénea, con lo que la presión deja de ser una magnitud escalar. Además, es estos casos el sistema experimental sólido-fluido suele estar en contacto con un reservorio que contiene una gran cantidad de moléculas de fluido, que pueden acceder a la región interfacial o salir de ella, con lo que la cantidad de moléculas en interacción con el sustrato es variable. Esto significa que el colectivo que debe utilizarse para representar estas condiciones experimentales es el Gran Canónico $\{\mu\text{VT}\}$. En este caso se consideran dos tipos de movimientos adicionales respecto al colectivo canónico, que son la inserción y la eliminación de partículas, y que lo convierten el colectivo ideal para realizar cálculos de adsorción, fluidos confinados, capilaridad, etc.

### 1.2.3 Ventajas y desventajas del método de Monte Carlo

Una de las principales ventajas que presenta en método de Monte Carlo es la facilidad con la que puede aplicarse a una gran cantidad de colectivos estadísticos diferentes ($\{\text{NVT}\}$,$\{\text{NPT}\}$,$\{\mu\text{VT}\}$) donde las leyes de distribución de probabilidad están bien establecidas. Este hecho lo convierte en el método idóneo para abordar por ejemplo el estudio de transiciones de fase, ya que en estos procesos la evolución temporal es lenta comparada con las escalas de tiempo abordables hoy en simulación, lo que limita la aplicación de la Dinámica Molecular. Sin embargo, su principal desventaja es que no proporciona información sobre la evolución temporal de los sistemas, los movimientos

de las partículas son artificiales y no representan los movimientos dinámicos de un sistema real, con lo que no son accesibles de forma sencilla cálculos fuera del equilibrio, o propiedades de transporte como la viscosidad, difusividad o conductividad térmica.

### 1.2.4 Determinación de propiedades interfaciales

Se han propuesto varias técnicas de simulación molecular para el estudio del equilibrio de fases y el cálculo de propiedades interfaciales. Una alternativa para el análisis simultáneo de ambos es la elección de una caja de simulación multifásica inhomogénea, donde las fases coexistentes están en contacto directo entre sí, a través de una interfase explícita. Este método se ha demostrado muy eficaz para este tipo de estudios, frente a otras técnicas que permiten el estudio del diagrama de fases sin contacto material entre las fases coexistentes, como pueden ser la Integración Termodinámica[56] y el Colectivo de Gibbs[57]. La técnica de simulación de interfases explícitas tiene la ventaja que permite el acceso directo a la estructura de la interfase, y por tanto permite la determinación simultánea de las propiedades de las fases coexistentes (como la densidad de cada una), propiedades interfaciales macroscópicas (tensión interfacial, coeficientes de adsorción), y propiedades estructurales microscópicas como los perfiles de densidad a lo largo de la interfase, anchura interfacial o funciones de distribución radial, inaccesibles mediante los otros métodos citados. La implementación de este método de simulación de coexistencia di-

recta de fases presenta en cambio una serie de dificultades técnicas sutiles que pueden afectar de forma notable a los resultados cuantitativos obtenidos, y una elección de condiciones y variables poco acertada puede introducir, como se verá, artefactos en el cálculo que conducen a resultados erróneos. Entre estos factores juegan un papel fundamental los efectos de tamaño, que necesitan de la adecuada elección del tamaño de la caja de simulación, así como la inestabilidad potencial de la interfase generada o la necesidad de tratar de forma rigurosa las correciones de largo alcance en sistemas inhomogéneos. Otra posible desventaja del método es que es muy costoso desde el punto de vista computacional, y por ejemplo la estabilización de las interfases es un proceso lento, lo que limita el tamaño y complejidad de los sistemas accesibles. Respecto a esta característica, la optimización de código y el análisis comparativo de eficiencia de distintos métodos de cálculo, por ejemplo en el tratamiento de las correcciones de largo alcance, permiten un ahorro considerable de tiempo de cálculo, resultando en una mayor fiabilidad estadística de las simulaciones.

El método de simulación de coexistencia directa de fases fluidas fue ensayado por vez primera por Liu[58], en un trabajo en el que estimó la coexistencia directa de las fases líquida y vapor de un fluido Lennard-Jones a diferentes presiones y temperaturas. El proceso propuesto en este primer trabajo consta de dos etapas:

- En primer lugar, se sitúa el número de partículas necesario para repre-

sentar la fase líquida del fluido considerado en una caja de simulación cúbica, y se deja evolucionar el sistema hasta alcanzar el equilibrio en el colectivo isotermo-isobárico {NPT}.

- Una vez alcanzado el equilibrio, se utiliza la configuración final de la primera etapa de cálculo para construir la caja de simulación donde se realizará la simulación de coexistencia bifásica directa. Para ello, se añaden dos cajas cúbicas vacías de igual tamaño que la anterior, a ambos lados según la dirección $z$, obteniendo de este modo una caja paralelepipédica de dimensiones $L_x$=$L_y$=$L_z/3$. La elección de este tipo de geometría garantiza el cumplimiento de las condiciones de contorno periódicas en las tres direcciones espaciales, de modo que una partícula que salga por cualquiera de las caras del paralelepípedo vuelve a entrar en una región que contiene la misma fase del fluido de la que partía. Con esta configuración se continúa la simulación, pero ahora en el colectivo canónico {NVT}. Si el valor de densidad del fluido en la fase líquida es próximo al de coexistencia a la temperatura dada para el modelo molecular elegido, algunas moléculas comenzarán a saltar desde la región central hacia las cajas vacías añadidas, en las que se formará una fase menos densa (gas). Este proceso continúa si la elección de las condiciones de partida es adecuada, con lo que las dos interfases líquido-vapor se desarrollan hasta llegar a estar completamente equilibradas. A partir de este momento, comienza la etapa de producción, también a volumen

constante, durante la cuál se realizan los cálculos de las propiedades interfaciales, tanto macroscópicas como microscópicas.

Este método de simulación de fases coexistentes en contacto explícito es extensible, realizando pequeñas modificaciones, al estudio de otro tipo de equilibrios de fase, como el caso de mezclas multicomponentes. En dicho caso, se emplea la misma estructura de caja de simulación paralelepipédica, con una región central que alberga una de las fases, y la otra fase coexistente situada en dos regiones iguales, dispuestas de forma simétrica en los extremos de la caja en una de las direcciones espaciales. Estas modificaciones se resumen detalladamente a continuación:

- Inicialmente, deben establecerse con detalle todas las variables que involucra el equilibrio de fases que se pretende simular. Para ello debe conocerse con la mayor precisión posible las condiciones de presión, temperatura, y composición de fases coexistentes para el modelo molecular utilizado, con el objeto de poder construir la configuración de partida del sistema. Esta estimación inicial es crucial para el éxito del cálculo final, ya que si las condiciones impuestas no son las adecuadas las fases simuladas a continuación no se encontrarán en situación próxima al equilibrio de fases, y por tanto al ponerlas en contacto no se desarrollarán las interfases, colapsando el sistema en una única fase sin utilidad alguna. Estos condicionantes sugieren que es de gran utilidad utilizar, en

esta etapa previa, un modelo teórico de cálculo auxiliar para estimar las condiciones de equilibrio de fases. Una opción podría ser realizar una simulación molecular de Monte Carlo preliminar en un colectivo, como el de Gibbs, que nos proporcionase esta información para el modelo molecular a utilizar. Esta ruta es la formalmente correcta para estimar las condiciones de equilibrio del sistema, pero implica la necesidad de simulaciones adicionales y por tanto es muy costosa. Una alternativa es emplear como método de estimación de las condiciones de equilibrio un modelo termodinámico de naturaleza diferente, como por ejemplo una ecuación de estado. La ventaja de esta alternativa es que permite obtener el equilibrio de fases global de la mezcla considerada en un tiempo muy inferior al que sería preciso si se utilizasen sólo cálculos de simulación. La desventaja es que, en el caso más general, el modelo molecular para el que se ha desarrollado y parametrizado la ecuación de estado no es el mismo que el utilizado durante la simulación molecular, con lo que el equilibrio de fases descrito usando ambos métodos no coincide y podría incluso ser muy discrepante. A pesar de esto, estudiando con cuidado las alternativas, la elección de una ecuación de estado fiable y de sólida base física puede resultar muy efectiva si tanto los modelos moleculares de la ecuación como de la simulación son rigurosos y fiables desde un punto de vista realista. Este hecho se comprobará a lo largo de este trabajo, donde se ha empleado como modelo de referencia una versión de la

ecuación de estado derivada de teoría de perturbaciones conocida como SAFT[59] (*Statistical Association Fluid Theory*). Este ha sido el modelo auxiliar usado para determinar las condiciones de inicio de cada uno de los cálculos de simulación de interfases de mezclas, y constituye una piedra angular del trabajo, ya que sin una estimación muy precisa del punto de partida es prácticamente imposible obtener ningún resultado con sentido físico.

- Tras establecer las condiciones de presión, temperatura, y concentración de cada una de las fases coexistentes, se simula cada una de ellas en una caja independiente, partiendo de cajas de iguales dimensiones, $L_x = L_y = L_z$. Cada fase se equilibra en el colectivo {NPT}, pero de un modo ligeramente diferente al caso del fluido puro, ya que los cambios de volumen se llevan a cabo permitiendo solamente variaciones de la dimensión $L_z$ de cada una de ellas, para posibilitar su posterior acoplamiento a lo largo de la dirección $z$, una vez que se haya alcanzado el equilibrio.

- Alcanzado el equilibrio en cada fase, se realiza su acoplamiento con estructura de "sandwich", dejando un pequeño espacio entre ellas, generalemente $5\mathring{A}$ para favorecer la formación de las interfases y evitar superposiciones en la configuración de partida, obteniendo una caja de simulación multifásica con geometría similar al ejemplo anterior. A partir de aquí se deja evolucionar el sistema a volumen constante hasta que

las interfases se hayan equilibrado, y a continuación de nuevo comienza la fase de producción del cálculo.

En esta última etapa de cálculo, la caja de simulación se divide a lo largo del eje $z$ en cien partes idénticas, siendo por tanto cada división una caja de dimensiones $L_x = L_y = L_z/100$. Se determina y promedia a lo largo de la fase de producción la densidad en cada una de ellas para obtener el perfil de densidad de la caja a lo largo de cada interfase. En todo este proceso, la posición del centro de masas de la caja debe ser controlada y reajustada al centro geométrico de la caja, para evitar fluctuaciones que producirían un perfil de densidad borroso. Excluyendo las dos regiones de interfase, se pueden calcular las densidades de coexistencia de las distintas sustancias involucradas haciendo el promedio de los valores tomados sobre el perfil de densidad final, promediado a lo largo del cálculo.

La anchura interfacial también se calcula a partir de este perfil de densidad, en este caso ajustándolo a una función tangente hiperbólica, que para el caso de una caja bifásica en la que tenemos la presencia de una fase líquida y otra vapor, tendría la siguiente forma:

$$\rho(z) = \frac{1}{2}(\rho_l + \rho_v) - \frac{1}{2}(\rho_l - \rho_v) tanh\left[\frac{z - z_0}{d}\right] \tag{1.6}$$

donde $\rho_l$, $\rho_v$, $z_0$ y $d$ representan las densidades de coexistencia de líquido y vapor, posición de la superficie de división de Gibbs, y anchura de la interfase,

respectivamente. El ajuste a una función de este tipo no es el único criterio para establecer la extensión de la interfase. Con frecuencia se utiliza también la denominada anchura interfacial '10-90', denotada por $t$, que es la distancia entre los puntos de la interfase donde la densidad toma los valores del 10 y 90 por ciento del valor promedio de la fase más densa. La relación entre ambos parámetros es $t = 2.1972d$, teniendo en cuenta los efectos de borde.

En el caso del interés práctico descrito al principio de este capítulo, la extracción de gas natural de depósitos no convencionales, juega un papel crucial la adsorción del fluido sobre el sustrato con el que está en contacto. En este caso, aparece el confinamiento como nuevo escenario de fluido inhomogéneo, en el que el cálculo de las propiedades interfaciales tiene una gran importancia. Aplicando simulación molecular existen formas diversas de reproducir estas condiciones de contacto con un sustrato sólido. En el tipo de cajas de simulación descritas, una opción sencilla es eliminar las condiciones de contorno periódicas en una de las direcciones espaciales, como por ejemplo la dirección $z$. Con esta configuración, se introduce una anisotropía en el fluido, ante el que las paredes superior e inferior de la caja actúan ahora como superficies plano paralelas confinantes. Esta geometría se suele denotar como poro plano, y es de gran utilidad porque permite explorar condiciones de adsorción, capilaridad, mojado, efectos de tamaño de poro, etc. Además puede completarse la descripción considerando que las moléculas del fluido interaccionan con el sustrato sólido. En este caso, puede representarse el sólido como formado por

una red cristalina de átomos con posiciones fijas, donde cada uno de ellos interactúa a través de un potencial dado con cada una de las moléculas del fluido, o bien integrar estas interacciones calculando potenciales de interacción efectivos que dependen de la distancia y/o orientación relativa de cada molécula respecto a la pared.

En todas las situaciones descritas hasta el momento, tanto en el caso de sistemas libres como confinados, se consideran fluidos inhomogéneos, que pertenecen a un ámbito de conocomiento en Física extraordinariamente activo y donde la cantidad de fenómenos y comportamientos que aparecen es, sin duda, fascinante. Es preciso decir que la descripción teórica formal de los fenómenos de superficie en fluidos se ha desarrollado sólo de forma reciente, y en todo caso ha sido posterior al desarrollo de las Teorías de Estado Líquido. En la actualidad, la investigación en este tipo de fenómenos es muy intensa debido a sus implicaciones en multitud de aplicaciones tecnológicas. De entre las obras científicas que han hecho progresar el conocimiento en este campo pueden citarse textos claves como los de Henderson[60], Rowlinson y Widom[61], o de Gennes *et al.*[62].

El desarrollo de nuevas técnicas de cálculo mediante simulación molecular para determinar propiedades interfaciales, como la tensión interfacial, es en particular un área de investigación extraordinariamente activa en la actualidad. Algunos ejemplos son los métodos conocidos como Test-Area (TA)[63], Wandering Interface[64], o Expanded Ensemble[65], todos ellos propuestos muy

recientemente para determinar la tensión interfacial a través de la ruta termodinámica, que consiste en calcular esta propiedad como derivada parcial del potencial de Helmholtz respecto al área interfacial. Estos métodos representan una alternativa a la ruta mecánica clásica que implica el cálculo de las componentes del tensor de presiones, ya que en sistemas inhomogéneos la presión deja de ser una magnitud escalar e isótropa. Entre estos métodos de cálculo de componentes de la presión en sistemas inhomogéneos en simulación de Monte Carlo, se pueden citar el método perturbativo propuesto por de Miguel y Jackson[66], y el método tradicional de Irving y Kirkwood[67].

A lo largo del presente trabajo se han utilizado en concreto los siguientes métodos de cálculo:

- Cálculo mediante la ruta termodinámica:
  - Test-Area

    La técnica Test-Area (TA) fue propuesta por Gloor *et al.*[63], y se utiliza para determinar la tensión interfacial durante la simulación llevando a cabo cambios virtuales del área interfacial en la celda de simulación. Partiendo de la definición termodinámica de tensión interfacial:

    $$\gamma = \left(\frac{\partial A}{\partial \mathcal{A}}\right)_{N,V,T} \tag{1.7}$$

    donde $A$ representa el potencial de Helmholtz y $\mathcal{A}$ el área interfacial del sistema. Gloor *et al.*[63] demostraron como el cálculo de esta

derivada parcial puede obtenerse mediante un paso al límite, donde se evalúa la transición del sistema, mediante un desplazamiento virtual de volumen, desde un estado inicial hasta otro final en el que el área interfacial difiere una cantidad $\Delta\mathcal{A}$, con lo que puede escribirse:

$$\gamma = \lim_{\Delta A \to 0} \left( \frac{\Delta A_{0\to 1}}{\Delta \mathcal{A}} \right)_{N,V,T} = -\frac{\kappa_B T}{\Delta \mathcal{A}} ln \left\langle exp\left( \frac{-\Delta U}{\kappa_B T} \right) \right\rangle_0 \quad (1.8)$$

En esta ecuación, los subíndices 0 y 1 denotan los estados inicial y final del sistema, obtenidos mediante la traslación virtual de volumen, y $\Delta U$ es la diferencia de energía configuracional entre ambos. Este desplazamieno de volumen es virtual ya que no constituye un movimiento incorporado a la cadena de Markov del cálculo. El método consiste en tres pasos: se realiza el desplazamiento en el área interfacial $\Delta\mathcal{A}$ ajustando las demás dimensiones del sistema para que el volumen permanezca constante, se calcula la variación de la energía configuracional, y se recupera el estado de partida. Repitiendo este ensayo, y promediando al final de la simulación sobre el colectivo, tal y como indica el último término de la ecuación anterior, puede determinarse con gran precisión la tensión interfacial del sistema. El trabajo original proporciona varias claves para asegurar la convergencia y fiabilidad del método, como promediar

desplazamientos virtuales en los que el área interfacial se incrementa y se disminuye, estimar de modo conveniente el módulo de este cambio de área, etc.

El método TA ha llegado a ser muy popular debido a su versatilidad y su uso se ha extendido con rapidez en los últimos años, llegando a ser aplicado para el estudio interfacial de sistemas líquido-vapor tan variados como: cadenas Lennard-Jones[68], modelos realistas de agua[1], o mezclas binarias de fluidos[69,70].

- Cálculo mediante la ruta mecánica:

La tensión interfacial de un fluido inhomogéneo en coexistencia con su vapor puede calcularse a partir de la siguiente expresión:

$$\gamma = \int_{-\infty}^{+\infty} \left[ P_N(z) - P_T(z) \right] dz \tag{1.9}$$

donde se ha supuesto que la dirección $z$ es perpendicular a la interfase, y los subíndices $N$ y $T$ denotan las componentes de la presión normal y tangencial a la interfase. Para el caso particular de la caja de simulación bifásica descrita, donde conviene recordar que aparecen dos interfases explícitas, la ecuación anterior se convertiría en:

$$\gamma = \frac{L_z}{2} \left[ \langle P_{zz} \rangle - \frac{\langle P_{xx} \rangle + \langle P_{yy} \rangle}{2} \right] \tag{1.10}$$

donde $L_z$ es la longitud en la dirección $z$ de la caja de simulación, y $P_{\alpha\alpha}$ con $\alpha = x, y, z$ son las componentes diagonales del tensor de presiones. Desde esta expresión de partida, existen varias posibilidades de determinación de estas componentes.

– Método perturbativo propuesto por de Miguel and Jackson[66]

Entre ellos se encuentra el método perturbativo propuesto por de Miguel y Jackson[66], en el que el cálculo de $P_{\alpha\alpha}$ se obtiene realizando un cambio virtual de volumen en el cuál la dimensión de la caja $L_\alpha$ cambia a $L_\alpha + \Delta L_\alpha$, manteniendo constantes las otras dimensiones $L_\beta(\beta \neq \alpha)$. Para una expansión virtual ($\Delta V/V = \Delta L_\alpha/L_\alpha > 0$), la componente $P_{\alpha\alpha}$ se obtiene mediante la siguiente expresión:

$$P^{+}_{\alpha\alpha} = \frac{1}{\beta\Delta V} ln \left(1 + \frac{\Delta V}{V}\right)^{N} exp(-\beta\Delta U^{+}) \qquad (1.11)$$

donde $\Delta U^{+}$ es el cambio de la energía configuracional asociada al cambio de volumen expansivo. Para una compresión de volumen, donde la dimensión de la caja $L_\alpha$ se reduce a $L_\alpha - |\Delta L_\alpha|$, $P_{\alpha\alpha}$ se calcula de forma análoga:

$$P^{-}_{\alpha\alpha} = \frac{1}{-\beta\,|\Delta V|} ln \left(1 + \frac{|\Delta V|}{V}\right)^{N} exp(-\beta\Delta U^{-}) \qquad (1.12)$$

En el caso de un sistema con interacciones energéticas descritas

por un potencial intermolecular contínuo $P^{+}_{\alpha\alpha}$ y $P^{-}_{\alpha\alpha}$ toman valores prácticamente iguales, ya que energéticamente es equivalente realizar una expansión que una compresión. Además, como este sistema es inhomogéneo a lo largo de la dirección $z$, la componente microscópica perpendicular o normal (a lo largo del eje $z$) del tensor de presiones $P_N = P_{zz}$ debe ser constante y representa la presión de equilibrio del sistema, y a su vez las componentes microscópicos tangenciales $P_T = P_{xx} = P_{yy}$ son iguales a $P_T$ lejos de la interfase, pero alcanzan valores absolutos muy elevados y negativos en su proximidad.

– El método de Irving y Kirkwood[67]

De acuerdo con este método clásico de cálculo, las componentes tensoriales de la presión normal y tangencial a la interfase pueden determinarse de la siguiente forma:

$$P_N(z) = \rho(z)k_BT - \tfrac{1}{2\mathcal{A}}\left\langle \sum_{i=1}^{N-1}\sum_{j=i+1}^{N} \frac{|z_{ij}|}{r_{ij}}\frac{du(r_{ij})}{dr}\Theta\left(\frac{z-z_i}{z_{ij}}\right)\Theta\left(\frac{z_j-z}{z_{ij}}\right)\right\rangle \quad (1.13)$$

$$P_T(z) = \rho(z)k_BT - \tfrac{1}{4\mathcal{A}}\left\langle \sum_{i=1}^{N-1}\sum_{j=i+1}^{N} \frac{(x_{ij}^2+y_{ij}^2)}{r_{ij}\cdot|z_{ij}|}\frac{du(r_{ij})}{dr}\Theta\left(\frac{z-z_i}{z_{ij}}\right)\Theta\left(\frac{z_j-z}{z_{ij}}\right)\right\rangle \quad (1.14)$$

donde de nuevo $\mathcal{A}$ representa el área interfacial, $\Theta$ es la función de Heaviside, y el subíndice $ij$ se refiere a la distancia sobre la coordenada correspondiente entre las moléculas $i$ y $j$. La determinación de la tensión interfacial a partir de las componentes de la presión

es, como se ha mostrado, directa a través de la ruta mecánica. Este método es robusto y se ha utilizado con frecuencia, pero presenta una característica que representa una desventaja clara frente a por ejemplo el método TA. Como puede verse en las ecuaciones de cálculo de $P_N$ y $P_T$, el primer término involucra el perfil de densidad del sistema, que debe actualizarse a lo largo de la simulación de forma constante, lo que por un lado complica su implementación y por otro resulta computacionalmente costoso. En todo caso, a lo largo de este trabajo se ha empleado este método para comparar y validar los resultados obtenidos con las otras alternativas de cálculo citadas.

## 1.3 Objetivos

Una vez establecido el interés práctico del estudio de propiedades interfaciales de sistemas fluidos conteniendo metano, agua, y dióxido de carbono, en el marco de la extracción de gas natural de fuentes no convencionales, se plantean en este trabajo los siguientes objetivos:

- Cálculo de propiedades interfaciales usando el método de Monte Carlo

  Se realizará una evaluación crítica de los métodos más utilizados en la actualidad para determinar propiedades interfaciales de fluidos mediante el método de la coexistencia directa de fases. Se considerarán,

para las moléculas objeto de estudio, los modelos moleculares más habituales, centrando el interés en modelos de átomos unidos, rígidos y no polarizables, pero considerando de forma explícita las interacciones de Coulomb por su relevancia. Se compararán los resultados cuantitativos de los distintos modelos o parametrizaciones en cada caso. Respecto a las metodologías de cálculo, se prestará especial atención a la descripción rigurosa y formal de las correcciones de largo alcance, a la energía configuracional del sistema, tanto en las interacciones dispersivas como a las electrostáticas. Se tratará de establecer el alcance cuantitativo de estas contribuciones, para estimar con la mayor precisión posible el rendimiento de cada modelo en el cálculo de la tensión interfacial líquido-gas en interfases libres. También se evaluará la aplicabilidad de métodos de desplazamiento virtual de volumen a la estimación de propiedades interfaciales de fluidos en situación de confinamiento por un sustrato sólido interaccionante.

- Estimación del equilibrio de fases

  Con el objetivo de determinar el diagrama de fases global de la mezcla ternaria objeto de interés, se utilizará una ecuación de estado molecular, por la imposibilidad de acceder a esta descripción sólo mediante simulación molecular. Por su rigor, versatilidad y demostrada eficacia en la estimación aplicada a este tipo de moléculas, se utilizará la ecuación SAFT en su versión de rango variable. Se describirá el comportamiento

de fases de cada una de las mezclas binarias involucradas, así como de la mezcla ternaria, intentando minimizar la parametrización del modelo, con el fin de tener una guía fiable para determinar las condiciones en las que se realizarán las simulaciones posteriormente. Este análisis se extenderá a un rango de temperaturas y presiones que incluya las condiciones reales de yacimiento en el tipo de depósitos de gas no convencionales descrito.

- Propiedades interfaciales de mezcla

  Usando la metodología de simulación molecular optimizada descrita como primer objetivo, y seleccionando las condiciones de equilibrio estimadas a través de la ecuación de estado, se estudiará la capacidad de los modelos moleculares utilizados para describir el comportamiento interfacial de mezclas binarias, incluyendo la determinación de la tensión interfacial, pero también la descripción de fenómenos de adsorción preferencial y mojado. Se comparará esta descripción con otras teorías de medios inhomogéneos como la Teoría del Gradiente[71]. A continuación, se extenderá este estudio a la mezcla ternaria, tratando de localizar la región de coexistencia trifásica, y las propiedades interfaciales de la misma.

- Fluidos confinados

  Tras establecer las propiedades interfaciales de las mezclas, en situación de interfase libre, se extenderá el estudio al caso de confinamiento entre

paredes plano paralelas no estructuradas interaccionantes. El objetivo en este caso es estudiar los efectos de la interacción impuesta por el sustrato, y como esta alteración modifica las propiedades estructurales, interfaciales y de adsorción de las mezclas estudiadas en situación de fluido libre. El objetivo final es discutir el efecto de la inyección de un fluido externo de base acuosa sobre un fluido compuesto por metano y adsorbido sobre un sustrato, imitando en lo posible las condiciones halladas en los yacimientos descritos anteriormente.

# Chapter 2

# Calculation of interfacial properties using molecular simulation with the reaction field method: Results for different water models

## 2.1 Abstract

Coulombic interactions in molecular simulation are usually computed using the Ewald summation technique. This method is reliable for homogeneous and inhomogeneous systems but remarkably time consuming. This means a serious shortcoming in cases where unusually long simulation runs are necessary, as for instance during the calculation of interfacial properties, a subject of increasing interest. In homogeneous systems, the Reaction Field (RF) method can be alternatively used reducing not only the computation time but also the difficulty of its implementation. However, it can not be applied for inhomogeneous systems, at least from a strict formal point of view. In this paper, an analysis of the discrepancies in the computation of interfacial properties of water using the RF method is performed using constant volume biphasic Monte Carlo simulations, considering several of the most popular models available. The results show good quantitative agreement, within the simulation uncertainty, with the values obtained from the Ewald sums method. This result states the applicability of the Reaction Field method for interfacial properties calculation for this type of molecules.

## 2.2 Introduction

The development of novel calculation techniques to determine interfacial properties of fluids using molecular simulation is a very active research area

nowadays. Some recent examples are the Test-Area (TA)[63], Wandering Interface[64], or Expanded Ensemble[65] methods, that can be used to determine interfacial tension through the so called thermodynamic route. These methods represent an alternative to the classical mechanical route, which entails the determination of the components of the pressure tensor. A comparative study of several area sampling approaches has been published by Errington and Kofke[72]. These methods have been already applied with remarkable results to different molecular models, and for instance the TA method has been used to study the vapour-liquid interfacial properties of Lennard-Jones (LJ) chains[68], several water models[1], or the Mie potential[73,74]. Although the application of these inhomogeneous fluid calculation methods is now feasible due to the advance in computational resources efficiency, a common feature to these techniques is that they require long simulation runs, for the combination of two reasons. First, the simulation of inhomogeneous systems containing explicit interphases needs a larger number of molecules than the typical scale of bulk fluid simulations. Second, the number of cycles must be greatly increased as well, in order to adequately equilibrate and sample the system under study. In addition, if the simulation includes molecules containing explicit electric charges, the calculation of the coulombic contribution to the system total energy increases to a great extent the computing time, because this is done most often using the Ewald sums method[48] or alternatively the more efficient Particle Mesh Ewald (PME) technique[75]. The election of these procedures is

not fortuitous since they are strictly correct methods to evaluate coulombic interactions in either homogeneous or inhomogeneous systems. From another perspective, the calculation of coulombic interactions in molecular simulation may be also dealt with the so-called Reaction Field (RF) method[76–94]. In this method the energy of a molecule is obtained as the addition of two terms. The first one accounts for the interaction energy between the considered molecule and those located within a sphere of radius $r_c$ centered in the first one. The second term involves the interaction energy with the molecules placed beyond this sphere, which is calculated by considering that the medium surrounding the sphere is a continuous and homogeneous dielectric. Specific expressions have been derived in literature depending on the details of the system considered[77,83,85,87–92]. Due to the nature of this method, it has been widely applied for homogeneous systems. However, recently, there is an increasing interest in the study of its potential applicability to inhomogeneous systems, after the promising results obtained for molecular ions[95], biomolecules in water[96,97], short peptides in water[98–102], and simulations with explicit solid-liquid equilibrium[103,104]. Bearing this in mind, the objective of this work is to evaluate the reliability of the Reaction Field method to be used in the calculation of interfacial properties in inhomogeneous systems through the comparison with the values obtained using the strictly correct Ewald method. Kolafa et al.[105] recently published an analysis of the treatment of electrostatic interactions, applied to TIP4P/2005[106] water, focusing mainly on the performance of various

short-range approximations. In their work Ewald sums and RF performance are compared, but only in the case of bulk fluid properties.

With the aim already stated, water has been selected as benchmark molecule for its practical relevance. Many papers have been devoted so far to the determination of different water models interfacial properties using molecular simulation, as reviewed for instance by Wang and Zeng[107]. Vega and de Miguel[1] presented an updated critical review of previously published water interfacial tension values, obtained using the most popular rigid non polarizable molecular models, together with their own results, obtained using both the mechanical and thermodynamic (TA method) routes. The same procedure will be applied in this case with the aim to establish a quantitative comparison with their results. Following their approach, SPC/E[108], TIP4P[109], TIP4P/Ewald[110] and TIP4P/2005[106] water models were tested. All these models consider a rigid molecular geometry with a LJ center and point electric charges.

## 2.3 Models and simulation details

The TIP4P-type models[106,109,110] for water consist of four interacting sites placed on the oxygen atom (O), on each of the hydrogen atoms (H, H), and along the H-O-H bisector (the so-called M site). The SPC/E model for water[108] differs from the previous ones in that the M site is not considered. The molecular geometry (bond distances and angles), as well as the values of the

Lennard-Jones (LJ) parameters, $\epsilon$ and $\sigma$, and the charges $q$ of the sites are given in Table 8.1.

Table 2.1: Lennard-Jones parameters, $\epsilon$ and $\sigma$, partial charges $q$, and geometries, of the different used water models.

| *Site* | $\epsilon/\kappa(K)$ | $\sigma(\mathring{A})$ | $q(e)$ | *Geometry* |
|---|---|---|---|---|
| | | $TIP4P/2005$ | | |
| $O$ | 93.20 | 3.1589 | 0.0 | $O-H: 0.9572\mathring{A}$ |
| $H$ | 0.0 | 0.0 | 0.5564 | $O-M: 0.1546\mathring{A}$ |
| $M$ | 0.0 | 0.0 | $-1.1128$ | $H-O-H: 104.52°$ |
| | | $TIP4P/Ew$ | | |
| $O$ | 81.9 | 3.16435 | 0.0 | $O-H: 0.9572$ |
| $H$ | 0.0 | 0.0 | 0.52422 | $O-M: 0.125\mathring{A}$ |
| $M$ | 0.0 | 0.0 | $-1.04844$ | $H-O-H: 104.5°$ |
| | | $TIP4P$ | | |
| $O$ | 78.0 | 3.154 | 0.0 | $O-H: 0.9572\mathring{A}$ |
| $H$ | 0.0 | 0.0 | 0.52 | $O-M: 0.15\mathring{A}$ |
| $M$ | 0.0 | 0.0 | $-1.04$ | $H-O-H: 104.5°$ |
| | | $SPC/E$ | | |
| $O$ | 1.0 | 1.0 | $-0.8476$ | $O-H: 0.9572\mathring{A}$ |
| $H$ | 0.0 | 0.0 | 0.4238 | $H-O-H: 104.5°$ |

For these models, the intermolecular interactions between sites, $a$ and $b$, of different molecules, are defined by the site-site potential defined as follows:

$$u_{ab} = 4\epsilon_{ab}\left(\left(\frac{\sigma_{ab}}{r_{ab}}\right)^{12} - \left(\frac{\sigma_{ab}}{r_{ab}}\right)^{6}\right) + \frac{q_a q_b}{r_{ab}} \tag{2.1}$$

where $r_{ab}$ is the distance between sites, and $\epsilon_{ab}$ and $\sigma_{ab}$ are the LJ cross parameters computed from $\epsilon_a$, $\epsilon_b$ and $\sigma_a$, $\sigma_b$, respectively, using the geometrical

mean as imposed by the TIP4P-type and SPC/E models.

The LJ contribution to the internal energy was computed with a spherical cut-off radius ($r_c$), and no further long range corrections (LRCs). Although several authors have proposed analytical expressions for the determination of LJ LRCs in inhomogeneous systems[69,111], beyond a certain value, the cut-off radius is expected not to affect the calculations in the case of water, as it represents a minor contribution if compared with the electrostatic term[107]. The cut-off radius was set in this case to 12.5 $\mathring{A}$ and the justification of this choice is given below. The coulombic interactions were dealt with the RF method as proposed by Neumann[83], using the same cut-off radius that for the LJ interactions. Thus, the energy $U_i$ of the $i$-th molecule is calculated during the simulation as follows:

$$F = \sum_{j \neq i} \sum_{a} \sum_{b} u^*_{ab} \tag{2.2}$$

$$u^*_{ab} = 4\epsilon_{ab} \left( \left( \frac{\sigma_{ab}}{r_{ab}} \right)^{12} - \left( \frac{\sigma_{ab}}{r_{ab}} \right)^{6} \right) + \frac{q_a q_b}{r_{ab}} \left( 1 + \frac{\epsilon_{RF} - 1}{2\epsilon_{RF} + 1} \left( \frac{r_{ab}}{r_c} \right)^3 \right) \tag{2.3}$$

In this expression, index $j$ runs for all the molecules placed within the sphere of radius $r_c$ centered in the $i$-th molecule, and $a$ and $b$ denote the interacting sites of the different water molecules. As it can be seen, the interaction energy between sites $u_{ab}$ (Eq 7.1) must be slightly modified (now $u^*_{ab}$) in order to account properly for the interaction of the molecules with the surround-

ing dielectric media (see Neumann[83] for details). In this expression, $\epsilon_{RF}$ is the dielectric constant of the surrounding media. For moderately of highly polar liquids, as it is the case for water ($\epsilon_{RF}$=78.5), the value of the factor $(\epsilon_{RF}-1)/(2\epsilon_{RF}+1)$ is close to 0.5, corresponding to $\epsilon_{RF}=\infty$, i. e., the conducting boundary condition, that has been assumed in this case.

Interfacial properties for the cited water models were determined using byphasic constant volume (NVT ensemble) Monte Carlo simulations. The calculations were performed using our own code, and the interfacial properties at each temperature and pressure were determined through a two step procedure. First, a cubic box containing $N$=1024 water molecules was considered, which were initially placed at random and then equilibrated under isothermal-isobaric (NPT) conditions. Once the equilibration was achieved, two equal size empty boxes were added at both sides of the former one, in the $z$ direction, obtaining a parallelepipedic box where $L_x$=$L_y$=$L_z$/3. This byphasic simulation box was then allowed to evolve at constant volume (NVT) conditions, until two parallel vapour liquid interfaces are fully equilibrated. The box was divided into 100 parallel slabs in the $z$ direction in order to study the interfacial density profile and coexisting phase densities. In this step, the center of mass of the simulation box was monitored and kept at the center of the box to avoid density profile fluctuations. Minimum image conventions and fully periodic boundary conditions were considered as usual. Simulations were arranged in cycles, every one of them consisting in $N$ attempts to either displace

or rotate a randomly chosen molecule (both movements with equal probability), plus one volume change try in the case of bulk NPT calculations. Each movement was adjusted during the run to approach a 30% acceptance ratio. In the byphasic simulations, each run consisted of $10^6$ equilibration followed by $5 \times 10^6$ production cycles.

Interfacial tension was computed using both the thermodynamic route, using the cited TA method[63], and the mechanical route. The latter entails the calculation of two pressure components, normal and tangential to the interface. This calculation has been done following the method proposed by de Miguel and Jackson[66]. Determination of interfacial tension from pressure components is then straightforward. Coexisting phase densities were determined from density profiles, which were averaged along the production run. Excluding the interface, liquid density was computed as the average of the 25 central slabs in the profile, while the vapour phase density is the average of the two sets of 25 slabs at each box end, and the uncertainties were determined in this case to be the standard deviations of the independent slab density values.

## 2.4 Results and discussion

First of all, a preliminary analysis is necessary to show the reliability of our election of the cut-off radius and also the ability of our code to accurately compute interfacial properties. To this end, coexisting densities and interfacial

tension were computed at 400 and 450 K for the TIP4P water model, using different cut-off values, spanning from 4 to 8 times $\sigma_{LJ}$ ($\sigma_{LJ} = 3.154\mathring{A}$), with no LJ LRCs. In these simulations, the coulombic interactions were computed using the Ewald sums method using the same cut-off radius for the real space contribution of the Ewald sums than for the LJ term. The screening parameter and the number of vectors in the reciprocal space have been carefully selected in order to achieve convergence. The results are shown in Table 5.1, compared to the data of Vega and de Miguel[1], that were obtained in a equivalent way. As it can be seen, both the election of the cut-off radius and correctness of our code are certified. Both interfacial tension values agreed to within the calculation uncertainty, determined by block averaging.

Table 2.2: Simulation data of coexisting densities ($\rho_l$ and $\rho_v$, both in kg m$^{-3}$) and surface tension ($\gamma$ in mJ m$^{-2}$) for the TIP4P water model. Subscripts $ta$ and $mr$ stand for Test-Area and mechanical route, respectively. The Ewald sums method was used in the simulations to handle electrostatic interactions, and a constant LJ cut-off radius $r_c = 12.5\mathring{A}$ was used. These values are compared with those obtained by Vega and de Miguel[1] using the same procedure.

| $r_c/\mathring{A}$ | $\rho_l$ | $\rho_l$ [1] | $\rho_v$ | $\rho_v$ [1] | $\gamma_{ta}$ | $\gamma_{mr}$ | $\gamma$ [1] |
|---|---|---|---|---|---|---|---|
| 400 K | | | | | | | |
| 12.5 | 895(2) | 896(1) | 2.0(1) | 2.1(1) | 35.6(5) | 35.6(5) | 36.8(1.5) |
| 17.3 | 896(3) | | 2.1(1) | | 36(2) | 36(1) | |
| 25.2 | 897(3) | | 2.2(1) | | 36(1) | 36(1) | |
| 450 K | | | | | | | |
| 12.5 | 825(1) | 825(1) | 8.1(3) | 7.8(1) | 24(2) | 24(1) | 26.0(1.7) |
| 25.2 | 827(1) | | 7.7(2) | | 25(1) | 25(1) | |

## 2.4. RESULTS AND DISCUSSION

After this preliminary verification, the key of this work is the comparison of the treatment of electrostatic interactions with Ewald sums and the RF method, for the set of water molecular models cited above. Table 5.2 summarizes the results obtained at temperatures from 350 to 500 K.

Table 2.3: Simulation data of coexisting densities ($\rho_l$ and $\rho_v$, both in kg m$^{-3}$) and surface tension ($\gamma$/ mJ m$^{-2}$), for the different water molecular models tested. Subscripts *ta* and *mr* stand for Test-Area and mechanical route, respectively . The reaction field method was used in the simulations to handle electrostatic interactions, and a constant LJ cut-off radius $r_c = 12.5\mathring{A}$ was used. These values are compared with those obtained by Vega and de Miguel[1] using the Ewald sums method.

| $T/K$ | $\rho_l$ | $\rho_l$[1] | $\rho_v$ | $\rho_v$[1] | $\gamma_{ta}$ | $\gamma_{mr}$ | $\gamma_{ta}$[1] |
|---|---|---|---|---|---|---|---|
| | | | | $TIP4P/2005$ | | | |
| 350 | 966(5) | 968(2) | 0.034(9) | 0.060(3) | 59(2) | 60(2) | 58.2(1.3) |
| 400 | 929(1) | 931(1) | 0.63(2) | 0.60(3) | 50(1) | 51(2) | 49.3(1.4) |
| 450 | 878(3) | 880(1) | 2.5(2) | 2.5(2) | 40(4) | 40(4) | 39.6(1.3) |
| 500 | 817(2) | 816(2) | 7.5(2) | 7.3(3) | 29(2) | 29(2) | 28.4(0.8) |
| | | | | $TIP4P/Ew$ | | | |
| 350 | 961(5) | 964(2) | 0.11(2) | 0.11(1) | 53(3) | 53(4) | 54.5(1.9) |
| 400 | 919(2) | 922(2) | 0.78(3) | 0.68(8) | 44(1) | 43.9(9) | 45.5(1.5) |
| 450 | 868(3) | 866(1) | 2.9(1) | 3.2(1) | 34.6(6) | 34.1(7) | 35.6(1.6) |
| 500 | 799(2) | 796(1) | 9.4(2) | 9.8(3) | 25(2) | 25(4) | 24.1(0.6) |
| | | | | $TIP4P$ | | | |
| 350 | 951(2) | 950(3) | 0.24(2) | 0.40(5) | 46(1) | 45(1) | 47.0(1.2) |
| 400 | 898(1) | 896(1) | 2.4(1) | 2.1(1) | 36(1) | 36(1) | 36.8(1.5) |
| 450 | 824(1) | 825(1) | 8.1(1) | 7.8(1) | 25.6(7) | 25.4(9) | 26.0(1.7) |
| 500 | 729(1) | 727(2) | 25(1) | 31(1) | 14.5(9) | 14.5(7) | 16.5(1.1) |
| | | | | $SPC/E$ | | | |
| 350 | 958(4) | 962(1) | 0.011(4) | 0.092(3) | 51(3) | 50(4) | 52.1(1.3) |
| 400 | 914(2) | – | 0.70(2) | – | 43(1) | 44(2) | – |
| 450 | 858(2) | 860(2) | 3.1(1) | 3.1(2) | 33.8(6) | 34(1) | 35.0(1.0) |
| 500 | 790(1) | 788(2) | 8.7(2) | 10(2) | 25(2) | 25(2) | 24.3(1.5) |

All liquid densities and interfacial tension values are compatible, agreeing within the computed error bars, with the values presented by Vega and de Miguel[1], using in their case Ewald sums. Some differences can be found for the vapour phase densities at the lower temperatures tested, but the use of molecular simulation to determine these low vapour densities is known to offer unreliable results. Except for these differences, both techniques for handling electrostatic interactions perform practically the same from a quantitative point of view. The interfacial tension results for the different models are plotted in Fig. 2.1, showing the equivalence of both calculation techniques.

This means that the use of the RF method can help to significatively reduce computing times, without loss of accuracy in the determination of interfacial properties, for the type of molecular models similar to the ones tested in this case. A further step in this direction could be the extension of this preliminary study to molecules with non spherical structure, as for instance chain molecules as linear alkanols. In the case studied here, the typical CPU time with our code for a given point with Ewald sums was three to four times longer than the corresponding with RF, a fact that should be considered in addition to the ease of implementation of RF compared to Ewald sums or the PME method. Finally, the inclusion in the code of other saving time methods, as the cell list, might further shorten computing times, improving the feasibility of analyzing more complex systems.

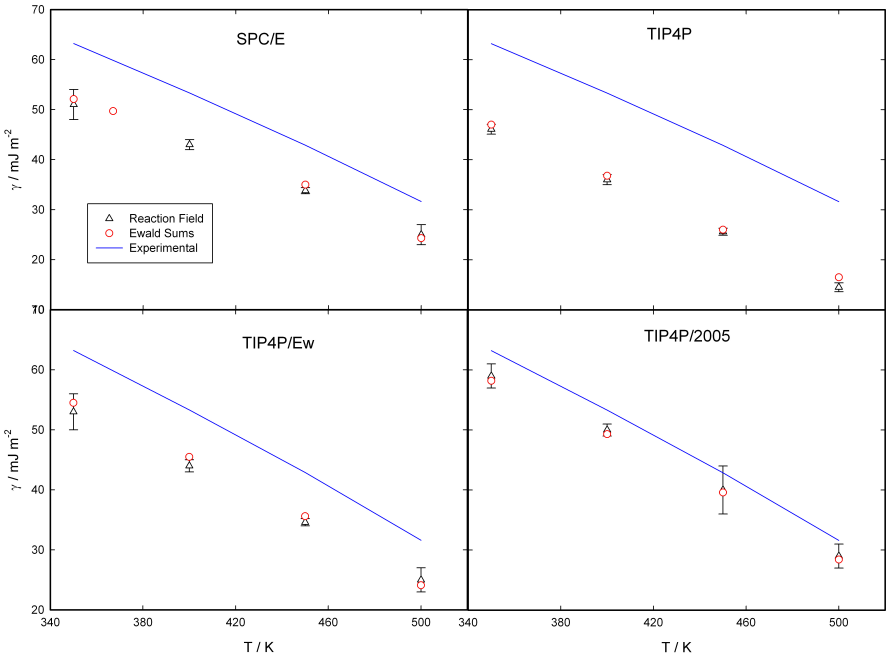


Figure 2.1: Comparison of calculated interfacial tension values for different water molecular models: this work (triangles), Vega and de Miguel [1] (squares), and experimental values (solid line).

# Chapter 3

# Influence of the long-range corrections on the interfacial properties of molecular models using Monte Carlo simulation

## 3.1 Abstract

We analyze the influence of the long-range corrections, due to the dispersive term of the intermolecular potential energy, on the interfacial tension using direct simulation of the vapour-liquid interface of different molecular models. Although several calculation methods have been proposed recently to compute the fluid-fluid interfacial properties, the truncation of the intermolecular potential or the use of the tail corrections represents a contribution relevant from a quantitative perspective. In this work, a simplified model for methane, namely a spherical Lennard-Jones intermolecular potential, has been considered first, and afterwards other models including rigid non polarizable structures with both Lennard Jones sites and point electric charges, representing some of the most popular models to describe water and carbon dioxide have been studied. Our results show that for all cases tested, including those in which the electrostatic interactions may be predominant, an incomplete account of the long-range corrections produces a systematic underestimation of the computed interfacial tension.

## 3.2 Introduction

The prediction of thermodynamic and structural properties of molecular models comprising intermolecular dispersive interactions and long-range Coulombic forces, such as puntual charges for modelling electrostatic inter-

actions, has been until recently a challenging problem especially for systems exhibiting any kind of inhomogeneity. Particularly difficult to account for has been the long-range corrections (LRCs) associated to the truncation of the potential of the dispersive forces. Although the effect of this truncation on different thermodynamic and structural properties might seem to be negligible, due to the small contribution of dispersive interactions if compared with electrostatic forces on the total energy, this is not the case for the vapour-liquid surface tension. Since this property is one of the most sensitive magnitudes when it is calculated along a computer simulation run, a very precise evaluation of the inhomogeneous LRCs due to the dispersive interactions is necessary. Otherwise, the quantitative performance of a given molecular model to estimate interfacial properties might not be evaluated properly, yielding misleading conclusions. The objective of this paper is to study the influence of the LRCs, due to the dispersive interactions, on the vapour-liquid interfacial tension of several realistic molecular models that combine dispersive and Coulombic interactions. In particular, we consider methane, which is described through the united-atom approach as a single Lennard Jones (LJ) sphere, and water and carbon dioxide, which are treated as rigid non polarizable molecules containing several interacting sites, including both LJ dispersive interaction sites and puntual electric charges.

Until very recently, there was not an easy, simple, and precise method for evaluating the LRCs due to the dispersive interactions in inhomogeneous sys-

tems. The first method intended to account for the LRCs was proposed by Chapela *et al.*[112], and was later modified by Blokhuis *et al.*[113]. Although this methodology provides a lower bound to the surface tension (and other thermodynamic properties), its main drawback is that it employs density profiles of the system determined without LRCs.

The first satisfactory methodology for dealing with LRCs for inhomogeneous systems was proposed by Guo and Lu[114], a procedure extensively used later by Malfreyt and co-workers[34,69,115–118]. Although the method takes into account the LRCs to the energy and other properties, the presence of a non local term in the final expression involving an integral over density makes the procedure somewhat inconvenient for run time calculations. In addition to that, although the non-local term seems to represent a relatively low contribution to the surface tension at low temperature, it becomes important close to the critical point[111]. For further details see the original work[114] and the review by MacDowell and Blas[119].

The same conceptual procedure accounting for the LRCs was recently proposed by Janeček[111], based on related works of Mecke *et al.*[120,121] and Daoulas *et al.*[122], applied by several authors[123–126], and later modified by MacDowell and Blas[119]. The Janeček's method accounts very accurately for the LRCs in inhomogeneous systems along the whole range of temperatures in which the system exhibits vapour-liquid coexistence, and what is more important, the method has been shown to be very robust concerning the choice of the

cut-off distance. A step further, the improved Janeček's method proposed by MacDowell and Blas[119] is able to evaluate in an exact way the intermolecular interactions without the need of computing the instantaneous density profile to calculate the LRCs to the intermolecular potential energy. With this new formulation, the method can be implemented in a compact and straightforward fashion in any standard Monte Carlo computer simulation code, since the final expression is given by an effective pairwise intermolecular potential between all the particles forming the system[119]. Another approach to the problem is the use of Ewald sums to deal also with dispersive interactions. This method has been applied by int Veld *et al.*[127] and Alejandre and Chapela[128], but it is definitely much more complex from a mathematical point of view than other techniques, such as the Janeček's methodology. In addition to that, it is remarkably CPU time demanding, adding up to the already lengthy inhomogenous simulation runs.

The rest of the paper is organized as follows. in Sec. II we consider an improved method for determining the LRCs of inhomogeneous molecules. Molecular models and the simulation details of this work are presented in Sec. III. Results obtained are discussed in Sec. IV. Finally, in Sec. V we present the main conclusions.

## 3.3 Improved Janeček's methodology: The effective long-range pairwise potential

In 2006, Janeček[111] proposed a new methodology for calculating the LRCs to the potential energy in systems that interact through spherically symmetric intermolecular potentials. This procedure allows to treat in a simple way the truncation of the intermolecular energy of systems that exhibit planar interfaces. More recently, MacDowell and Blas[119] have demonstrated that the Janeček's procedure can be rewritten into an effective long-range pair potential that allows a fast, easy, and elegant implementation of method. Since the original and improved methodologies have been described elsewhere[111,119,123], only a brief account of the most important details will be presented here.

Consider a system of $N$ molecules contained in a volume $V$ that interact through a pairwise intermolecular potential. The total intermolecular potential energy can be written as

$$U(r_{ij}) = \frac{1}{2}\sum_{i=1}^{N}\sum_{j=1}^{N} u(r_{ij}) = \frac{1}{2}\sum_{i=1}^{N} U_i \tag{3.1}$$

where $u(r_{ij})$ is the intermolecular potential between particles $i$ and $j$, that depends on the distance between the centres of molecules $r_{ij} \equiv |\mathbf{r}_i - \mathbf{r}_j|$, and $U_i$ is the potential energy of molecule $i$ due to the interactions with all molecules of the system. During a simulation, the potential energy of a particle is usually

splitted into two contributions: one arising from the interaction of molecule $i$ with all molecules inside a sphere of radius $r_c^{(i)}$ centered at this molecule, and a second term that corresponds to the interaction between the molecule $i$ and the rest of molecules forming the system (i.e., all the molecules located outside the cut-off distance). The potential energy of a molecule $i$ can be then written as

$$U_i = \sum_{j \in r_c^{(i)}} u(r_{ij}) + U_i^{LRC} \tag{3.2}$$

where $r_c^{(i)}$ is the so-called cut-off distance of particle $i$, the notation $j \in r_c^{(i)}$ denotes all the particles $j$ located inside the cut-off sphere centered at the position of particle $i$, and $U_i^{LRC}$ represents the intermolecular interactions between particle $i$ and the rest of the system due to long-range corrections. Note that $r_c^{(i)} \equiv r_c$ since all molecules have actually the same cut-off distance.

In the original Janeček's methodology, the simulation box is divided into slabs parallel to the $xy$-plane (and to the planar interface), in such a way that if the width of these slabs is small enough the number density of the system $\rho(z)$ is approximately constant inside each of them. Here we have choosen the $z$-axis as the direction perpendicular to the planar interface. If one assumes that the pair correlation function between two particles separated beyond the cut-off distance is equal to one, i.e., the distribution of particles separated a distance $r_{ij} \geq r_c$ is uniform, the intermolecular potential associated to the long-range correction, of a particle $i$ located at position $z_i$ (according to Janeček's original

method[111]), is given by

$$U_i^{LRC}(z_i) = \sum_{k=1}^{n_s} w(|z_i - z_k|)\rho(z_k)\Delta z \tag{3.3}$$

where $\rho(z_k)$ is the density of the system in the slab of width $\Delta z$ and centered at $z_k$, the index $k$ runs for all the $n_s$ slabs in which the simulation box is divided along the $z$-axis, and $w(|z_i - z_k|)$ accounts for the intermolecular interactions due to the long-range correction between a particle $i$ at $z_i$ and all the particles located inside the slab centered at $z_k$ and with a number density $\rho(z_k)$. The particular expression for $w(|z_i - z_j|)$ depends on the election of the intermolecular potential of the system. In the original Janeček's method, applicable for molecules interacting through the Lennard-Jones (LJ) intermolecular potential, the function $w(z)$ is given by

$$\omega(z) = \begin{cases} 4\pi\epsilon\sigma^2 \left[ \frac{1}{5}\left(\frac{\sigma}{r_c}\right)^{10} - \frac{1}{2}\left(\frac{\sigma}{r_c}\right)^{4} \right] & \text{if } z < r_c \\ 4\pi\epsilon\sigma^2 \left[ \frac{1}{5}\left(\frac{\sigma}{z}\right)^{10} - \frac{1}{2}\left(\frac{\sigma}{z}\right)^{4} \right] & \text{if } z > r_c \end{cases} \tag{3.4}$$

The total contribution to the energy obtained from the long-range corrections is given then as a sum over individual contributions, of course with a factor of 1/2 to avoid including mutual interactions twice,

$$U^{LRC} = \frac{1}{2}\sum_{i=1}^{N} U_i^{LRC}(z_i) \tag{3.5}$$

## 3.3. IMPROVED JANEČEK'S METHODOLOGY

Eqs. 3.3, 3.4, and 3.5 constitute the original Janeček's method for estimating the energetic contribution due to long-range corrections. Although this method allows to calculate very accurately the long-range corrections of a LJ system that exhibits a planar interface, it has several drawbacks. The most important one is the calculation of the density profile on the fly, i.e., the need to recalculate the instantaneous density profile every step to be used in Eq. 3.3 and hence, to be able to calculate the tail corrections at each Monte Carlo step. Unfortunately, this makes the procedure cumbersome, especially in the case of molecular fluids[119], and also complicated to code since the density profile must be updated each Monte Carlo step. The improved methodology proposed recently by MacDowell and Blas[119] is simple and elegant, and it is also easier to implement in a simulation code. The original Janeček's method assumes that $U_i^{LRC}(z_i)$ is given by a discrete sum of $n_s$ contributions due to each slab in which the simulation box is divided along the $z$-axis (see Eq. 3.3). In the improved procedure of MacDowell and Blas[119] Eq. 3.3 is given by the more accurate expression

$$U_i^{LRC}(z_i) = \int_{-\infty}^{+\infty} w(|z_i - z|)\, \rho(z)\, dz \tag{3.6}$$

where the discrete approximation given by Eq. 3.3 is replaced by the continuous expression of $U_i^{LRC}(z_i)$. Using this formulation, the density profile of a system formed by $N$ particles can be written formally as a summation of

$\delta$-Dirac distributions centered at the positions $z_j$, with $j = 1, \ldots, N$

$$\rho(z) = \frac{1}{\mathcal{A}} \sum_{j=1}^{N} \delta(z - z_j) \tag{3.7}$$

where $\mathcal{A}$ is the interfacial area of the $xy$-plane of the system. Note that the density is normalized appropriately since

$$\int_V \rho(z)\, dV = N \tag{3.8}$$

Substituing Eq. 3.7 into Eq. 3.6 we have

$$U_i^{LRC}(z_i) = \int_{-\infty}^{+\infty} w(|z_i - z|)\, \frac{1}{\mathcal{A}} \sum_{j=1}^{N} \delta(z - z_j)\, dz \tag{3.9}$$

and using the property of the $\delta$-Dirac distribution, we obtain the final expression for $U_i^{LRC}(z_i)$

$$U_i^{LRC}(z_i) = \frac{1}{\mathcal{A}} \sum_{j=1}^{N} w(|z_i - z_j|) \tag{3.10}$$

Note that the sum in the previous equation runs over all the values of the index $j$ ($j = 1, \ldots, N$), and this also includes the case $j = i$.

The total intermolecular interaction energy arising from the long-range corrections, given by Eq. 3.5, is then expressed as

$$U^{LRC} = \frac{1}{2\mathcal{A}} \sum_{i=1}^{N} \sum_{j=1}^{N} w(|z_i - z_j|) \tag{3.11}$$

The unrestricted summation over indexes $i$ and $j$ can be finally transformed into a sum of pairwise effective (integrated) intermolecular potential over all the pairs of molecules in the system and $N$ self-energy terms as

$$U^{LRC} = \frac{1}{\mathcal{A}} \sum_{i=1}^{N-1} \sum_{j=i+1}^{N} w(|z_i - z_j|) + \frac{1}{2\mathcal{A}} \sum_{i=1}^{N} w(0) \tag{3.12}$$

The expressions given by Eqs. 3.10 and 3.12 are the key relationships of the improved version proposed by MacDowell and Blas[119]: the interaction energy due to the long-range corrections is given by an effective pairwise intermolecular potential between all the particles forming the system.

Each of the self-energy terms arising from the last contribution of Eq. 3.12 has a clear physical meaning that can be explained very easily by inspecting carefully Eq. 3.10. As previously mentioned, the intermolecular potential of particle $i$ at $z_i$, due to the long-range corrections, includes $N$ terms, being one of them a self-energy contribution arising from the case $j = i$ in Eq. 3.10. What is the physical meaning of this contribution? It is not for sure a truly self-energy term in the real sense since this has not physical reality. This is easily understandable since the funtion $w(z)$ is not a real intermolecular potencial between two particles but an effective (integrated) potential. Focussing on Eq. 3.10, each contribution $\frac{1}{\mathcal{A}} w(|z_i - z_j|)$ (with $i = 1, \ldots, N$) represents the intermolecular potential, due to the interactions between the particle $i$ with all the particles located inside the slab centered at $z_j$ that are outside the cut-off

sphere (i.e., due to the long-range interactions). Therefore, $w(0)$ represents the interaction of a given $i$ particle with those others placed in the same density profile slab but located beyond the cut-off distance, and not a truly self-energy term in the real sense.

This procedure results in several important advantages over the original method:

- Eqs. 3.10 and 3.12 correspond to the exact evaluation of the intermolecular interactions due to the long-range corrections. It is important to recall that the use of the original Janeček's version of the method implies a discretization of the simulation box along the $z$-axis, which is in fact an approximation.

- The improved procedure allows to evaluate $U_i^{LRC}$ and $U^{LRC}$ without the explicit calculation of the density profile on the fly, i.e., it is not necessary to update the density profile $\rho(z)$ each Monte Carlo step. Just to give an order of magnitude, if the simulation of the vapour-liquid interface of a LJ system is equilibrated typically during $10^6$ Monte Carlo cycles, and in each cycle we attempt to move $N$ molecules ($N \sim 10^3$ molecules), the density profile of the system should be updated $10^9$ times along the equilibration stage.

- Finally, the implementation of the method is straightforward. If one has a standard Monte Carlo code in the canonical ensemble, the only change

needed is to include a new subroutine for the evaluation of the contribution to the total intermolecular energy due to the long-range corrections (at the start of the simulation), and an additional subroutine for calculating the contribution to the intermolecular energy of a given particle due to the long-range corrections (each time a molecule displacement is attempted).

## 3.4 Models and simulation details

In this work we investigate the effect of LRC due to the dispersive interactions on the interfacial properties of three different molecular systems, methane, water, and carbon dioxide. There are several reasons for this choice. First at all, the molecules are modelled following the united-atom approach, and in particular, accounting for the dispersive interactions through the LJ intermolecular potential. In a previous work[129], the influence of the method used to account for coulombic interactions in the calculation of interfacial properties for various water models was analyzed, showing the equivalence between Ewald summation and the reaction field (RF) method in this application. Therefore, we evaluate now the effect of the LRCs due to the dispersive interations on different interfacial properties, with special emphasis on surface tension. Another reason for the choice of these molecules is their undeniable applied interest in many fields, and in particular in the study of enhanced

natural gas recovery and carbon dioxide stockage, in which their phase equilibria[130] and interfacial properties[70,131] play a key role. In addition to that, the existence of very accurate experimental data for all the substances considered in this work allows to establish a comparison between the performance of different models for the same substance, evaluating the quantitative efficiency of each one in predicting interfacial properties.

Methane is modelled, following the united-atom approach, as a single LJ sphere to account for, in an effective way, the nearly spherically symmetric dispersive interactions[132,133]. For the case of carbon dioxide, the most usual model is a linear-rigid chain molecule with three chemical units, representing each of the C and O atoms, and each unit or interacting site consists of a combination of a LJ site plus an electric point charge. The molecule is considered to be rigid and non polarizable. This structure mimics the typical anisotropic feature of carbon dioxide, including the large quadrupole moment value accounted for the three partial charges. Among the available parametrizations for this molecular structure, in this case the original version of the MSM[134–136] model, as well as those denoted as EPM2[15], TraPPE[137], and Zhang and Duan[138] models, were tested. In the case of water, the well-known original TIP4P molecular model[109] and two modifications of it, the TIP4P/Ew[110] and TIP4P/2005[106] models, were also studied. All of them share the same site definition and molecular geometry: four interacting centers, with the oxygen atom O as the only LJ interaction site, a partial charge

(M-site) located along the H-O-H angle bisector, and two hydrogen atoms H, which are represented by partial point electric charges. Table 3.1 summarizes the characteristic parameters for all the molecular models studied in this work.

Table 3.1: Lennard-Jones potential well depth $\epsilon$ and size $\sigma$, partial charges $q$, and geometry, of the $CH_4$, $H_2O$ and $CO_2$ models used.

| *Atom* | $\epsilon/\kappa(K)$ | $\sigma$(Å) | $q(e)$ | *Geometry* |
|---|---|---|---|---|
| $CH_4$ [132,133] | 149.92 | 3.7327 | 0 | |
| $TIP4P$ $H_2O$ [109] $O$ | 78.0 | 3.154 | 0.0 | $O-H$ : 0.9572Å |
| $H$ | 0.0 | 0.0 | 0.52 | $O-M$ : 0.15Å |
| $M$ | 0.0 | 0.0 | −1.04 | $H-O-H$ : 104.5° |
| $TIP4P/Ew$ [110] $H_2O$ $O$ | 81.9 | 3.16435 | 0.0 | $O-H$ : 0.9572Å |
| $H$ | 0.0 | 0.0 | 0.52422 | $O-M$ : 0.125Å |
| $M$ | 0.0 | 0.0 | −1.04844 | $H-O-H$ : 104.5° |
| $TIP4P/2005$ [106] $H_2O$ | | | | |
| $O$ | 93.20 | 3.1589 | 0.0 | $O-H$ : 0.9572Å |
| $H$ | 0.0 | 0.0 | 0.5564 | $O-M$ : 0.1546Å |
| $M$ | 0.0 | 0.0 | −1.1128 | $H-O-H$ : 104.52° |
| $MSM$ [134–136] $CO_2$ | | | | |
| $C$ | 29.0 | 2.785 | 0.5957 | $C-O$ : 1.16Å |
| $O$ | 83.1 | 3.014 | −0.29785 | $O-C-O$ : 180° |
| $EPM2$ [15] $CO_2$ | | | | |
| $C$ | 28.129 | 2.757 | 0.6512 | $C-O$ : 1.149Å |
| $O$ | 80.507 | 3.033 | −0.3256 | $O-C-O$ : 180° |
| $TraPPE$ [137] $CO_2$ | | | | |
| $C$ | 27.0 | 2.80 | 0.70 | $C-O$ : 1.16Å |
| $O$ | 79.0 | 3.05 | −0.35 | $O-C-O$ : 180° |
| $Zhang-Duan$ [138] $CO_2$ | | | | |
| $C$ | 28.845 | 2.7918 | 0.5888 | $C-O$ : 1.163Å |
| $O$ | 82.656 | 3.0 | −0.2944 | $O-C-O$ : 180° |

Following the ensuing discussion, the pairwise intermolecular potential be-

tween molecules $i$ and $j$ may now be written as,

$$u(r_{ij}) = \sum_{a=1}^{n_a} \sum_{b=1}^{n_b} u_{ab}(r_{ab}) \tag{3.13}$$

where $n_a$ and $n_b$ are the numbers of sites in the molecules $i$ and $j$, respectively. $u_{ab}(r_{ab})$, the interaction potential between two sites of molecules $i$ and $j$, is given by,

$$u_{ab}(r_{ab}) = 4\epsilon_{ab} \left[ \left( \frac{\sigma_{ab}}{r_{ab}} \right)^{12} - \left( \frac{\sigma_{ab}}{r_{ab}} \right)^{6} \right] + \frac{1}{4\pi\epsilon_0} \frac{q_a q_b}{r_{ab}} \tag{3.14}$$

where $r_{ab}$ is the distance between interacting sites $a$ and $b$ in molecules $i$ and $j$, respectively, $\sigma_{ab}$ and $\epsilon_{ab}$ are the size and dispersive energy parameters associated to the LJ dispersive interactions between a pair of $a$ and $b$ sites in these molecules, and $q_a$ and $q_b$ are the partial charges on these sites, with $\epsilon_0$ the vacuum permittivity. Note that in the case of interactions involving methane, the coulombic term is always equal to zero. The unlike LJ parameters $\epsilon_{ab}$ and $\sigma_{ab}$ are given by the Lorentz-Berthelot combining rules,

$$\epsilon_{ab} = \sqrt{\epsilon_{aa}\epsilon_{bb}} \tag{3.15}$$

$$\sigma_{ab} = \frac{1}{2} \left( \sigma_{aa} + \sigma_{bb} \right) \tag{3.16}$$

where $\sigma_{kk}$ and $\epsilon_{kk}$ are the LJ size and dispersive energy parameters of a $k$-type interacting site.

Molecular simulations were initially started from a cubic box of size $L_x =$

$L_y = L_z > 10\sigma$, where $\sigma$ stands for the typical size of each molecular model used in this work. Systems containing $N = 1024$ molecules were equilibrated at constant temperature and pressure, in the isothermal-isobaric or $NPT$ ensemble. Typically, the system was equilibrated, starting from an initial bcc ordered configuration, during $5 \times 10^6$ Monte Carlo cycles. Once the system was equilibrated, the original cubic box containing the system was placed between two equal size empty boxes added at both sides along the $z$ direction. The simulations continued then in the $NVT$ canonical ensemble. At temperatures below the critical temperature, the system spontaneously develops two parallel vapour-liquid interfaces perpendicular to the $z$-axis of this byphasic simulation box, allowing to study the properties of interest, including vapour-liquid surface tension and interfacial thickness, among others.

The $NPT$ and $NVT$ Monte Carlo simulations were organized in cycles. Each cycle consisted of $N$ attempts of displacement (translation, and also rotation in the case of non-spherical molecular models) of a molecule selected at random, plus one volume change try in the case of $NPT$ simulations. The type of move was selected randomly with fixed probabilities. The acceptance ratios for translational, rotational moves and volume changes were tuned to approximately 30%. Minimum image convention and periodic boundary conditions were considered. The simulation box was divived into 100 parallel slabs along the $z$-axis in order to calculate the vapour-liquid density profile. In the byphasic simulations, after an initial equilibration period of $5 \times 10^5$ cycles,

we generated tipically $2 \times 10^6$ additional cycles to accumulate averages of the desired interfacial properties. The uncertainties of the simulated results were obtained using block averaging, by dividing the simulation run in ten subsets.

The total LJ contribution to the intermolecular interaction energy was computed using two different approaches. The first one entailed the use of a spherical cut-off distance ($r_c$) to truncate the interaction, considering no LRCs, i.e., neglecting the contribution to the intermolecular potential energy of pairs of molecules separated by a distance larger than this cut-off value. The second method consisted in the use of a spherical cut-off distance ($r_c$) and the LRCs evaluation method proposed by Janeček[111] following the improved formulation of MacDowell and Blas[119]. This allowed us to determine the relevance of this particular term in the calculation of interfacial properties.

In this work we also use two different approaches to account for the coulombic interactions, i.e., the reaction field methodology and the Ewald sums. Here we only explain the most important features of both techniques. In the Reaction Field (RF) method, the same cut-off distance is used as that for the LJ interactions. In this case, the coulombic interaction energy between two point charges, $u_{coul}$, is computed as follows:

$$u_{coul} = \frac{q_a q_b}{4\pi\epsilon_0 r_{ab}} \left[ 1 + \frac{\epsilon_{RF} - 1}{2\epsilon_{RF} + 1} \left( \frac{r_{ab}}{r_c} \right)^3 \right] \tag{3.17}$$

where $\epsilon_{RF}$ is the dielectric constant of the surrounding media. Here we use

the value $\epsilon_{RF} = 78.5$ valid for moderately of highly polar liquids, as it is the case for water. In a previous work[129] it has been shown that the use of the RF method yields analogous results than the Ewald sums method (within the simulation statistical uncertainty) for calculating the interfacial tension of these molecular models of water.

In the Ewald sums approach[48], the total electrostatic energy of a system of $N$ point charges $q_a$ placed at positions $r_a$ can be written as

$$U_{coul} = \frac{1}{2V}\sum_{k\neq 0}\frac{4\pi}{k^2}|\rho(k)|^2 exp\left(-\frac{k^2}{4\alpha}\right) - \left(\frac{\alpha}{\pi}\right)^{\frac{1}{2}}\sum_{a=1}^{N} q_a^2 + \frac{1}{2}\sum_{a\neq b}^{N}\frac{q_a q_b\left(\sqrt{\alpha}r_{ab}\right)}{r_{ab}} \quad (3.18)$$

$$U_{coul} = \frac{1}{2V}\sum_{k\neq 0}\frac{4\pi}{k^2}|\rho(k)|^2 exp\left(-\frac{k^2}{4\alpha}\right) - \left(\frac{\alpha}{\pi}\right)^{\frac{1}{2}}\sum_{a=1}^{N} q_a^2 + \frac{1}{2}\sum_{a\neq b}^{N}\frac{q_a q_b\left(\sqrt{\alpha}r_{ab}\right)}{r_{ab}} \quad (3.19)$$

where

$$\rho(k) = \sum_{a=1}^{N} q_a exp(ikr_a) \quad (3.20)$$

$V$ is the volume of the unit cell, given by $L_x \times L_y \times L_z$, $\alpha$ is the Ewald screening parameter, and $\mathbf{k}$ is a reciprocal lattice vector given by $(2\pi n_x/L_x,\ 2\pi n_y/L_y,\ 2\pi n_z/L_z)$, with $n_x$, $n_y$, $n_z$ integers. In the calculations, $\alpha$ and the number of $\mathbf{n}$ and $\mathbf{k}$ vectors are adjustable parameters, and their values are typically selected to achieve the optimum computational efficiency.

Average density profiles were calculated during the simulations and fitted

to a hyperbolic tangent function as

$$\rho(z) = \frac{\rho_l - \rho_v}{2} - \frac{\rho_l - \rho_v}{2} tanh\left(\frac{z - z_0}{d}\right) \tag{3.21}$$

where $\rho_l$, $\rho_v$, $z_0$, and $d$ are the liquid and vapour coexistence densities, the position of the Gibbs-dividing surface, and the width of the interface, respectively. The liquid and vapour densities were determined using the average density profile at each temperature and $d$ was obtained from the hyperbolic tangent function. The "10-90" thickness value of the interface, $t$, is related to $d$ by $t = 2.1972d$.

The surface tension of the simulated planar interface was computed using the mechanical and thermodynamic routes. In the first case, the interfacial tension is calculated from the diagonal components of the pressure tensor,

$$\gamma = \frac{L_z}{2}\left[\langle P_{zz}\rangle - \frac{\langle P_{xx}\rangle + \langle P_{yy}\rangle}{2}\right] \tag{3.22}$$

where $L_z$ is the length of the simulation box along the $z$-axis, perpendicular to the interface, and $P_{\alpha\alpha}$, with $\alpha = x, y, z$, are the diagonal components of the pressure tensor, which in this case were determined following the perturbative method proposed by de Miguel and Jackson[66].

In the second case, namely, the thermodynamic route, the Test-Area (TA) technique proposed by Gloor *et al.*[63], was used to determine the interfacial tension during the simulation performing virtual changes of the interfacial area

of the simulation cell. Following the original work, the surface tension can be calculated as,

$$\gamma = \lim_{\Delta\mathcal{A}\to 0}\left(\frac{\Delta A_{0\to 1}}{\Delta\mathcal{A}}\right)_{N,V,T} = -\frac{k_B T}{\Delta\mathcal{A}} ln\left\langle exp\left(\frac{-\Delta U}{\kappa_B T}\right)\right\rangle_0 \tag{3.23}$$

where $k_B$ is the Boltzmann constant, $\Delta\mathcal{A}$ represents a small change in the interfacial area keeping the volume constant, and $\Delta U$ is the change in configurational energy associated to this perturbation. The TA method has become very popular due to its versatility and it has been applied by different authors to determine the vapour-liquid interfacial properties of LJ chains[68], several water models[1], the Mie potential[73,74], binary fluid mixtures[34,70], and recently it has been used to determine the solid-fluid interfacial tension of a confined LJ fluid[139].

Nevertheless, the results of these calculations are in any case greatly dependent of the type of LRCs used for each term of the intermolecular potential, and this also concerns the LJ dispersive interactions. Assuming the equivalence of the RF and Ewald sums methodologies to account for the long-range coulombic interactions, as previously demonstrated[129] for this particular simulation setup, the objective now is to determine the effect of the LRCs, due to the dispersive interactions, on the interfacial properties. Here we are particularly interested on the comparison of two approaches. In the first case, the LJ contribution to the intermolecular interactions was computed with a

spherical cut-off distance with no further correction. An estimate of the tail correction to the surface tension due to the truncation of the LJ interaction may be calculated *a posteriori*. Once the simulation has finished, the hyperbolic tangent approximation given by Eq. 3.21 can be used to fit the density profile obtained from simulation and calculate the tail correction as,

$$\gamma_{tail} = 12\pi\epsilon\sigma^6(\rho_l - \rho_v)^2 \int_0^1 ds \int_{r_c}^{\infty} dr \coth\left(\frac{rs}{d}\right)\left(\frac{3s^3 - s}{r^3}\right) \tag{3.24}$$

The two-dimensional integral can be solved numerically in a 2D grid of points covering the range indicated by the limits of the integral. A sensitivity analysis has been performed in order to determine the trend of the integral value depending of the step of the grid in each direction. The final value has been found to be convergent beyond a certain step value.

In the second case, we used a proper LRC evaluation method to account for the neglected part of the intermolecular potential energy using the technique proposed by Janeček and improved by MacDowell and Blas as described in Section II.

## 3.5 Results

We first consider the simple molecular model of methane. In particular, we focus our attention on the influence of the cut-off distance and the treatment of the LRCs, due to the dispersive interactions, on the determination of the

phase coexisting densities and interfacial properties. The vapour-liquid surface tension has been evaluated using two different routes, the TA method and the mechanical route.

As can be seen in Table 3.2, the effect of the cut-off distance on the vapour-liquid coexistence densities is very important, particularly in the case of the vapour density. The density value obtained using a cut-off distance of $r_c = 2.5\sigma$ is 70% larger than the corresponding values obtained using LRCs. The trend of the coexistence density values with the increasing cut-off distance can be seen clearly in Table 3.2, showing that results obtained without LRCs are only consistent for cut-off distances equal or larger than $5\sigma$. On the other hand, a cut-off distance of only $r_c = 3\sigma$ is enough to obtain the same results if a proper treatment of the LRCs is considered. This tendency is also represented in Figs. 3.1a and 3.1b for coexistence density and interfacial tension, respectively. This result represents, besides the guarantee to obtain a reliable and exact property value for the molecular model explored, a considerable saving in CPU time in calculations that, as already said, are highly time demanding. It is worth mentioning that the differences between the experimental value and predictions from simulation are larger when LRCs are used. This must be taken into account since an incomplete account of the LRCs may produce misleading conclusions about the quantitative performance of a given molecular model parametrization. In this particular case, the fact that most forcefields are tuned to reproduce the dense fluid phases

behaviour is also to be born in mind, especially for the dense liquid phase for which the LRC corrected value is slightly better.

Table 3.2: Simulation data of coexisting densities ($\rho_l$ and $\rho_v$, both in kg m$^{-3}$) for the Lennard-Jones methane model at 120 K and different cut-off radius values.

| | NO-LRC | | Janeček-LRC | |
|---|---|---|---|---|
| $r_c/\sigma$ | $\rho_l$ | $\rho_v$ | $\rho_l$ | $\rho_v$ |
| 2.5 | 390.7(4) | 5.58(7) | 405.6(4) | 3.15(5) |
| 3 | 399.3(4) | 4.36(5) | 407.5(7) | 3.05(6) |
| 4 | 402.3(3) | 3.70(5) | 407.9(7) | 3.05(8) |
| 5 | 406.2(7) | 3.29(7) | 407.5(7) | 3.08(4) |
| 8 | 406.4(6) | 3.25(6) | 407.6(8) | 3.07(5) |
| *Exp.*[140] | 410.01 | 3.24 | 410.01 | 3.24 |

Similar results are obtained for the vapour-liquid surface tension of methane. As can be seen in Table 3.3 and Fig. 3.1b, the effect of using a cut-off distance (without LRCs) is negligible when its value is larger than $5\sigma$. However, to obtain the same cut-off independent predictions, only a cut-off distance of $r_c = 3\sigma$ is necessary if LRCs are used. Differences between the results obtained with LRC and without them (using $r_c = 2.5\sigma$) are around 30% approximately. Note also that predictions from simulations for the surface tension using the TA and mechanical routes produce compatible numerical values, as expected. Finally, two interesting features can be mentioned here. Firstly, the tail correction for interfacial tension determined through the integral in Eq. 3.24 has also been calculated and presented in the column denoted as tail-LRC in Ta-

ble 3.3. The results show that this term value depends on the cut-off distance used during the simulation, and leads to a final interfacial tension value that does not show monotonic convergence with increasing cut-off distance, contrarily to what happened in the other cases, indicating clearly a limited reliability of this methodology when accounting for the LRCs. Secondly, the interfacial tension value obtained without LRCs is closer to the experimental value than that corresponding to the LRC value. As in the case of coexistence densities, the ability of a given model for predicting quantitatively the surface tension must be evaluated with care, through a complete calculation that takes into account LRCs in order to obtain the "real" model value for the point considered. Note that the interfacial tension containing the complete LRC treatment is around 7% higher than the non-corrected value, which is significative from a quantitative point of view. It is also important to remark that this value overestimates the experimental value.

Once the influence of the LRCs, due to the dispersive interactions, on the phase behaviour and interfacial properties for a model consisting of a single LJ site (methane) has been evaluated, we consider now the case of a molecular model that also includes coulombic interactions such as water. Table 3.4 shows the coexisting densities as obtained from Monte Carlo simulations at a single temperature, 400 K, for the TIP4P/2005 model[106]. We have used different methods for calculating both the dispersive interactions associated to the LJ potential and the coulombic interactions due to the presence of point charges

Table 3.3: Simulation data of surface tension ($\gamma$ in mJ m$^{-2}$) for the Lennard-Jones methane model at 120 K and different cut-off radius values. Subscripts *ta* and *mr* stand for Test-Area and mechanical route, respectively.

| | NO-LRC | | tail-LRC | | Janeček-LRC | |
|---|---|---|---|---|---|---|
| $r_c/\sigma$ | $\gamma_{ta}$ | $\gamma_{mr}$ | $\gamma_{ta}$ | $\gamma_{mr}$ | $\gamma_{ta}$ | $\gamma_{mr}$ |
| 2.5 | 8.67(7) | 8.67(7) | 12.66(7) | 12.66(7) | 13.61(7) | 13.64(7) |
| 3 | 10.41(7) | 10.41(7) | 13.55(7) | 13.55(7) | 13.9(1) | 13.8(1) |
| 4 | 11.75(9) | 11.75(9) | 13.66(9) | 13.66(9) | 13.8(1) | 13.8(1) |
| 5 | 12.74(9) | 12.73(9) | 14.03(9) | 14.02(9) | 13.8(1) | 13.8(1) |
| 8 | 12.7(1) | 12.7(1) | 13.4(1) | 13.4(1) | 13.7(1) | 13.8(1) |
| *Exp.*[141] | | | 11.3 | | | |

in the molecular model. In particular, we neglect the LRCs associated to the dispersive interactions and calculate explicitly the LRCs using the Janeček's methodology. In addition to that, we have also computed the coulombic interactions using two different procedures, the Ewald sums and the RF method. The effect of the LRCs on the coexisting density values is hardly noticeable. As in the case of methane, the use of LRCs allows to choose shorter values of $r_c$. The differences between both results are not relevant, as can be seen clearly in Fig. 3.2a. However, this is no longer true for the case of the interfacial tension, as it is shown in Table 3.5 and Fig. 3.2b. The value of the surface tension obtained using the LRCs is approximately 7% higher than that obtained when LRCs are disregarded, obtaining a better agreement between simulation predictions and experimental data taken from literature. It is obvious from these results that the surface tension is much more sensitive to LRCs

than the coexisting densities. As in the case of methane, the use of LRCs *a posteriori* (tail-LRC) yields a somewhat erratic trend.

Table 3.4: Simulation data of coexisting densities ($\rho_l$ and $\rho_v$, both in kg m$^{-3}$) for the TIP4P/2005 water model at 400 K and different cut-off radius values.

| | NO-LRC | | Janeček-LRC | | | |
|---|---|---|---|---|---|---|
| $r_c/\sigma$ | $\rho_l$ | $\rho_v$ | $\rho_l^{RF}$ | $\rho_v^{RF}$ | $\rho_l^{EW}$ | $\rho_v^{EW}$ |
| 1.5 | | | 948(3) | 0.53(4) | | |
| 2 | | | 946(2) | 0.70(3) | 947(2) | 0.66(4) |
| 2.5 | 924(2) | 0.65(3) | 935(2) | 0.56(2) | 935(2) | 0.59(3) |
| 3 | 926(2) | 0.56(4) | 929(1) | 0.57(4) | 928(2) | 0.57(4) |
| 4 | 929(2) | 0.60(2) | 929(1) | 0.58(3) | 928(2) | 0.57(4) |
| 5 | 929(1) | 0.60(3) | 929(2) | 0.58(3) | 928(2) | 0.57(5) |
| *Exp.*[142] | 937.5 | 1.37 | 937.5 | 1.37 | 937.5 | 1.37 |

Table 3.5: Simulation data of surface tension ($\gamma$ in mJ m$^{-2}$) for the TIP4P/2005 water model at 400 K and different cut-off radius values. Subscripts *ta* and *mr* stand for Test-Area and mechanical route, respectively.

| | NO-LRC | | tail-LRC | | Janeček-LRC | | | |
|---|---|---|---|---|---|---|---|---|
| $r_c/\sigma$ | $\gamma_{ta}$ | $\gamma_{mr}$ | $\gamma_{ta}$ | $\gamma_{mr}$ | $\gamma_{ta}^{RF}$ | $\gamma_{mr}^{RF}$ | $\gamma_{ta}^{EW}$ | $\gamma_{mr}^{EW}$ |
| 1.5 | | | | | 65(1) | 64(2) | | |
| 2 | | | | | 60(2) | 60(1) | 58(1) | 57.2(9) |
| 2.5 | 43(1) | 42(1) | 51(1) | 50(1) | 52.3(9) | 53(1) | 53.7(7) | 54(1) |
| 3 | 47.4(7) | 47.9(7) | 53.3(7) | 53.8(7) | 52(1) | 51.8(8) | 52(1) | 52(1) |
| 4 | 48.7(8) | 48.6(8) | 52.3(8) | 52.1(8) | 52.1(9) | 52.3(9) | 52(1) | 52.2(8) |
| 5 | 48.4(7) | 48.4(9) | 50.9(7) | 50.9(9) | 52.5(8) | 52(1) | 52(1) | 52.2(8) |
| *Exp.*[143] | 53.6 | | | | | | | |

Before finishing the analysis of the effect of the LRCs on the properties of water, it is important to mention that the values obtained for both, coexisting

densities and surface tension values, are identical using Ewald sums and RF methods for determining the coulombic interactions of the system. Also, as in the case of methane, the surface tension values obtained using the TA methodology and the mechanical route are identical to within the statistical errors of the simulation results. Taking into account this information, and unless otherwise stated, the rest of the interfacial tension data reported in this work were obtained using TA technique and RF method. In addition to that, we have used the cut-off distance value of $r_c = 3\sigma$ for calculating the LRCs under the Janeček's approximation.

We have also determined the vapour-liquid coexisting densities and the surface tension of different models of water, including TIP4P/2005, TITP4P/Ew, and the original TIP4P, at several temperatures, from 350 up to 500 K. Results obtained in this work are presented in Table 3.6. The experimental data values recommended by the NIST, the Setzmann and Wagner[140] dedicated EoS for the case of coexistence densities and Somayajulu[141] EoS for interfacial tension, are also listed in this table. As can be seen, the TIP4P/2005 model provides the best description of these properties, as previously established[1].

Finally, we have analysed the effect of the LRCs, due to the dispersive interactions, on the phase behaviour and interfacial properties of carbon dioxide. In particular, we consider here several models of $CO_2$ that describe this molecule as a linear rigid trimer with three LJ sites and three point charges that mimic the existence of a strong quadropole moment value. Table 3.7

Table 3.6: Simulation data of coexisting densities ($\rho_l$ and $\rho_v$, both in kg m$^{-3}$) and surface tension ($\gamma$/ mJ m$^{-2}$), for the different water molecular models tested. The reaction field method was used in the simulations to handle electrostatic interactions, and a constant LJ cut-off radius $r_c = 3\sigma$ was used. These values are compared with experimental values

| $T/K$ | $\rho_l^{LRC}$ | $\rho_l^{NIST}$ | $\rho_v^{LRC}$ | $\rho_v^{NIST}$ | $\gamma_{ta}^{LRC}$ | $\gamma^{NIST}$ |
|---|---|---|---|---|---|---|
| | | | TIP4P/2005 | | | |
| 350 | 968(1) | 973.7 | 0.09(2) | 0.26 | 60.9(9) | 63.2 |
| 400 | 929(2) | 937.5 | 0.58(3) | 1.37 | 52(1) | 53.6 |
| 450 | 882(2) | 890.3 | 2.3(2) | 4.8 | 41(1) | 42.9 |
| 500 | 820(2) | 831.3 | 7.4(3) | 13.2 | 30(2) | 31.5 |
| | | | TIP4P/Ew | | | |
| 350 | 963(3) | 973.7 | 0.11(2) | 0.26 | 56(2) | 63.2 |
| 400 | 922(2) | 937.5 | 0.9(1) | 1.37 | 45.9(7) | 53.6 |
| 450 | 869(2) | 890.3 | 3.2(2) | 4.8 | 35.8(9) | 42.9 |
| 500 | 799(2) | 831.3 | 10.1(3) | 13.2 | 27(1) | 31.5 |
| | | | TIP4P | | | |
| 350 | 953(2) | 973.7 | 0.32(3) | 0.26 | 48(1) | 63.2 |
| 400 | 896(2) | 937.5 | 1.9(1) | 1.37 | 37.5(9) | 53.6 |
| 450 | 827(2) | 890.3 | 7.3(2) | 4.8 | 27.5(8) | 42.9 |
| 500 | 732(2) | 831.3 | 26(1) | 13.2 | 16(1) | 31.5 |

presents the results obtained for the vapour-liquid coexisting densities, and Table 3.8 those corresponding to the vapour-liquid interfacial tension. In both cases, the range of temperatures studied goes from 230 up to 270 K. The effect of the LRCs, due to the dispersive interactions, accounted for using the Janeček's methodology is clearly noticeable for the case of vapour-liquid coexisting densities. This can be clearly seen in Fig. 6.3a for the case of the Zhang-Duan model, a fact that is not surprising if we take into account that

each molecule contains now three LJ sites. Agreement between predictions from the model and experimental data taken from the literature is better when using the Janeček's inhomogeneous LRCs than with the use of a constant cut-off for the LJ potential and no further corrections. Notice that the last choice produces considerable deviations between simulation and experiment, especially as the temperature is raised. The effect of LRCs, due to the dispersive interactions, on the interfacial tension data is similar to that exhibited in the case of methane, as can be seen in Fig. 6.3b. The interfacial tension values obtained from simulation when using the inhomogeneous LRCs are 5% higher than those corresponding to the case in which a constant value of the cut-off distance is used. As a result, the simulations that use a constant cut-off distance for the intermolecular potential overestimates the experimental data in the whole range of temperatures considered.

## 3.6 Conclusions

We have studied the effect of LRCs, due to the dispersive interactions, on the vapour-liquid surface tension of several molecular models of real substances. The results shown in this work lead to the following conclusions. First, the pure truncation of the dispersive (LJ) term of the intermolecular potential produces an undesirable underestimation of the computed interfacial tension along byphasic inhomogeneous Monte Carlo simulations. This

Table 3.7: Simulation data of coexisting densities ($\rho_l$ and $\rho_v$, both in kg m$^{-3}$) for the different $CO_2$ molecular models tested. The reaction field method was used in the simulations to handle electrostatic interactions, and a constant LJ cut-off radius $r_c = 3\sigma$ was used. These values are compared with NIST recommended values (Span and Wagner[144])

| $T/K$ | $\rho_l^{NO-LRC}$ | $\rho_l^{LRC}$ | $\rho_l^{NIST}$ | $\rho_v^{NO-LRC}$ | $\rho_v^{LRC}$ | $\rho_v^{NIST}$ |
|---|---|---|---|---|---|---|
| | | | MSM | | | |
| 230 | 1110(1) | 1121(1) | 1129 | 28.4(4) | 24.2(3) | 23.3 |
| 240 | 1071(2) | 1083(1) | 1089 | 38.5(3) | 35.8(4) | 33.3 |
| 250 | 1029(1) | 1042(2) | 1046 | 55.4(2) | 49.8(5) | 46.6 |
| 260 | 982(2) | 995(2) | 999 | 73.0(6) | 67.6(5) | 64.4 |
| 270 | 927(1) | 943(2) | 946 | 100.4(7) | 90.2(7) | 88.4 |
| | | | EPM2 | | | |
| 230 | 1113(2) | 1123(3) | 1129 | 27.5(2) | 24.9(2) | 23.3 |
| 240 | 1075(2) | 1084(2) | 1089 | 38.5(5) | 34.6(4) | 33.3 |
| 250 | 1027(2) | 1040(2) | 1046 | 54.1(4) | 48.0(6) | 46.6 |
| 260 | 978(1) | 994(2) | 999 | 76.3(5) | 69.1(3) | 64.4 |
| 270 | 922(1) | 940(1) | 946 | 103.9(7) | 93.6(5) | 88.4 |
| | | | TraPPE | | | |
| 230 | 1117(2) | 1124(2) | 1129 | 23.1(2) | 20.4(3) | 23.3 |
| 240 | 1080(3) | 1083(2) | 1089 | 33.1(4) | 31.4(2) | 33.3 |
| 250 | 1037(1) | 1049(2) | 1046 | 46.2(5) | 42.6(3) | 46.6 |
| 260 | 990(2) | 1002(2) | 999 | 64.4(5) | 56.9(7) | 64.4 |
| 270 | 936(1) | 954(2) | 946 | 89.2(6) | 78.2(5) | 88.4 |
| | | | Zhang-Duan | | | |
| 230 | 1118(2) | 1126(1) | 1129 | 28.9(3) | 25.9(3) | 23.3 |
| 240 | 1078(2) | 1088(2) | 1089 | 40.5(4) | 36.5(2) | 33.3 |
| 250 | 1031(1) | 1045(2) | 1046 | 57.8(5) | 51.2(7) | 46.6 |
| 260 | 981(1) | 998(1) | 999 | 79.6(5) | 70.8(4) | 64.4 |
| 270 | 927(1) | 944(1) | 946 | 105.1(9) | 93.3(4) | 88.4 |

Table 3.8: Simulation data of surface tension ($\gamma$/ mJ m$^{-2}$), for the different $CO_2$ molecular models tested.

| $T/K$ | $\gamma_{ta}^{NO-LRC}$ | $\gamma_{ta}^{LRC}$ | $\gamma_{ta}^{NO-LRC}$ | $\gamma_{ta}^{LRC}$ | $\gamma^{NIST}$ [145] |
|---|---|---|---|---|---|
| | $MSM$ | | $EPM2$ | | |
| 230 | 14.0(3) | 14.6(2) | 13.9(3) | 14.2(3) | 13.9 |
| 240 | 11.7(2) | 12.1(3) | 11.7(2) | 12.0(2) | 11.5 |
| 250 | 9.0(2) | 9.9(2) | 9.2(2) | 9.6(3) | 9.3 |
| 260 | 7.1(2) | 7.4(3) | 6.9(1) | 7.4(2) | 7.1 |
| 270 | 5.0(1) | 5.3(2) | 4.8(2) | 5.1(2) | 5.1 |
| | $TraPPE$ | | $Zhang-Duan$ | | |
| 230 | 15.0(3) | 15.9(2) | 13.6(2) | 14.3(3) | 13.9 |
| 240 | 12.9(3) | 12.4(2) | 11.5(2) | 11.9(2) | 11.5 |
| 250 | 10.7(2) | 11.1(2) | 9.2(3) | 9.7(2) | 9.3 |
| 260 | 8.1(2) | 8.4(2) | 7.0(2) | 7.2(2) | 7.1 |
| 270 | 5.7(2) | 6.1(1) | 4.8(2) | 5.1(1) | 5.1 |

effect has been checked for models where the LJ term represents the complete intermolecular potential contribution, as it is the case for the typical united-atom methane forcefield, but also for models including point electric charges in their molecular structures, as it is the case of TIP4P-type models for water or MSM-type models for carbon dioxide. In every case, the complete account of LRCs using the Janeček's methodology, with the improved formulation of MacDowell and Blas, leads to an augmentation around 5-7% on the values of the interfacial tension for the pure fluids investigated. Additionally, this methodology allows a faster convergence on the determined interfacial tension and coexistence densities from cut-off distance values as short as $3\sigma$. Moreover,

this method is superior to post processing methods as the determination of the integered contribution to the interfacial properties due to potential truncation. The variation on the properties produced by dispersive LRCs treatment must be taken into account for quantitative purposes when comparing the respective performances of different models parametrizations. In addition, the use of this methodology circumvents the otherwise necessary heuristic and non rigorous choice of the cut-off distance, which plays an important role also beyond the pure numerical results, because it also imposes the use of large simulation boxes. This latter condition, added to the inherent slowness of this type of byphasic simulations and combined with the fact that simulation times increase very fast with the cut-off distance, allows to conclude that the use of the dispersive potential tail correction as proposed in this work optimizes the formal reliability, numerical performance, and CPU time requirement of the calculation of interfacial properties.

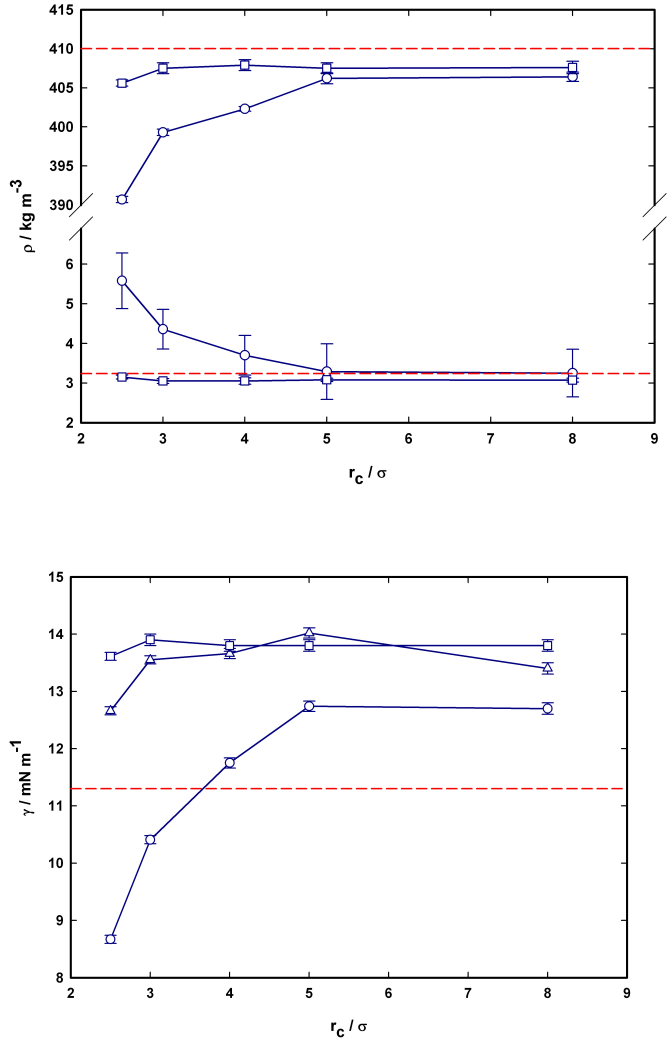


Figure 3.1: (a) Evolution with the cut-off radius value of the computed coexisting densities (liquid phase above, gas phase below) for LJ methane at 120 K. Circles: calculation without LRCs. Squares: calculation with Janeček's LRCs. In both cases the dashed line represents the NIST recommended experimental value. (b) id for computed interfacial tension, computed using the TA method. In this case triangles represent the values obtained applying the LRCs represented by Eq. 3.24

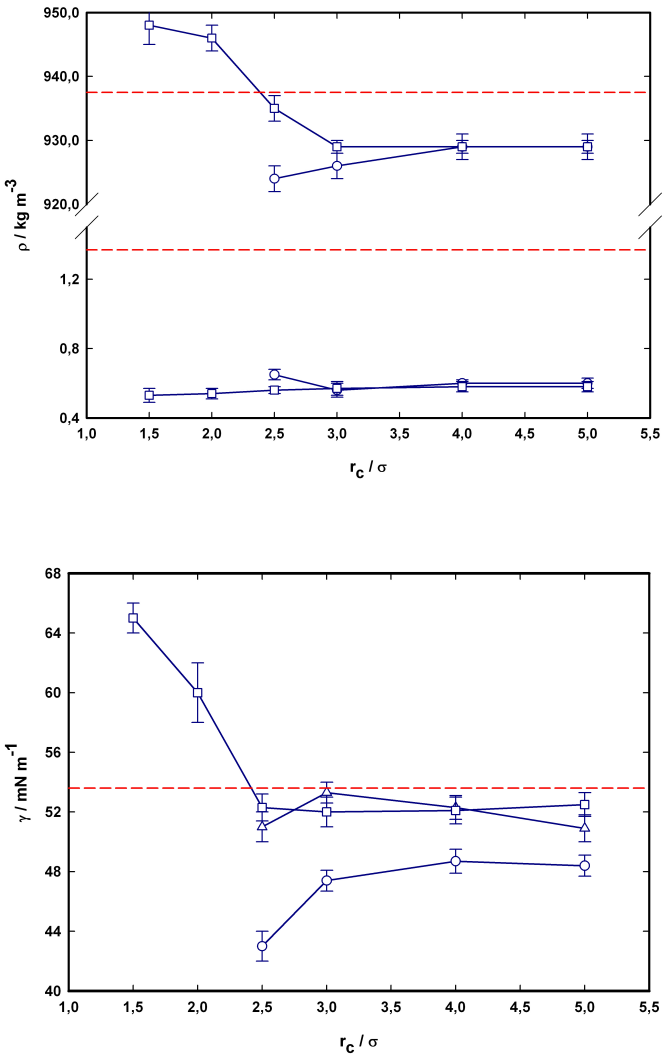


Figure 3.2: Same caption as Fig. 6.1, for TIP4P/2005 water molecular model, at 400 K. For the points represented, the RF method was used to handle electrostatic interactions.

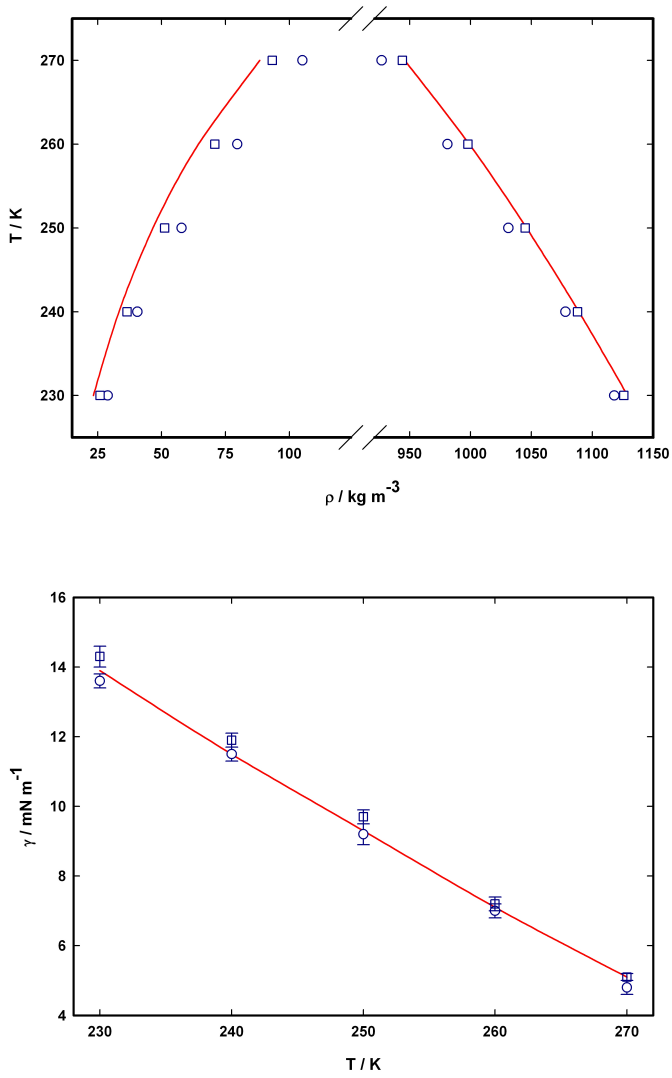


Figure 3.3: (a) Coexistence densities for $CO_2$. Solid line: NIST experimental correlation, symbols: results obtained with the Zhang-Duan molecular model (circles: calculation without LRCs and $r_c = 5\sigma$, squares: calculation with Janeček's LRCs). (b) same caption for interfacial tension, calculated in every case using the TA method.

Chapter 4

# On interfacial tension calculation from the Test-Area methodology in the grand canonical ensemble

## 4.1 Abstract

We propose the extension of the Test-Area methodology, originally proposed to evaluate the surface tension of planar fluid-fluid interfaces along a computer simulation in the canonical ensemble, to deal with the solid-fluid interfacial tension of systems adsorbed on slitlike pores using the grand canonical ensemble. In order to check the adequacy of the proposed extension, we apply the method for determining the density profiles and interfacial tension of spherical molecules adsorbed in slitlike pore with different pore sizes and solid-fluid dispersive energy parameters along the same simulation. We also calculate the solid-fluid interfacial tension using the original Test-Area method in the canonical ensemble. Agreement between the results obtained from both methods indicate that both methods are fully equivalent. The advantage of the new methodology is that allows to calculate simultaneously the density profiles and the amount of molecules adsorbed onto a slitlike pore, as well as the solidfluid interfacial tension. This ensures that the chemical potential at which all properties are evaluated during the simulation is exactly the same since simulations can be performed in the grand canonical ensemble, mimicking the conditions at which the adsorption experiments are most usually carried out in the laboratory.

## 4.2 Introduction

During the last two decades there has been an enormous advance in the fundamental knowledge of interfacial properties of inhomogeneous complex fluids, not only in the cases of vapour-liquid and liquid-liquid free interfaces, but also in other inhomogeneous situations, such as molecules near planar walls, inside slit-like pores, and in general, in all situations concerning fluids adsorbed on structured materials as zeolites, nanotubes, and amorphous adsorbents. Molecular chains, substances with specific interactions as hydrogen bonding, and systems interacting through long-range intermolecular forces including Coulombic-type interactions, are only a few examples of systems for which new methods of Statistical Mechanics and computer simulation techniques are now available to describe their thermodynamic and structural behaviour.

One of the main reasons of this advance is undeniably the constant development of molecular-based theories of Statistical Mechanics. Density Gradient Theory (DGT)[70,73,131,146–149], and more significantly, Density Functional Theory (DFT)[150,151], have allowed to determine thermodynamic and structural properties of spherical and molecular inhomogeneous systems. Particularly relevant to this discussion are the great amount of works published for predicting and understanding the behaviour of fluids at free interfaces and adsorbed on different materials. The new generation of functional theories, such as those

based on Fundamental Measure Theory (FMT)[152–154] and their different versions, have provided an important insight in the field. We recommend the work of Llovell *et al.*[155] for a recent review of the literature.

As in the case of molecular-based theories, computer simulation methods have also experienced a great development in the field of interfacial properties, particularly in new techniques for the calculation of fluid-fluid interfacial tension. The traditional method used for determining this key property has been (and still is) the mechanical route, through the evaluation of the microscopic components of the pressure tensor from the virial. However, during the last decade there has been an intense and fruitful development of new methodologies based on the thermodynamic definition of surface tension. The use of new theoretical approaches, such as the Expanded Ensemble (EE)[65], Wandering Interface Method (WIM)[64], or perturbative methods as the Test-Area (TA)[63] technique, or the determination of the macroscopic components of the pressure tensor (using for instance virtual volume changes, as proposed by de Miguel and Jackson[156] or Brumby *et al.*[157]), are only a few examples of the new methods available in literature from a computer simulation perspective. These methods are becoming very popular, and as an example the TA method has been so far used by several authors to determine vapour-liquid interfacial properties of Lennard-Jones (LJ) chains[68], several water models[1,129], the Mie potential[73,74], or binary fluid mixtures[70,158].

The traditional method, and also most of the recent ones, have been ap-

plied for determining the fluid-fluid (mainly vapour-liquid) surface tension of simple and complex systems using molecular simulations carried out in the canonical ensemble, i.e., simulations in which the number of particles, volume, and temperature are kept constant. Obviously, this is the "natural" ensemble for calculating the fluid-fluid interfacial properties at direct coexistence using computer simulation. However, this is not the case if we are dealing with confined inhomogenous systems. There are only a few studies in which the solid-fluid interfacial tension of a confined fluid is calculated from computer simulation (see for instance Hamada *et al.*,[159], Singh and Kwak[160], Das and Binder[161]), while most authors concentrate on phase behaviour (Gelb *et al.*[162]), adsorption (del Pino *et al.*[163]) or fluid structure (Evans[164]). The reason for this is that confined fluid interfacial tension is not experimentally accessible. However, its determination is important from a formal point of view because this magnitude is easily calculated theoretically from Density Functional Theory. A comparison between theoretical and molecular simulation predictions constitutes a strong test to check the ability of a theory in predicting the behaviour of adsorbed molecules in a pore.

How is it possible to determine the interfacial tension of a fluid confined into a pore from computer simulation? There are different possibilities for calculating the interfacial tension of a confined system using methodologies based on its thermodynamic definition, and particularly, using the TA[63] technique. However, if we are interested in determining all the involved interfacial proper-

ties, including the interfacial tension, at the same thermodynamic conditions at which the fluid adsorbed inside a pore is in equilibrium with its reservoir, the practical possibilities are limited. This situation depicted is the one occurring in most laboratory adsorption experiments, so the possibility to reproduce the same conditions determines the potential quantitative evaluation of the molecular simulation estimations. The goal in adsorption experiments is to determine the amount of molecules adsorbed as a function of the temperature and pressure of the reservoir with which the system is in contact. Since in the experimental setup the adsorbed gas is in equilibrium with the gas in the reservoir, the equilibrium conditions are that the temperature and chemical potential of the gas inside and outside the adsorbent must be identical. These conditions are exactly mimicked in the grand canonical ensemble, and hence, in a grand canonical Monte Carlo (GCMC) computer simulation.

From a computer simulation perspective, the calculation of the amount of molecules adsorbed in a pore, at a given pressure and temperature, involves a two-step procedure. In the first step, a bulk simulation is performed in the isothermal-isobaric or NPT ensemble at a given P and T. In order to evaluate the chemical potential of the system at the thermodynamic conditions, the particle insertion method proposed by Widom[165] is used during the production stage of the simulation. Since the density of the reservoir is usually low since the bulk phase is a gas, the Widom methodology is usually appropriate. It is important to recall here that this chemical potential $\mu$ is the corresponding

value for the reservoir at the selected pressure and temperature. The second step involves a grand canonical ensemble simulation, at the same temperature and chemical potential, that allows to determine all the thermodynamic and structural properties of the adsorbed gas, including the average amount adsorbed, the density profiles, or even the isostheric heat of adsorption. However, since the TA methodology is only applicable for simulations carried out in the canonical or NVT ensemble, there is no possibility of determining the interfacial tension during the same simulation run. The standard procedure involves a third independent simulation, in the NVT ensemble, of the confined fluid at a density equal to the average amount of adsorbed molecules obtained in the GCMC simulation. During the production stage it is then possible to calculate the solid-fluid interfacial tension of the adsorbed system in the pore by performing virtual displacements in the interfacial areas, as proposed by Gloor *et al.*[63] in the TA procedure. Note that it is also possible to calculate the interfacial tension from the thermodynamic route through the relationship that connects the interfacial tension and the normal and tangential components of the pressure tensor. Consider a system confined inside a pore with a well defined geometry, such as a slit-like pore in which the system is confined between two parallel walls that interact with the fluid through a known solid-fluid intermolecular potential. The z-axis is choosen perpendicular to the walls of the pore and the x- and y-axis are parallel to the walls. It is important to recall here that in a inhomogeneous system the pressure is not a scalar but a

tensorial magnitude. In the particular case of pores with planar geometry in which the inhomogeneity of the system is along the direction perpendicular to the walls, i.e. the z-axis, the microscopic perpendicular or normal (along the z-axis direction) component of the pressure tensor, $P_{zz} \equiv P_N$, is constant and equal to the "true" thermodynamic pressure inside the pore. The microscopic tangential components of the pressure tensor, parallel to the walls, $P_{xx}(z) = P_{yy}(z) \equiv P_T(z)$, are functions of the z coordinate, or distance to the walls, and it is different to $P_N$, i.e., $P_T(z) \neq P_N$.

An alternative, more efficient, and faster procedure, without the need of performing the third computer simulation (the NVT run) would be feasible if the solid-fluid interfacial tension were calculated at the same time than the rest of thermodynamic and structural properties during the GCMC simulation. This would be possible by extending the TA methodology to be applicable in the grand canonical ensemble. The goal of this work is to extend the method proposed by Gloor *et al.*[63] to the grand canonical ensemble. We have ten performed some Monte Carlo simulations in both ensembles to check the equivalence of the predictions obtained using the two methodologies. We have also determined interfacial tension using Monte Carlo simulations in the $\mu VT$ ensemble by the more traditional method of Irving and Kirkwood[67], that entails the calculation of the components of the pressure tensor using the virial route.

The rest of the paper is structured as follows. In section III we derivate

the extension of the formalism in the grand canonical ensemble. The next section presents the comparison between the interfacial tension calculations using $\mu$VT and NVT ensembles for a benchmark system. Finally, we present the main conclusions of this work.

## 4.3 Test-Area methodology in the GCMC ensemble

Consider an open system of particles at a given temperature T, occupying a volume V, and at chemical potential $\mu$. In the grand canonical or $\mu$VT ensemble, the key free energy is the grand canonical potential energy $\Omega = \Omega(\mu, V, T) \equiv \Omega_{\mu VT}$. The change in grand canonical free energy when the temperature, volume, and chemical potencial are changed with their corresponding infinitesimal amounts is given by the well-known change of free energy in the grand canonical ensemble. However, density variations produce an extra contribution to the thermodynamic state functions, in general, and to the grand canonical free energy in particular. In the presence of an interface the free energies and particularly $\Omega$ need to be modified to include the work that has to be imposed by external forces in order to change the interfacial area $\mathcal{A}$ by $d\mathcal{A}$,

$$d\Omega(\mathcal{A}) = -SdT - PdV - Nd\mu + \gamma d\mathcal{A} \tag{4.1}$$

The contribution $\gamma d\mathcal{A}$ is the work needed and the coefficient $\gamma$ is the interfacial tension of the system. Note that now $\Omega = \Omega(\mu, V, T, \mathcal{A}) \equiv \Omega_{\mu VT}(\mathcal{A})$ is

also a function of the interfacial area $\mathcal{A}$. Its thermodynamic definition follows from the expression,

$$\gamma = \left( \frac{\partial \Omega}{\partial \mathcal{A}} \right)_{\mu VT} \tag{4.2}$$

where the partial derivative must be evaluated at constant chemical potential $\mu$, volume V, and temperature T. Note that in the case of a two-phase vapour-liquid or liquid-liquid interface, the usual definition of the surface tension invokes a similar derivative but in the the canonical or NVT ensemble. This is the "natural" ensemble for studying a two-phase fluid-fluid interface since the number of particles N, volume V, and temperature T are constant.

Similarly to the case of the canonical ensemble, the interfacial tension can be computed efficiently from the previous expression by using fictitious increasing and decreasing surface area. The grand canonical free energy is related with the grand canonical partition function $\Xi_{\mu VT}$ through the well-known Statistical Mechanics relationship,

$$\Omega \equiv \Omega_{\mu VT}\left(\mathcal{A}\right) = -k_B T \ln \Xi_{\mu VT} \tag{4.3}$$

where $k_B$ is Boltzmann's constant, and the grand canonical partition function $\Xi_{\mu VT}$ is expressed as

$$\Xi_{\mu VT} \equiv \Xi_{\mu,V,T}(\mathcal{A}) = \sum_{N=0}^{+\infty} exp\left[\,\beta \mu N\,\right] Q_{NVT} \tag{4.4}$$

where $Q_{NVT}$ is the canonical partition function of a system formed by N particles (at temperature T and volume V) and $\beta = (k_B T)^{-1}$. The partition function of a system of spherical molecules without internal degrees of freedom can be written as

$$Q_{NVT} = \frac{1}{\Lambda^{3N} N!} \int d\mathbf{r}^N exp\left[ -\beta U_N(\mathbf{r}^N) \right] = \frac{1}{\Lambda^{3N} N!} Z_{NVT} \tag{4.5}$$

where $\Lambda$ is the de Broglie wavelength associated to the translational degrees of freedom of the system, $U_N \equiv U_N(\mathbf{r}^N)$, the intermolecular potential energy of a system formed by $N$ particles that depends on all the positions $\mathbf{r}^N \equiv \{\mathbf{r}_1, \ldots, \mathbf{r}_N\}$, and $Z_{NVT}$ is the configurational partition function of the system

$$Z_{NVT} = \int d\mathbf{r}^N exp\left[ -\beta U_N(\mathbf{r}^N) \right] \tag{4.6}$$

Although we have used explicitly the relationship given by Eq. 4.5 valid for systems that interact through spherical intermolecular potentials, with no internal degrees of freedom, the methodology is equally applicable to molecular systems, as it will be explained.

Perturbative methods in computer simulation allow to calculate a number of thermodynamic properties from estimation of the change in the appropriate free energy under fictitious perturbation. The works of Eppenga and Frenkel[166], Harismiadis *et al.*[167], and de Miguel and Jackson[156], in the case of pressure or components of the pressure tensor, and that of Gloor *et al.* in

the case of surface tension are clear examples of this methodology. Following the work of Gloor *et al.*, the interfacial tension can be easily evaluated in the grand canonical ensemble using the appropriate thermodynamics definition. Using Eq. 4.2, the interfacial tension can be expressed as the difference in grand potential free energy between to states with different surface areas,

$$\gamma = \left(\frac{\partial \Omega}{\partial \mathcal{A}}\right)_{\mu VT} = \lim_{\Delta\mathcal{A}\to 0} \frac{\Omega_{\mu VT}\left(\mathcal{A}+\Delta\mathcal{A}\right) - \Omega_{\mu VT}\left(\mathcal{A}\right)}{\Delta\mathcal{A}} \approx \frac{\Delta\Omega_{\mu VT}}{\Delta\mathcal{A}} \tag{4.7}$$

The difference in free energy can be written in terms of the grand canonical partition functions of the system having surface areas $\mathcal{A}' = \mathcal{A} + \Delta\mathcal{A}$ and $\mathcal{A}$, with $\Delta\mathcal{A} > 0$,

$$\Delta\Omega_{\mu VT} = \Omega_{\mu VT}(\mathcal{A}') - \Omega_{\mu VT}(\mathcal{A}) = -k_B T \ln \left[ \frac{\sum_{N=0}^{+\infty} \frac{e^{\beta\mu N}}{\Lambda^{3N} N!} \int d\mathbf{r}^N exp\left[-\beta U(\mathcal{A}')\right]}{\sum_{N=0}^{+\infty} \frac{e^{\beta\mu N}}{\Lambda^{3N} N!} \int d\mathbf{r}^N exp\left[-\beta U(\mathcal{A})\right]} \right] \tag{4.8}$$

where $U(\mathcal{A}) \equiv U_N(\mathbf{r}^N;\mathcal{A})$ and $U(\mathcal{A}') \equiv U_N(\mathbf{r}^N;\mathcal{A}')$ denote the intermolecular potential energy of the system with surface area $\mathcal{A}$ and $\mathcal{A}'$, respectively. It is straightforward to write the previous equation in a more convenient way as

$$\Delta\Omega_{\mu VT} = -k_B T \ln \left[ \frac{\sum_{N=0}^{+\infty} \frac{e^{\beta\mu N}}{\Lambda^{3N} N!} \int d\mathbf{r}^N exp\left(-\beta\Delta U^{+}\right) exp\left[-\beta U(\mathcal{A})\right]}{\sum_{N=0}^{+\infty} \frac{e^{\beta\mu N}}{\Lambda^{3N} N!} \int d\mathbf{r}^N exp\left[-\beta U(\mathcal{A})\right]} \right] \tag{4.9}$$

where $\Delta U^{+} = U(\mathcal{A} + \Delta\mathcal{A}) - U(\mathcal{A})$ is the change in potential energy when the interfacial area changes from $\mathcal{A}$ to $\mathcal{A}+\Delta\mathcal{A}$. According to Eq. 4.9, the difference in grand potential free energy is proportional to the logarithm of the average of the Boltzmann factor associated with the surface area perturbation over the unperturbed system of surface area $\mathcal{A}$. This configurational average can be written as:

$$\Delta\Omega_{\mu VT} = -k_B T \ln \left\langle \, exp \left[ -\beta \Delta U^{+} \right] \right\rangle_{\mu VT} \tag{4.10}$$

The interfacial tension can be then calculated in the grand canonical ensemble through the following expression,

$$\gamma^{+} = -\frac{k_B T}{\Delta\mathcal{A}} \ln \left\langle \, exp \left[ -\beta \Delta U^{+} \right] \right\rangle_{\mu VT} \tag{4.11}$$

In principle, one could also have selected a backward, finite difference scheme to approximate the first derivative of the free energy. In this case one can write:

$$\gamma = \left( \frac{\partial \Omega}{\partial \mathcal{A}} \right)_{\mu VT} = \lim_{\Delta\mathcal{A}\to 0} \frac{\Omega_{\mu VT}\left(\mathcal{A}\right) - \Omega_{\mu VT}\left(\mathcal{A} - |\Delta\mathcal{A}|\right)}{|\Delta\mathcal{A}|} \tag{4.12}$$

which results in an expression for the interfacial tension of the form:

$$\gamma^{-} = -\frac{k_B T}{|\Delta\mathcal{A}|} \ln \left\langle \, exp \left[ -\beta \Delta U^{+} \right] \right\rangle_{\mu VT} \tag{4.13}$$

where $\Delta U^{-} = U(\mathcal{A}) - U(\mathcal{A} - |\Delta\mathcal{A}|)$ is the change in potential energy when the interfacial area changes from $\mathcal{A}$ to $\mathcal{A} - |\Delta\mathcal{A}|$.

For systems of particles interacting through continuous potentials, $\gamma^{+}$ and $\gamma^{-}$ are expected to be equal to the value of the interfacial tension as long as $\Delta\mathcal{A} \to 0$. In practical implementations, small but finite values of $\Delta\mathcal{A}$ must be used, and the forward and backward approaches will not yield exactly the same value. As in previous works[1,34,63,65,66,68,118,129,156], the central finite-difference approximation should provide a more reliable estimate of the derivative given by Eqs. 4.7 and 4.12. In this case, the interfacial tension can be expressed as:

$$\gamma = \frac{\gamma^{+} + \gamma^{-}}{2} \tag{4.14}$$

where $\gamma^{+}$ and $\gamma^{-}$ are given by Eqs. 4.11 and 4.13, respectively. Special care must be taken when using Eq. 4.14 for determining the interfacial tension of systems that interact through non-continuous intermolecular interactions. The use of Eq. 4.14 assumes implicitly that both expansion and compression perturbations are appropriate to gauge the value of interfacial tension. This is not expected for systems with discontinuous intermolecular potentials, as was first noted by Eppenga and Frenkel[166] some years ago, and more recently by de Miguel and co-workers[156,157]. However, as we deal with continuous intermolecular potentials, the use of Eqs. 4.11, 4.13, and 4.14 is fully justified from a theroretical point of view.

## 4.4 Simulation details

We have applied the methodology proposed in the previous section to study the interfacial properties of a simple fluid confined inside a pore. In particular, the geometry selected for this evaluation is a planar slit pore, composed by two non-structured flat parallel walls separated by a fixed distance, the pore width $H$. The molecules confined inside this pore will be described using a simplified albeit widely used molecular model, consisting of symmetrically spherical molecules whose intermolecular interaction energy is described through the classical Lennard-Jones (LJ) potential

$$u_{ff}(r_{ij}) = 4\varepsilon_{ff}\left[\left(\frac{\sigma_{ff}}{r_{ij}}\right)^{12} - \left(\frac{\sigma_{ff}}{r_{ij}}\right)^{6}\right] \tag{4.15}$$

where $u_{ff}(r_{ij})$ is the intermolecular potential energy between particles $i$ and $j$, that depends only on the distance between the centres of molecules $r_{ij} \equiv |\mathbf{r}_i - \mathbf{r}_j|$. As it is well known, $\sigma_{ff}$ stands for the diameter of the molecular spherical core, and $\varepsilon_{ff}$ is the depth of the pairwise interaction potential. The subscript $ff$ stands for fluid-fluid molecular interactions. The confinement of LJ spheres inside a planar pore has been studied using Monte Carlo molecular simulations by seveal authors [159,168,169].

The molecules are supposed to interact with both confining walls. Among the extensive collection of models proposed in literature to account for solid-fluid molecular interactions, the so-called Steele [170] 10–4–3 potential is very

popular as it has been used to reproduce the interaction with realistic planar solid substrates as for instance graphite. This model considers that the atoms constituting the solid substrate are placed in layers equispaced by a distance $\Delta$, and placed in parallel to the solid-fluid dividing surface. Each of the solid substrate atoms is supposed to interact with every individual fluid molecule through a LJ potential. With this setting, and considering that the atom density in each solid substrate layer is constant, the total interacting energy between a given molecule and one confining wall may be integrated, yielding the following expression:

$$u_{sf}(r) = 2\pi\varepsilon_{sf}\sigma_{sf}^2\rho_S\Delta\left[\frac{4}{10}\left(\frac{\sigma_{sf}}{r}\right)^{10} - \left(\frac{\sigma_{sf}}{r}\right)^4 - \left(\frac{\sigma_{sf}^4}{3\Delta\left(r+0.61\Delta^3\right)}\right)\right] \quad (4.16)$$

where $r$ is the distance from the centre of the molecule to one of the walls. The subscript $sf$ denotes in this case wall-fluid interactions. These characteristic interacting parameteres are defined using the usual Lorentz-Berthelot rules, i.e., $\sigma_{sf} = \frac{1}{2}(\sigma_{ss} + \sigma_{ff})$, and $\varepsilon_{sf} = (\varepsilon_{ss}\,\varepsilon_{ff})^{1/2}$, where $\sigma_{ff}$ and $\varepsilon_{ff}$ are the diameter and dispersive energy parameters corresponding to the LJ wall atoms, respectively. Typical graphite values of $\rho_S = 0.114$ and $\Delta = 3.35$ were selected, representing the solid substrate atom density within each layer, and interlayer spacing, respectively. Since the walls are oriented perpendicular to the $z$-axis and each molecule interacts with two walls, one located at z=0 and the other one at z=H, the total solid-fluid interaction energy felt by a molecule

placed at a distance z from one of the walls is given by

$$U_{sf}^{TOT}(z) = u_{sf}(z) + u_{sf}(H - z) \tag{4.17}$$

In the calculations presented here, the range of both attractions has been considered to be the same, hence $\sigma_{ss} = \sigma_{ff}$, and the ratio $\varepsilon_{sf}/\varepsilon_{ff}$ has been tuned considering different values in order to explore the effect of the relative strength of both interactions on the confined fluid interfacial properties.

We have performed computer simulations in the gran canonical or $\mu$VT ensemble, as well as in the canonical or NVT ensemble, in order to check the methodology proposed in the previous section. The simulation box selected was a parallelepipedic box of dimensions $L_x$, $L_y$ and $L_z$. The flat parallel walls were placed at z=0 and z=$L_z$=H, which means that periodic boundary conditions no longer apply along the z-axis. The pore width, which plays an important role in any study concerning slab geometries as it determines tha capillarity effects induced by the confinement, remained constant in every case, i.e., $L_z \equiv H$ is fixed during Monte Carlo simulations, whatever the thermodynamic ensemble is used.

All simulation runs were organized in cycles. For GCMC simulations, each cycle consisted in N displacement movements and a molecule deletion or insertion trial. The type of movement was in every case selected at random according to their fixed probabilities, and the maximum displacements were

tuned along the simulation to approach a 30% acceptance ratio. Initially, N=512 Lennard-Jones molecules were placed inside the simulation box using a fcc grid. A typical run consisted of $5 \times 10^5$ equilibration cycles followed by a production stage of at least $2 \times 10^6$ cycles. During this last stage averages of the desired interfacial properties were computed (density profiles, interfacial tension, normal and tangential components of the pressure tensor). Simulation box profiles along the z-axis were determined by dividing the box in 100 equal width slabs parallel to the confining surfaces. The uncertainties for the calculated interfacial tension values presented were in all case determined using the block averaging technique, described in Ref.[48]. The NVT runs were identical, except of course for the fact that only translation moves were considered.

Interfacial tension of the system was calculated using the TA methodology explained in the previous section in the $NVT$ and $\mu VT$ ensemble. In addition, the Irving and Kirkwood[67] method was independently applied to determine interfacial tension during GCMC simulations. This last method allows to determine the normal and tangential components of the pressure tensor for the case of planar confinement studied. The pressure is obtained in this case as the contributions from the fluid intermolecular interactions to the normal and tangential components, as follows:

$$P_N^{IK}(z) = \rho(z) k_B T - \frac{1}{2A} \left\langle \sum_{i=1}^{N-1} \sum_{j=i+1}^{N} \frac{|z_{ij}|}{r_{ij}} \frac{du(r_{ij})}{dr} \Theta\left(\frac{z - z_i}{z_{ij}}\right) \Theta\left(\frac{z_j - z}{z_{ij}}\right) \right\rangle \quad (4.18)$$

$$P_T^{IK}(z) = \rho(z)k_BT - \frac{1}{4A}\left\langle \sum_{i=1}^{N-1}\sum_{j=i+1}^{N} \frac{(x_{ij}^2 + y_{ij}^2)}{r_{ij}\cdot|z_{ij}|}\frac{du(r_{ij})}{dr}\Theta\left(\frac{z-z_i}{z_{ij}}\right)\Theta\left(\frac{z_j-z}{z_{ij}}\right)\right\rangle \quad (4.19)$$

where $\Theta$ is the Heaviside function and the subscript $r_{ij}$ refers to the distance between molecules $i$ and $j$. The contribution of the interacting walls produces an additional term to the normal pressure component, which may be described, taking into account that the walls are placed in the geometry selected at z=0 and z=$L_z$, according to:

$$P_N^{walls,IK}(z) = \frac{1}{A}\left[\left\langle \sum_{i=1}^{N} F_w(z_i)\Theta(z_i - z)\cdot\Theta(z)\right\rangle - \left\langle \sum_{i=1}^{N} F_w(L_z - z_i)\Theta(L_z - z)\cdot\Theta(z - z_i)\right\rangle\right] \quad (4.20)$$

where N is the number of confined fluid molecules, and $F_w(z)$ is given by

$$F_w(z) = \frac{du_w(z)}{dz} \quad (4.21)$$

The calculation of the interfacial tension from the computed normal and tangential components of pressure tensor is then straightforward, using the classical mechanical route definition:

$$\gamma_{IK} = \frac{1}{2}\int_0^{L_z}\left(\ P_N^{IK}(z) + P_N^{walls,IK}(z) - P_T^{IK}(z)\right)\ dz \quad (4.22)$$

## 4.5 Results

Once the technical and theoretical justification for the application of the TA method in the grand canonical ensemble has been established, a test will be

performed on a benchmark system, with the aim to provide a first insight into the quantitative equivalence of the application of TA method in the canonical and grand canonical ensembles. In particular, we compare the quantitative performance of the TA approach in the calculation of interfacial tension for a slab confined fluid in the NVT and $\mu$VT ensembles. Keeping this in mind, it is very important to set the thermodynamic conditions for both runs to be as equivalent as possible, and with this aim the calculation routes exposed in Sec. III, comprising respectively two or three simulation runs were followed.

In the following discussion, the fluid-fluid dispersive energy parameter $\varepsilon_{ff}$ and the diameter $\sigma_{ff}$ are chosen as the units of energy and length, respectively. According to this, we define the following reduced quantities: temperature, $T^* = k_B T/\varepsilon_{ff}$; pressure, $P^* = P\sigma_{ff}^3/\varepsilon_{ff}$; density profile, $\rho^* = \rho\sigma_{ff}^3$; chemical potential, $\mu^* = \mu/\varepsilon_{ff}$; surface tension, $\gamma^* = \gamma\sigma_{ff}^2/\varepsilon_{ff}$; pore size, $H^* = H/\sigma_{ff}$; and distance from one of the walls, $z^* = z/\sigma_{ff}$.

The procedure has been then the following. Initial values of $T^* = 2.001$ and $P^* = 0.136$ have been selected as reference working conditions. The reason for this choice is that, if the molecule of methane is modeled as a single LJ sphere, these reduced coordinates correspond to the usual conditions found in real Tight Gas Reservoirs (TGRs)[130], a case study that is very relevant from a practical perspective, and where the fluid interfacial properties play a crucial role. As mentioned in section III, the calculation of the solid-fluid interfacial tension of a confined system involves, if the TA methodology could be applied

Table 4.1: Solid-fluid interfacial tension of LJ molecules adsorbed on slit-like pores of different pore widths $H^*$ and dispersive energy ratio $\varepsilon_{sf}/\varepsilon_{ff} = 2.0$. $\gamma^*_{TA-\mu VT}$, $\gamma^*_{TA-NVT}$, and $\gamma^*_{IK}$ are the interfacial tensions obtained from the TA method in the grand canonical ensemble, from the TA in the canonical ensemble, and from the Irving-Kirkwood procedure in the grand canonical ensemble, respectively.

| $H^*$ | $\gamma^*_{TA-\mu VT}$ | $\gamma^*_{TA-NVT}$ | $\gamma^*_{IK}$ |
|---|---|---|---|
| 4 | −43.67(7) | −43.64(3) | −43.70(8) |
| 5 | −33.1(5) | −33.7(5) | −33.20(6) |
| 8 | −27.2(5) | −27.7(5) | −27.27(7) |
| 10 | −28.2(5) | −28.8(5) | −28.16(6) |

during a GCMC simulation, a two-steps procedure. In the first step, a simulation of the described bulk LJ fluid was performed in the isothermal-isobaric or NPT ensemble at the selected $P^*$ and $T^*$ conditions, in order to determine the chemical potential value. The chemical potential was determined using the classical Widom particle insertion method[165]. This preliminar simulation yielded a value of $\mu^* = -10.86(3)$.

In a second step, the information obtained in the preliminar simulation is then used to perform a simulation of the confined fluid in the grand canonical ensemble at the chemical potential obtained during the (bulk) NVT simulation. It is important to recall here that this is the standard procedure if ones intends to mimick the setup used in experimental adsorption studies, i.e., a gas reservoir in equilibrium with the confined system at the same temperature and chemical potential. During this second simulation, the average denstiy

of molecules inside the pore (adsorbed molecules) is calculated. In particular, the average density value inside the pore, in equilibrium with the bulk phase at $T^* = 2.001$ and $P^* = 0.136$, was $\rho^* = 0.0739(6)$. In addition to that, we apply the extension of the TA procedure proposed in Sec. III and calculate the solid-fluid interfacial tension of LJ molecules confined in the pore. We also apply the Irving-Kirkwood method for determining independently along the grand canonical simulation the normal and tangential components of the pressure tensor, and hence, the interfacial tension.

Although this procedure is enough to have reliable values of the solid-fluid interfacial tension, we have performed an additional and independent simulation of the confined system in the canonical ensemble at the same (constant) density as that obtained in the second simulation previously mentioned ($\rho^* = 0.0739$), and calculate the solid-lfuid interfacial tension of the confined system using the TA method in the canonical or NVT ensemble as originally described by Gloor *et al.*[63].

We have applied the procedure explained in the previous paragraphs to calculate the solid-fluid interfacial tension of spherical molecules inside a slit-like pore for different confining conditions of pore widths H and solid-fluid relative strength $\varepsilon_{sf}/\varepsilon_{ff}$. We first consider the influence of the pore width for a fixed ratio $\varepsilon_{sf}/\varepsilon_{ff} = 2.0$. Fig. 1 shows the density profiles inside the pore at $T^* = 2.001$ and $P^* = 0.136$ for different values of the pore width. As can be seen, simulationsin the grand canonical ($\mu$ VT) and canonical (NVT)

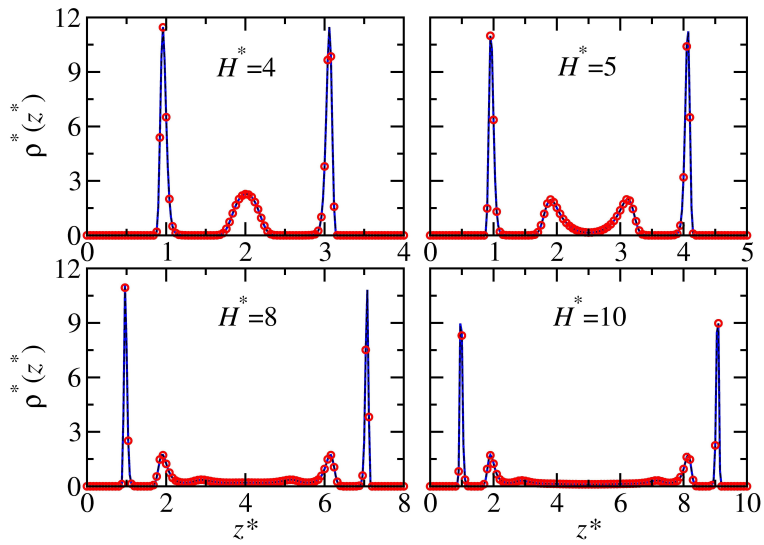


Figure 4.1: Density profiles of LJ molecules adsorbed on slit-like pores with different pore widths $H^*$. Solid lines represent GCMC results at $\mu^* = -10.86$ and $T^* = 2.001$, and symbols represent $NVT$ results at the same temperature and $\rho^* = 0.0739$.

ensembles give identical profiles, as expected since the same system is simulated using different ensembles but at equivalent thermodynamic conditions. Results indicate that the system develops the expected structure and layering effects inside the pore, and more importantly, the correct behaviour as the pore size is varied. In particular, the system exhibits three layers, two of them located at one sigma of distance from the each wall (located approximately at positions at which the solid-fluid intermolecular potential exhibits two min-

Table 4.2: Solid-fluid interfacial tension of LJ molecules adsorbed on slit-like pores of pore width $H^* = 8$ and different dispersive energy ratios $\varepsilon_{sf}/\varepsilon_{ff}$. $\gamma^*_{TA-\mu VT}$, $\gamma^*_{TA-NVT}$, and $\gamma^*_{IK}$ represent the same as in the caption of Table 4.1.

| $\varepsilon_{sf}/\varepsilon_{ff}$ | $\gamma^*_{TA-\mu VT}$ | $\gamma^*_{TA-NVT}$ | $\gamma^*_{IK}$ |
|---|---|---|---|
| 0.5 | −2.49(2) | −2.49(2) | −2.49 |
| 1 | −10.19(6) | −10.20(6) | −10.18 |
| 1.5 | −20.0(2) | −20.2(3) | −19.98 |
| 2 | −27.2(5) | −27.8(5) | −27.27 |

ima), and the third located in the centre of the pore. As the pore size is increased, the confined system exhibits four ($H^* = 5$), and six layers ($H^* = 8$ and 10) located symmetrically inside de pore. Note that for the larger pores ($H^* = 8$ and 10), the system develops a nearly homogenenous adsorption or bulk-like behaviour in the centre of the pore, an expected behaviour since interactions between the walls and molecules located in this region become smaller in comparison with fluid-fluid interactions as $H^*$ increases.

Results corresponding to the solid-fluid interfacial tension for the fixed ratio $\varepsilon_{sf}/\varepsilon_{ff} = 2.0$ and different pore widths calculated using three independent methods are presented in Table 4.1. As can be seen, the interfacial tension values are nearly identical is all cases using three alternative methods, demonstrating the complete equivalence between the use of the TA methodology in the canonical and gran canonical ensembles when using similar thermodynamic conditions. It is important to recall here that the use of the TA method in the grand canonical ensemble allows to evaluate the interfacial tension and

all the thermodynamic and structural properties of the confined system in the same simulation, without the need of any additional calculation. As can be seen in Fig. 4.2(a), the solid-fluid interfacial tension becomes larger (less negative) as the pore size increases, and it seems to develop an asymptotic limitin behaviour as the pore size approaches to 8-10 (in reduced units), approximately. The structure of the adsorbed layers, at sufficiently large pores, does not change significantly as the pore size is increased, and it is expected that the solid-fluid interfacial tension does not vary too much in these cases.

A similar behaviour in the structure of the adsorbed systems is obtained when considering a fixed pore size, $H^* = 8$, and vary the relative strength of $\varepsilon_{sf}/\varepsilon_{ff}$. Although we have not shown the results here, we have observed the expected behaviour, i.e., increase of the molecules adsorbed inside the pore and a more structured density profiles as $\varepsilon_{sf}/\varepsilon_{ff}$ increases from 0.5 up to 2.0.

The influence between the relative strength between the fluid molecules and the fluid-wall interactions was studied by setting the ratio $\varepsilon_{sf}/\varepsilon_{ff} = 0.5$, 1, 1.5 and 2.0, for a fixed pore width of $H^* = 8$. Agreeement between interfacial tensions obtained with the three methods is also excellent within the statistical uncertainty of the simulations, as can be observed in Table 4.2. Fig. 4.2(b) shows the solid-fluid interfacial tension, as a function of $\varepsilon_{sf}/\varepsilon_{ff}$, for the pore considered. As can be seen, the interfacial tension becomes more negative as the energy ratio increases since the walls are more attractive, and hence, interacting more cohesively with the fluid adsorbed. Agreement between interfacial

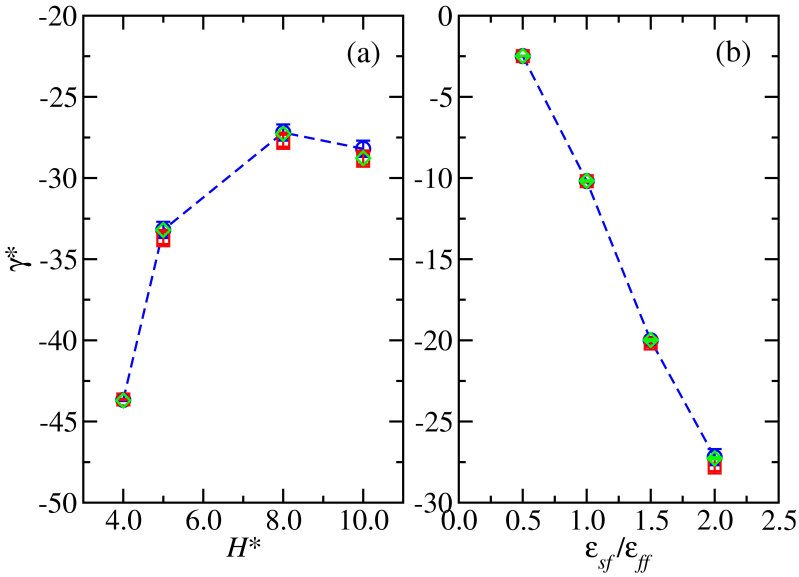


Figure 4.2: Solid-fluid interfacial tension of LJ molecules adsorbed on slit-like pores of (a) different pore widths $H^*$ and dispersive energy ratio $\varepsilon_{sf}/\varepsilon_{ff} = 2.0$ and (b) pore width $H^* = 8$ and different dispersive energy ratios $\varepsilon_{sf}/\varepsilon_{ff}$ obtained from the TA method in the grand canonical ensemble (blue circles), from the TA method in the canonical ensemble (red squares), and from the Irving-Kirkwood procedure in the grand canonical ensemble (green triangles). The blue dashed line is a guide to the eye.

tensions obtained from different methods are nearly identical, indicanting the advantage of using the TA procedure along a grand canonical Monte Carlo simulation when studying adsorbed systems on pores.

## 4.6 Conclusions

We have extended the TA methodology, originally proposed to evaluate the surface tension of vapour-liquid interfaces along a computer simulation in the canonical ensemble, i.e., at constant number of particles, volume, and temperature, to calculate solid-fluid interfacial tension of systems adsorbed on slit-like pores. This has been done by using the generalisation of the grand potential free energy for systems exhibiting two-phase direct coexistence and expressing the interfacial tension as the derivative of the corresponding free energy with respect to the interfacial area. Thus, the interfacial tension can be computed along a simulation in the grand canonical ensemble, i.e., at constant chemical potential, volume, and temperature, by performing fictitious increasing and decreasing interfacial area changes and averaging the corresponding Boltzmann factor associated with the surface area perturbation over the unperturbed system.

The main advantage of this methodology is that it allows to calculate simultaneously the density profiles and the amount of molecules adsorbed onto a slit-like pore, as well as the solid-fluid interfacial tension. Contrary, the evaluation of the solid-fluid interfacial tension using the original TA methodology requires an additional and independent simulation in the NVT ensemble, at the same average chemical potential and density, which makes the proposed methodology clearly more advantageous than the original one. In addition

to that, the new method ensures that the chemical potential at which all properties are evaluated during the simulation is exactly the same since the simulation is performed in the grand canonical ensemble, mimicking the conditions at which the adsorption experiments are most usually carried out in the laboratory.

We have applied the new methodology performing grand canonical Monte Carlo computer simulations to calculate the density profiles and interfacial tension of spherical molecules, interacting through the Lennard-Jones intermolecular potential, adsorbed in slit-like pores with different pore sizes and solid-fluid dispersive energy parameters. In order to check that predictions obtained from the new methodology give the same results as those using the original technique, we have also performed computer simulations in the NVT ensemble with a number of particles equal to the average obtained at constant chemical potential. Density profiles obtained from computer simulations in the NVT and $\mu$VT ensembles are nearly identical for all the pore sizes and solid-fluid dispersive energies considered. An excellent agreement has been also found, to the statistical uncertainties, between solid-fluid interfacial tension obtained from simulation in both ensembles, for all the cases considered. We have also determined the interfacial tension from the mechanical expression by determining the normal and tangent components of the pressure tensor using the Irving-Kirkwood recipe, finding the same results as those obtained from the TA technique.

# Chapter 5

# Monte Carlo simulation of interfacial properties of water, carbon dioxide and methane under confinement

## 5.1 Abstract

Monte Carlo molecular simulation results are presented for systems consisting on pure water (TIP4P/2005 molecular model), carbon dioxide ($CO_2$-IMP) and methane (Lennard-Jones) molecules confined between parallel walls. Two different models have been considered for the walls, the first one considers them to be completely hard, without any interaction with the fluid molecules, and the second considers graphite walls whose interaction with the fluid molecules is modelled by a Steele 10-4-3 potential. The influence on the fluid density profiles along the pore and interfacial tension is discussed, at temperature and pressure conditions similar to those found in tight gas reservoirs.

## 5.2 Introduction

Global warming caused by increasing amounts of greenhouse gases (GHGs) in the atmosphere is undoubtedly one of the most important environmental issues nowadays. It constitutes a global scale problem, and international organizations such as the United Nations Framework Convention on Climate Change (UNFCCC) and the Intergovernmental Panel on Climate Change (IPCC) have been created to coordinate research efforts and elaborate collaborative strategies. The Earth is warmed by the incoming solar radiation, and it naturally emits longer wavelength thermal radiation back into space. However, some of this terrestrial infrared radiation is absorbed by gaseous constituents in the

atmosphere, the so-called GHGs[171] (such as $H_2O$, $CO_2$, $N_2O$, $CH_4$, $O_3$, etc.), and re-emitted in all directions, warming the atmosphere[172]. The IPCC reported that the Earth's average global surface temperature increased 0.6±0.2 K over the twentieth century, producing a rise in sea level of 0.1±0.2 m[173,174]. In addition, natural processes related with changes in GHG concentration produce global fluctuations in temperature, precipitation and wind regimes[175–177].

Carbon dioxide has been targeted as the main responsible for changes in the Earth's radiation balance, and it is the most abundant GHG emitted from industrial processes, such as cement production, and fossil-fuel combustion for power generation, transportation and heating. It is widely agreed (see for instance White *et al.*[178]) that the three most feasible options to reduce $CO_2$ emissions and stabilize atmospheric levels of GHGs without severely impacting current standards of living are: increasing energy efficiency[179,180], switching to less carbon-intensive sources of energy[181], or GHGs sequestration[182]. The third option cited refers to the removal and long-term storage of GHGs from the atmosphere or emission sources, using for this purpose deep unmineable coal seams, deep saline aquifers, or depleted petroleum reservoirs, and $CO_2$ is focusing most of the efforts. Geological sequestration represents a technologically feasible, safe and verifiable option to meet the GHG emission targets and stabilize atmospheric $CO_2$ concentration. On the other hand, $CO_2$ is a useful product for many petroleum companies who inject it into the so-called tight gas reservoirs (TGRs), with the aim to displace methane adsorbed on

low permeability substrates, enhancing natural gas recovery, and aiming at the same time to the geological trapping of the injected external fluid in the process. Methane constitutes undoubtedly an interesting case study in this context as it constitutes the main component of natural gas, and concerning water, its role in Petrophysics is crucial[183,184], for instance, in the extraction processes employed usually in non conventional natural gas sources (TGRs), where the injection of an external aqueous based fluid modifies the natural gas adsorption on the solid substrate, enhancing fluid recovery[185].

In this context, interfacial properties and fluid-substrate interaction at molecular scale determine the macroscopic behaviour of the transport properties of the fluid, and contributions in this field are essential in order to gain insight into the involved molecular physics phenomena. Thus, advances towards a detailed theoretical description of interfacial structure and properties of different fluid phases and solids are of primary interest. This includes, from a theoretical perspective, contributions from different directions. For instance, the global phase equilibria of mixtures containing the fluids of interest is rather complex and analysis using theoretical molecular models to describe the involved bulk multicomponent mixtures is a reliable starting point to further studies concerning fluid interfaces (see e. g. Míguez *et al.*[130]). The interfacial properties may then be studied using different inhomogeneous media modelling approaches, as the Density Functional Theory (for instance, Georgiadis *et al.*[186] have recently presented a detailed account of the water or n-alkane +

$CO_2$ interfaces), or the Gradient Theory (see Lafitte *et al.*[131], and references therein). Molecular Simulation (MS) is another reliable and powerful tool to study interfacial properties of multiphase inhomogeneous fluids and over the last few years a number of relevant contributions have been presented in this field, including new calculation methods to determine interfacial properties. Some examples of these novel calculation techniques are the Test-Area (TA)[63], wandering interface method (WIM)[64], or Expanded Ensemble[65] methods. All of them combine versatility and reliability, and as an example of the rapid acceptance they are meeting the TA has already been applied to the cases of Lennard-Jones chains[68], water[1], the Mie potential[73,74], binary mixtures[70,158] etc. Nevertheless, the interfaces between solid and fluid phases have been less studied than fluid-fluid interfaces, while its detailed description is essential to describe a range of phenomena including adsorption, capillarity, wetting, etc. A common feature of the estimation of interfacial properties by MS is that they are remarkably CPU time demanding, but they allow a rigorous analysis of the connection between the details of the tested molecular models and the scarce experimental macroscopic interfacial properties data.

The objective of this work is to apply Monte Carlo (MC) simulation to describe the interfacial behaviour of three pure fluids (methane, carbon dioxide and water) confined in slab geometry, and the modification of the bulk fluid properties due to the presence of a solid substrate, which is intended to help to understand the real behaviour of these substances in oil or natural gas

reservoirs. Methane is often represented in MS using a single Lennard-Jones (LJ) sphere[132]. This molecular model, despite its simplicity, offers fair quantitative results not only for phase equilibria and coexisting phase densities, but also for more sensitive thermophysical properties as second order derivative properties, as shown in previous works[187,188]. A comprehensive revision of molecular simulation models for methane and other alkanes, and their applications in oil and gas industry has been recently published by Ungerer *et al.*[189]. The confinement of a LJ fluid in a slit pore has been also studied considering different theoretical approaches, as for instance the Density Functional Theory (Berim and Ruckesnstein[190], Sweatman[191]), or Monte Carlo (MC) simulations (Oleinikova and Brovchenko[168], Dominguez *et al.*[169]). Carbon dioxide has been described in this case using the so-called isotropic multipolar model (IMP)[192], considering the characteristic parameters presented by Galliero *et al.*[193]. For these two molecules, some preliminary calculations on coexistence densities and liquid vapour interfacial tension have been computed as an introductory step to check the quantitative agreement of the models with experimental data. Water has been modelled here using the four interacting sites TIP4P/2005 parameterization[106]. For the case of molecules including polar or coulombic interactions, studies concerning interfacial properties are still scarce. Two flat parallel structureless walls, placed at a fixed distance, compose the slab. The interaction between the walls and the fluid molecules has been considered using two models. First, non interacting walls were con-

sidered, i.e., the fluid molecules centres of mass were allowed to reach the wall. The other interaction selected was the so called Steele 10-4-3 potential[170], a common option to represent fluid adsorption on a solid surface[191], that represents quantitatively well the interaction with real substrates as graphite. The confined fluid pore density profiles have been computed in each case at T,P conditions close to those found in TGRs, and interfacial tension has been computed using both TA method[63] and the usual mechanical route that entails the calculation of tangential and normal pressure components to the interface, as detailed by de Miguel and Jackson[66].

## 5.3 Molecular models and Simulation details

### 5.3.1 Molecular models considered

The first step of this work consisted in the selection among the molecular models available to describe each of the species studied. The case of methane presented no doubts, because as cited the LJ model is quantitatively very precise in the determination of bulk properties. In the case of carbon dioxide, many approaches are available in literature, ranging from the simpler one that considers that all polar effects may be embodied in the appropriate determination of the characteristic parameters of a LJ interaction potential, to more developed models including the explicit consideration of point electric charges ($CO_2$-EPM2[15]) that entail the adequate treatment of coulombic long-

range interactions. As the determination of interfacial properties needs long equilibration runs, their calculation is considerably CPU time demanding. An intermediate compromise between computing times and quantitative agreement may be achieved for $CO_2$ with the so-called isotropic multipolar (IMP) models, described for instance by Müller *et al.*[192] and Galliero *et al.*[193], which considers that all polar effects may be described using a multipolar term averaged over all molecular orientations. This approximation is more reliable at higher temperatures and lower densities.

Concerning water, the molecular model used in this case was TIP4P/2005[106]. Vega and de Miguel[1] presented a comparative analysis of the performance of different water models in the determination of LV interfacial properties through molecular simulation. The authors conclude that the TIP4P/2005 version of the model is quantitatively more accurate than the other water models. In a recent paper[129], we have shown that the Reaction Field used to handle electrostatic interactions produces equivalent results to the Ewald sum method in the determination of interfacial properties of TIP4P/2005 water, with a considerable reduction of computing times. With these preliminary studies, the TIP4P/2005 model has been selected, combined with the RF method to account for coulombic long-range interactions, while for the LJ part of the potential the same cut-off radius than in the precedent case has been fixed.

### 5.3.2 Simulation details for VLE calculations

Before using these $CO_2$ models to examine the behaviour of the confined fluid, a preliminary test was made to determine its quantitative ability in the estimation of vapour-liquid interfacial properties. With this aim, MC simulations in a biphasic simulation box containing the liquid and vapour phases in coexistence were performed. The method used to reproduce these interfaces was quite similar to the one proposed by Gloor *et al.*[63]: a cubic box containing 1372 molecules of the fluid in close to real coexistence conditions was equilibrated using NPT MC, starting form an initial fcc ordered configuration. All simulations in this work were organized in cycles, each of them consisting in N-which stands for the number of molecules-attempts to move a particle, one volume change try in NPT calculations, and N attempts to rotate a molecule in the case of water. Maximum translation, rotation and volume displacements were tuned along the simulation runs to approach a 33% acceptance ratio. Once the equilibrium was reached (typically after $3 \times 10^5$ cycles), two identical size empty boxes were added on the top and bottom of this original liquid like box, and the system was allowed to evolve under NVT conditions until the two liquid vapour interfaces, parallel to the XY plane, were stabilized, a process which usually takes around $5 \times 10^5$ cycles. The simulation box was divided into 100 equal size slabs in order to determine the density profile along the z-axis. Once the system is again fully stabilized, the resulting configuration is used as starting point of a $2 \times 10^6$ cycles NVT run, used to

determine surface tension using both the TA method[63], and the calculation using the mechanical route, that entails the determination of the pressure tensor components, performed following the method proposed by de Miguel and Jackson[66].

Another feasible option to reduce computing times when a model including point electric charges is considered (as it is the case of EPM2 model) is the application of the alternative Reaction Field[83] (RF) method to describe the coulombic interactions in the case of molecular models including point electric charges. In recent works, it has been shown that the RF method produces quantitative accurate results for interfacial properties, if compared with the Ewald sum method. This is the case for instance for pure water biphasic simulations with explicit liquid-vapour interface[129] or in calculations involving water solid-liquid equilibria[103,104].

### 5.3.3 Simulation details for confined systems

For confined fluid calculations, the simulation box selected was a parallelepipedic box of $L_x$, $L_y$ and $L_z \geq 10\sigma_i$, where $\sigma_i$ stands as the Lennard-Jones core parameter value for each of the molecules studied, which is often used as reference distance for this type of confined configurations[194]. The flat parallel walls were placed at $z = 0$ and $z = L_z$, which means that periodic boundary conditions no longer apply in the $z$ direction. The pore width remained constant in every case, i.e., $L_z$ is constant during isothermal-isobaric (NPT)

simulations, when the volume displacements were obtained by either modifying the box dimensions along the $x$ or $y$ axis. The pore width plays an important role in any study concerning slab geometries as it determines the capillarity effects induced by the confinement. Real porous substrates usually present a broad pore size distribution function, that must be accounted for performing simulations at different pore widths and then combining the results. A detailed description of these phenomena has been presented for instance by Evans *et al.*[195].

With the settings detailed above, calculations were performed in slab confinement at T=413.15 K and P=30 MPa, because these conditions are representative of the ranges supposedly found in real TGRs. Two different interactions where considered between the wall and the fluid molecules. In the first case the walls are considered as infinite step potentials, allowing the centre of mass of the molecule to reach the wall, and this case will be referred to as hard walls. In the second case the wall is described by a soft continuous potential, the so-called Steele 10-4-3 potential, which is representative for instance of the interaction with a solid planar graphite substrate[191]. For this type of integrated potentials, the interaction energy between each particle and the pore $U_w(r)$ depends only on the distance $r$ from the centre of mass to each of both walls.

$$u_w(r) = \varepsilon_w \left[ \frac{4}{10} \left( \frac{\sigma_w}{r} \right)^{10} - \left( \frac{\sigma_w}{r} \right)^{4} - \left( \frac{\sigma_w^4}{3\Delta \left( r + 0.61\Delta^3 \right)} \right) \right] \qquad (5.1)$$

where $\sigma_w = 0.903\sigma_i$, $\varepsilon_w = 12.96\varepsilon_i$ , and $\Delta = 0.8044\sigma_i$, and the subscript $i$ refers to the LJ core characteristic parameters of each molecule.

The presence of the walls breaks the periodicity along the $z$-axis direction, and this has an effect on pressure components. The confining walls are placed at $z = 0$ and $z = L_z$, and the $L_z$ distance is fixed, while the other two distances, $L_x$ and $L_y$, are allowed to fluctuate along NPT MC calculations. Under these conditions, at least two different components of pressure should be computed. The first one is tangential to the walls, $P_t(z) = P_{xx}(z) = P_{yy}(z)$, and the second one is normal $P_n(z) = P_{zz}(z)$. With the configuration and method of calculation described, the thermodynamic pressure of the system is coincident with the normal component, while the input pressure value fixed for the calculation corresponds to the spatial average of the tangential compound, and the numerical values of the normal and tangential components are not coincident. The normal pressure component value is expected in this case to be lower than the set input pressure, and this difference is density dependent, so a study concerning for instance phase transitions considering only the input pressure is not formally correct and the normal pressure calculation should be taken into account. In this work, the 30 MPa pressure value declared for the calculations is the input pressure, but normal and tangential components of pressure have been computed as well in order to compute interfacial tension using the mechanical route.

## 5.4 Results and discussion

### 5.4.1 Choice of cut-off radius value for each system considered

A relevant question in interfacial properties determination using Molecular Simulation is the cut-off radius ($r_c$) used to compute the system internal energy, and the eventual use of long-range corrections. Interfacial tension values are very sensitive to the cut-off radius used during the simulations, as shown by Gloor *et al.*[63]. Several authors have proposed analytical expressions for the long-range corrections in inhomogeneous systems, as for instance Janecek[111], MacDowell and Blas[119], or Ibergay *et al.*[69]. Despite this, in different works[73,196] it has been shown that beyond a certain value of the cut-off radius the computed interfacial tension reaches a plateau for LJ like potentials. As an example of this, Fig. 5.1 shows the evolution of the coexisting phase densities and interfacial tension computed for methane, with different cut-off radius values. This figure plots the values of liquid and vapour density, and interfacial tension, in every case weighed over the largest cut off radius value, i.e.:

$$\rho_l^* = \frac{\rho_l(r_c)}{\rho_l(10\sigma_{LJ})} \tag{5.2}$$

This figure shows clearly that beyond $r_c = 5\sigma_{LJ}$, the influence of cut-off radius value for interfacial properties is almost negligible for LJ like interaction potentials. Thus, in this work, no long-range corrections have been applied for the case of pure carbon dioxide and methane because we have used cut-off

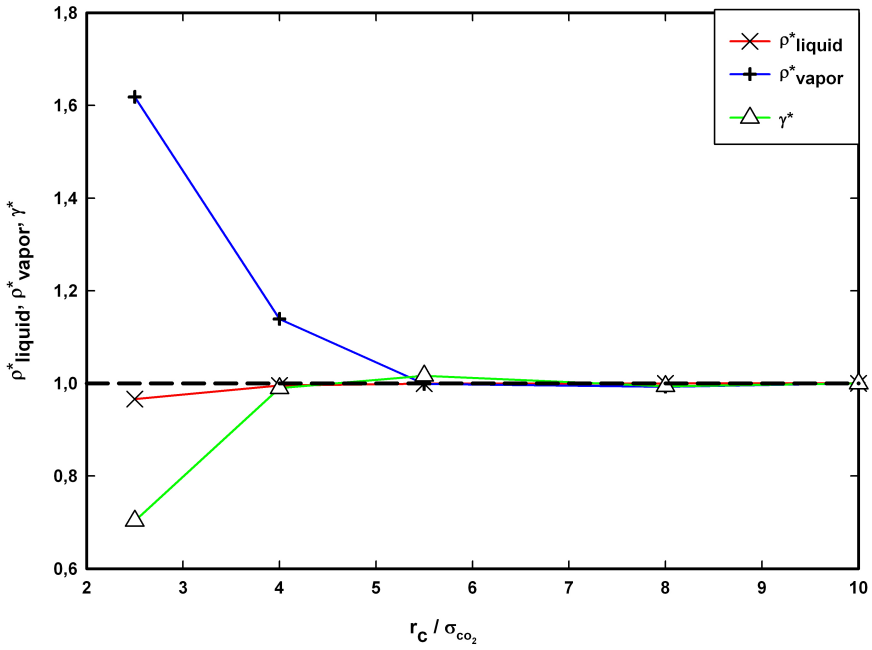


Figure 5.1: Variation with cut-off radius of the longest cut-off radius weighed coexisting phases densities and interfacial tension for vapour-liquid equilibrium of pure methane, computed at T=120 K using MC calculations.

radius values higher than $6\sigma_i$ (where $\sigma_i$ represents the LJ core radius for each of the molecules studied) in all our simulations.

Interfacial tensions were then calculated for methane and carbon dioxide, the latter with IMP and EPM2 models. The results obtained, compared with experimental data gathered from NIST[197], are presented in Table 5.1. As usual, the agreement between both methods used to determine interfacial ten-

sion (TA and mechanical route) is within the statistical error, determined in every case by block averaging. In fact, for every point both values agree at least to the third significant figure. The qualitative agreement for interfacial tension is correct in the case of methane (LJ) and $CO_2$-EPM2, and as expected the accuracy is better for higher temperatures for $CO_2$-IMP molecular model in the case of $CO_2$. Nevertheless, $CO_2$-EPM2 model is less accurate than $CO_2$-IMP in the estimation of coexisting phases densities. For the following calculations of confined systems, the IMP model has been selected for carbon dioxide.

Table 5.1: Comparison between Monte Carlo computed and recommended experimental values for coexisting phase densities ($\rho_l$ and $\rho_v$, both in kg m$^{-3}$) and surface tensions($\gamma$/ mJ m$^{-2}$), for the case of unconfined methane, carbon dioxide, and water, using the molecular models described in the text. Interfacial tension values were calculated using the Test-Area (ta) and mechanical route (mr) techniques.

| $T/K$ | $\rho_l$ | | $\rho_l^{exp}$ | $\rho_v$ | | $\rho_v^{exp}$ | $\gamma_{ta}$ | | $\gamma_{mr}$ | | $\gamma^{exp}$ |
|---|---|---|---|---|---|---|---|---|---|---|---|
| | | | | | $CH_4$(LJ) | | | | | | |
| 120 | 407(2) | | 409.90 | 3.1(2) | | 3.26 | 12.3(8) | | 12.4(9) | | 11.31 |
| 140 | 374(1) | | 376.87 | 9.8(4) | | 10.15 | 8.2(6) | | 8.2(6) | | 7.05 |
| 160 | 335(1) | | 336.31 | 23.4(7) | | 25.38 | 3.5(7) | | 3.5(3) | | 3.52 |
| | | | | | $CO_2$(IMP-EPM2) | | | | | | |
| | $IMP$ | $EPM2$ | | $IMP$ | $EPM2$ | | $IMP$ | $EPM2$ | $IMP$ | $EPM2$ | |
| 217 | 1192(5) | | 1177.0 | 15.6(4) | | 13.99 | 19.6(7) | | 19.6(9) | | 17.05 |
| 227 | 1146(5) | | 1140.1 | 22.6(3) | | 20.79 | 16.3(5) | | 16.3(7) | | 14.59 |
| 237 | 1104(3) | 1083(3) | 1101.1 | 33(1) | 36(1) | 29.98 | 13.8(6) | 12.6(5) | 13.7(5) | 12.6(4) | 12.21 |
| 247 | 1059(2) | | 1059.2 | 46.9(6) | | 42.23 | 10.9(4) | | 10.8(3) | | 9.93 |
| 257 | 1007(2) | 985(4) | 1013.5 | 64(1) | 67(1) | 58.53 | 8.4(3) | 7.8(3) | 8.4(3) | 7.8(4) | 7.76 |

As a preliminary test of the influence of the cut-off radius on the computed density profiles, Fig. 5.2 shows the simulation box density profile along $z$ di-

rection, for 1372 $CO_2$-IMP molecules confined between hard walls, with a pore width of $L_z = 12\sigma_{LJ}$, at T=413.15 K and P=30 MPa, and cut-off distances of $r_c$=2.5$\sigma_{LJ}$, 5.5$\sigma_{LJ}$, and 10$\sigma LJ$. The shorter value produces a profile that is significantly different, and this fact must be taken into account, while for the larger values the profiles are coincident. The shape of this profile has been denoted by Berim and Ruckenstein[190] as cup-like profile, and it is typical of LJ like interacting segments. In every case, an adsorbed layer appears in each wall. This first adsorbed layer produces then a minimum in density, due to the mutual exclusion of the LJ intermolecular potential cores, and density in the middle of the pore increases, but a bulk region is not clearly observable in this configuration, as the density does not reach a clear plateau.

### 5.4.2 Results for confined configurations

The same calculation was repeated (Fig. 5.3) for the three molecular species considered, in the same conditions noted, either without wall fluid interaction (Fig. 6.3a) or with the Steele potential (Fig. 6.3b). Fig. 6.3a evidences the different behaviour of each of the species considered. For the case of methane, the structure of weakly adsorbed layer, followed by a density minimum, leads to a bulk with constant density. The same trend appears for IMP carbon dioxide, but the range of the effect of the wall is longer in this case, and the central bulk density is recovered at a longer distance, which can be seen as the effect of the integrated multipolar term, the only difference with the

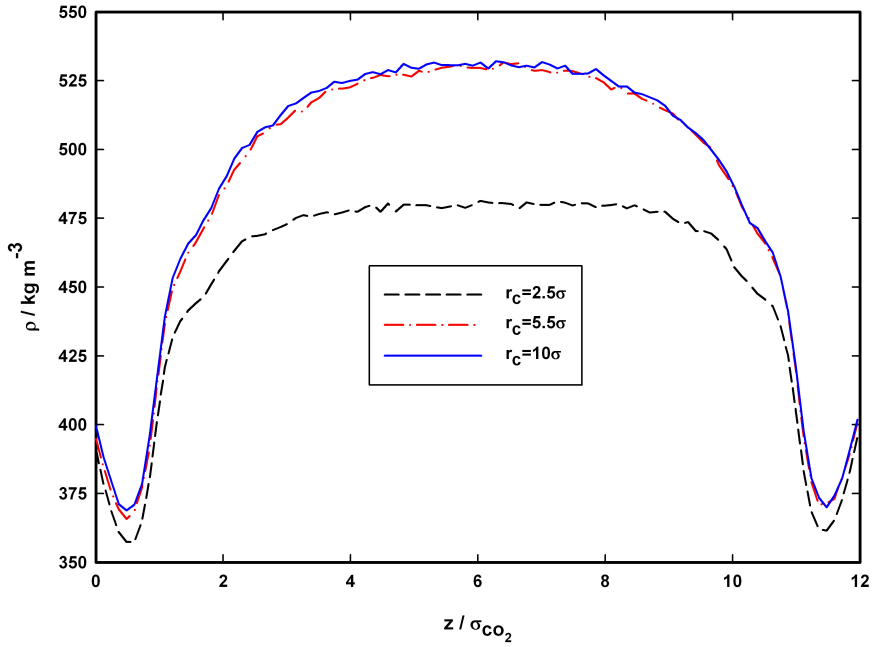


Figure 5.2: Density profile for a hard wall slit pore ($L_z = 12\sigma_{CO_2}$) containing IMP $CO_2$ at T=413.15 K and P=30 MPa, for different cut-off radius values: $r_c = 2.5\sigma_{LJ}$ (dashed line); $r_c = 5.5\sigma_{LJ}$ (dash-dot line), and $r_c = 10\sigma_{LJ}$(solid line).

methane pure LJ model, which adds an attractive term between the fluid molecules. This level of intermolecular attraction is more evident for the case of water, where a sharp density minimum appears in the vicinity of the wall. This may be explained as an effect of the associative interaction between molecules, which is broken by the presence of the inert wall, and produces this effect. Table 5.2 presents the data of interfacial tension computed for each

case, together with the system internal energy, and average density at the centre of the slab. The results show that the interfacial tension increases with the cohesive intermolecular interaction, as shown by a comparison of average internal energies and interfacial tension values.

Table 5.2: Computed values using Monte Carlo simulation of pure confined fluid interfacial tension($\gamma$/ mJ m$^{-2}$), bulk density($\rho$/ kg m$^{-3}$), and internal energy($U$/ kJ $mol^{-1}$), for pores widths of $L_z = 12\sigma_{LJ}$ and $24\sigma_{LJ}$, considering the case of non interacting hard wall and Steele potential interacting wall.

| *Pore width* | $L_z = 12\sigma_{LJ}$ | | | | $L_z = 24\sigma_{LJ}$ | | | |
|---|---|---|---|---|---|---|---|---|
| | $\gamma_{ta}$ | $\gamma_{mr}$ | $\rho_{bulk}$ | $U$ | $\gamma_{ta}$ | $\gamma_{mr}$ | $\rho_{bulk}$ | $U$ |
| | | | | *Non interacting walls* | | | | |
| $CH_4$ | 1.34(3) | 1.34(3) | 137.7(2) | −1.820(4) | 1.37(3) | 1.37(3) | 136.5(2) | −1.890(4) |
| $CO_2$ | 3.76(3) | 3.76(3) | 529(2) | −3.866(5) | 3.75(3) | 3.75(3) | 522(1) | −4.028(6) |
| $H_2O$ | 63.1(7) | 63.3(8) | 947(3) | −40.22(2) | 63.6(9) | 63.5(8) | 943(4) | −40.65(1) |
| | | | | *Steele potential* | | | | |
| $CH_4$ | 25.9(6) | 26.0(5) | 89.4(4) | −5.163(3) | 29.0(8) | 28.9(7) | 110.1(3) | −3.565(4) |
| $CO_2$ | 42.5(6) | 42.5(5) | 180.8(6) | −8.666(6) | 52.8(7) | 52.9(7) | 306.4(8) | −6.016(5) |
| $H_2O$ | 65(1) | 65.3(8) | 963(4) | −43.66(1) | 63.9(9) | 64(1) | 957(4) | −44.25(2) |

Fig. 6.3b shows the obtained profiles if the molecules of the fluid are assumed in each case to interact with the wall through the 10-4-3 Steele potential. The structure of the fluid in the pore is different now, and the different adsorbed layers induced by the attractive term of the wall potential are shown. Under these conditions, the carbon dioxide molecule is the one that presents the larger adsorption peak, and the layering effect extends for this molecule to the third fluid layer. The capillarity effect is also clear in this case. The interfacial tension computed now is remarkably much higher than the one obtained for the hard wall case for the molecules of methane and carbon dioxide,

but this effect is almost irrelevant in the case of water. This effect of the confining wall potential on the interfacial tension is connected with the average internal energy for each molecule. While the values are low for methane and carbon dioxide, as shown in Table 5.2, and the presence of the wall produces a remarkable energetic contribution, for the case of water the strength of the hydrogen bonds produces much higher internal energy values, and thus the interacting wall contribution is less relevant a produces an almost negligible contribution to interfacial tension values.

Figs. 5.4a and 5.4b show the same density profiles, now computed for pores twice wider than in the previous case, i. e., with $L_z = 24\sigma_{LJ}$. The influence of the slab width on interfacial tension is also to be highlighted, and the variation on the interfacial tension values is more relevant in this case for the interacting wall case. For the hard wall case, the influence of pore width in both interfacial tension and average internal energy is not noticeable. On the other hand, for the case of the interacting wall, the interfacial tension values increase in the case of methane and carbon dioxide, while they remain almost constant in the case of water, because the relative weight of the influence of the interaction energy of the walls is less relevant if compared with the other two molecules.

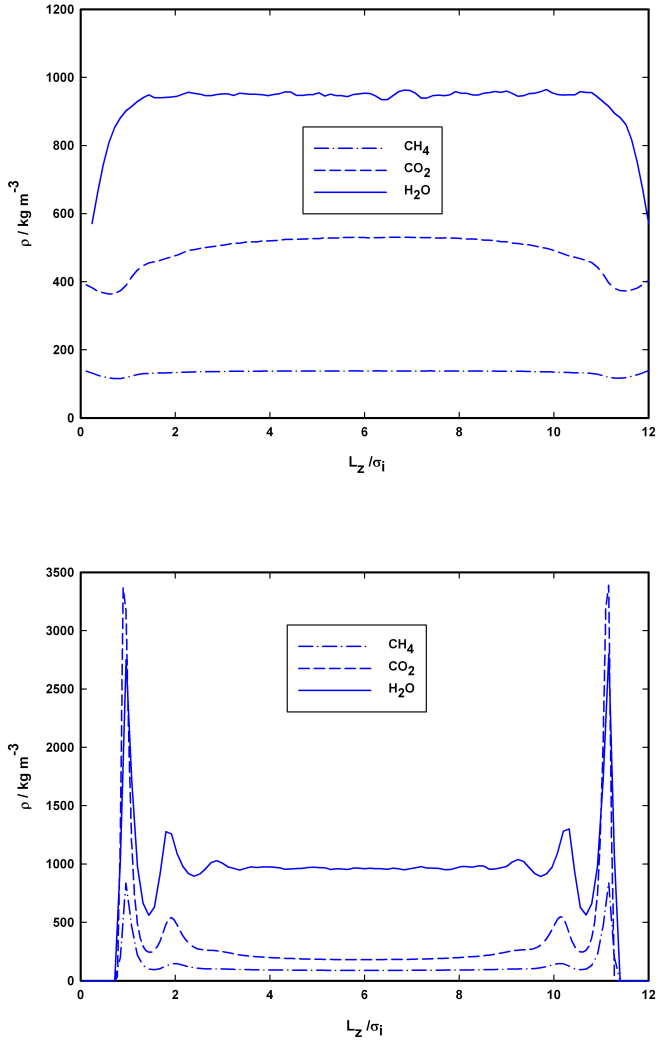


Figure 5.3: Density profiles for a slit pore ($L_z = 12\sigma_i$) at T=413.15 K and P=30 MPa containing TIP4P/2005 water (solid line), IMP $CO_2$ (broken line), and methane (dash-dot line): (a) Non interacting wall, (b) 10-4-3 Steele interacting potential wall.

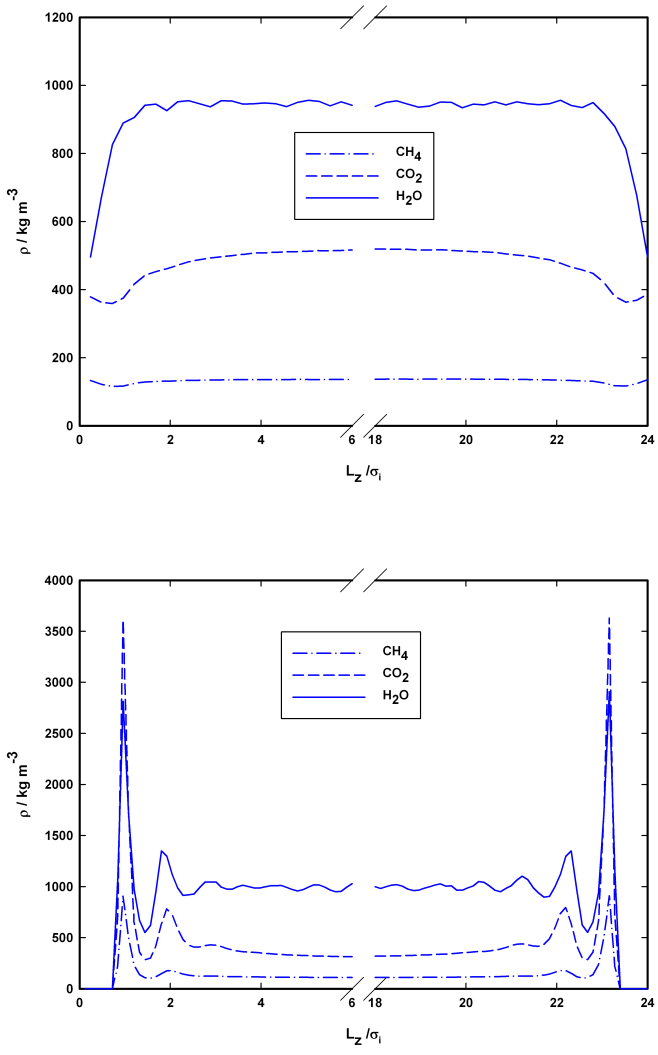


Figure 5.4: Same legend as Fig. 5.3, for a slit pore width $L_z = 24\sigma_i$.

## 5.5 Conclusions

In this work, the interfacial properties of methane, carbon dioxide and water under slab confinement have been determined using molecular simulation (Monte Carlo), for the configuration of slab confinement. Two different interaction schemes were considered for the interaction between the walls and the fluid molecules, namely a completely hard wall and an interacting wall described for the Steele potential. The calculations were done at a temperature and pressure values selected for being in the range of conditions presumably found in real Tight Gas Reservoirs. The computed results show that there is a clear influence on the pore width on the interfacial tension in the case of adsorbing walls for methane and carbon dioxide, while the nature of the strong association interaction between water molecules produces that this effect is less noticeable in this case. Further studies concerning the behaviour of fully miscible solutions of these compounds under confinement are necessary to contribute to characterize from a theoretical point of view the interfacial behaviour of real reservoir fluids, but these preliminary calculations on pure fluid interfacial properties evidence the need of a precise characterization of pore size distributions in the case of real adsorbing substrates.

# Chapter 6

# An examination of the ternary methane + carbon dioxide + water phase diagram using the SAFT-VR approach

## 6.1 Abstract

In this work, the molecular based Variable Range Statistical Associating Fluid Theory (SAFT-VR) has been used to estimate the global phase equilibria diagram of the ternary mixture water + carbon dioxide + methane, over a wide pressure and temperature range. An accurate determination of the phase equilibria of this mixture is relevant in Petrophysics, as for instance in enhanced natural gas recovery from low permeability reservoirs (the so called tight gas reservoirs), or in geology, as it is the basic composition of many geological fluids. A previous study on the phase behaviour of the binary mixtures involved is presented, using in a transferable manner the characteristic molecular parameters for the three molecules involved. The ternary mixture presents a very rich and complex phase behaviour, with a wide region of the thermodynamic space of phases (at higher pressures) presenting a large gap of ternary liquid−liquid equilibria, that upon descending on pressures leads to the transition to a three phase liquid− liquid−vapour equilibria region, and both regions are separated by a continuous critical endpoint line. The ability of the theory to describe this complex multicomponent mixture phase transition with a reduced and physically sound set of characteristic parameters must be underlined.

## 6.2 Introduction

Natural gas extraction from the so-called non conventional sources is gaining a remarkable relevance due to the increasing global demand of gas supply. These alternative sources include gas hydrates, coalbed methane, shale gas, and the tight-gas reservoirs (TGRs)[198,199]. TGRs are low permeability reservoirs, where the usual extraction techniques produce low gas yields. The global amount of natural gas that has been located trapped in this type of reservoirs undoubtedly points to TGRs as one of the main natural gas sources in the near future. Nevertheless, the optimal fracturation and extraction method for these reservoirs has not been determined yet, and it constitutes a challenging topic in Petrophysics. One of the key points in the extraction process commonly employed is the injection of an external aqueous based fluid, with the aim to modify the natural gas adsorption on the solid substrate, enhancing fluid recovery. Apart from the macroscopic engineering concerns, the interfacial phenomena occurring at molecular level in this scenario are poorly understood despite their important role in the process. Interfacial properties and fluid-substrate interaction at this scale determine the behaviour of the transport properties of the fluid, and contributions in this field are essential in order to gain insight into the involved phenomena. In particular, the modification of the original fluid-substrate reservoir conditions after the injection of the external fluid needs to be precisely described.

But before considering the effects induced by the presence of a solid substrate on a fluid mixture, it is essential to have, as starting reference, an accurate quantitative description of its global phase equilibria in bulk conditions, at temperature and pressure ranges close to those that are pressumed to be found in real reservoirs. This picture of the bulk system phase equilibria scheme is an essential information to guess which among the possible interfacial scenarios are bound to occur, and how the concentration, for instance, will modify the mixture behaviour to improve extraction conditions. Thus, the preliminary study of thermodynamic properties for bulk multicomponent mixtures that include methane, water, and other polar compounds plays a central role in this context. As an example, the importance of the water + methane binary mixture in the characterization of aqueous fluid inclusions in petroleum basins may be cited[200]. Carbon dioxide is a molecule that may be considered as well in the composition of these geochemically relevant mixtures, because its geologic sequestration is envisaged as a potential derived benefit of the extraction processes. In fact, a combination of carbon dioxide and water is already pumped into depleted oil wells to re-pressurize them and enhance oil recovery. Another application involving carbon dioxide, water and methane is the injection of $CO_2$ into deep sea methane hydrate reservoirs, with the double objective of releasing methane and capturing carbon dioxide in the hydrate structure[201]. Due to the complexity of the phase behaviour that may occur when considering multicomponent fluid mixtures, the selection of a physically

sound and versatile theoretical model, with demonstrated predictive ability for the estimation of complex phase equilibria diagrams plays a central role in the process.

In this paper, the objective is to estimate the ternary phase equilibria diagram of the water + carbon dioxide+ methane mixture, over the whole composition range, and in pressure and temperature ranges close to those that are supposed to exist in TGRs. The model used for this study is the Variable Range Statistical Associating Fluid molecular equation of state (SAFT-VR EoS[59,202]).

In previous works[203,204], the same approach has been used to accurately determine the water + carbon dioxide binary mixture phase diagram, using the intermolecular interaction parameters determined by Galindo and Blas[205,206] and Clark *et al.*[207]. This binary mixture exhibits type *III* phase behaviour, according to the classification of Scott and van Konynenburg[208,209], and due to its practical relevance, a large number of papers has been devoted to determine experimentally their phase equilibria, with special focus on the mutual solubilities. It is beyond the scope of this paper to present an exhaustive review of experimental data, but the paper of Spycher *et al.*[210] may be cited as an example, because it considers the pressure and temperature ranges of interest involved in carbon dioxide sequestration. Valtz *et al.*[19] determined experimentally vapour liquid equilibria for this binary, using SAFT-VR EoS as estimation tool. Other authors have tried different theoretical approaches

to estimate the phase equilibria of this mixture. As recent examples, Pappa *et al.*[211] have modelled the VLE of this mixture using a cubic EoS (Peng-Robinson), and Sun and Dubessy[212] considered a SAFT Lennard-Jones EoS version that included additional dipolar and quadrupolar terms to describe the intermolecular interactions. Recently, Lafitte *et al.*[131] used the so called SAFT VR Mie[213] approach to describe the VLE of this mixture, and used this calculation as starting point, coupling it to an inhomogeneous media theory (Gradient Theory) to describe the fluid-fluid interfacial phenomena, including wetting and adsorption, ocurring for this binary mixture. This latter application emphasizes the need of an accurate thermodynamic model describing both phase equilibria and thermophysical properties of the studied mixture, as a tool to further studies concerning, for instance, interfacial phenomena, which play a crucial role for the practical applications envisaged. From another perspective, Kontogeorgis et al./citeBreilFPE2011 have recently used the CPA EoS to analyze the behaviour of this binary, among other associating systems, with the objective to discuss several formulations describing the effect of crossed interactions between molecules and a feasible way to relate characteristic molecular parameters through an homomorph approach.

The binary mixture water + methane exhibits as well type *III* phase behaviour, as described in the review of the phase equilibria of the series of water + *n*-alkane mixtures presented by Galindo *et al.*[214], and finally the mixture carbon dioxide + methane presents type *I* behaviour[26,206]. The ref-

erences gathered in the cited articles show the extensive experimental and theoretical studies carried out for these three binary mixtures, but the ternary system has received much less attention due to the complexity of its phase diagram, that will be illustrated by the results shown in the present work. The scarce experimental works concerning this ternary mixture phase equilibria[29,215,216] are mainly focused on solubilities and VLE. Seo and Lee[217] determined experimental phase equilibria considering the presence of solid hydrates. From a modelling perspective, Duan et al.[218] presented an EoS for the ternary mixture based on the virial expansion, for an extended temperature and pressure range, justifying the study on the presence and relevance of this ternary mixture in many geological fluids. Austegard et al.[219] considered also this ternary mixture, focusing on the estimation of mutual solubilities of water in carbon dioxide and water in solutions of methane and carbon dioxide. For these purpose the authors used several cubic EoS approaches, as Soave-Redlich-Kwong[220] with different combining rules and the so-called Cubic Plus Association (CPA[221]) EoS. This paper tests various parametrization schemes and discusses the influence of the combining rules selected on the correlation of the experimental data.

## 6.3 Molecular model and theory

In the SAFT-VR approach, molecules are modelled with a simple united atom approach as chains composed of $m$ tangentially bonded segments of equal diameter $\sigma$, which interact through a potential of variable range, typically the square-well (SW) potential. The interactions in the SW potential between segments $i$ and $j$ separated by a distance $r_{ij}$ is given by,

$$u_{ij}(r_{ij}) = \begin{cases} +\infty & \text{if } r_{ij} < \sigma_{ij} \\ -\epsilon_{ij} & \text{if } \sigma_{ij} \leq r_{ij} \leq \lambda_{ij}\sigma_{ij} \\ 0 & \text{if } r_{ij} > \lambda_{ij}\sigma_{ij} \end{cases} \tag{6.1}$$

where $\sigma_{ij}$ defines the contact distance between spheres, and $\lambda_{ij}$ and $\epsilon_{ij}$ are the range and depth of the potential well for the $i$-$j$ interaction, respectively.

In this work we are considering three types of molecules: water ($H_2O$), methane ($CH_4$) and carbon dioxide ($CO_2$). The model for $H_2O$ molecules is based of the four-site model proposed by Bol[222] and Nezbeda *et al.*[223], where each molecule is represented as a hard sphere of diameter $\sigma_{11}$, with four off-centre short-range attractive sites that mediate the hydrogen-bonding interactions. Two associating sites (of type H) represent the hydrogen atoms in the $H_2O$ molecule and the other two sites (of type O) represent the lone pairs of electrons of the oxygen, where only H$-$O site-site interactions are allowed, i.e. no H$-$H or O$-$O interactions are permitted. The associating

sites are located at a distance $r_{d_{11}}$ from the centre of the sphere and have a cut-off range of $r_{c_{11}}$, so that when the site-site distance is less than $r_{c_{11}}$ a hydrogen-bonding energy of interaction $\epsilon_{11}^{hb}$ is realised. We use the optimal intermolecular parameters for $H_2O$ previously determined by Clark *et al.*[207]. The $H_2O$ molecule is represented by an spherical segment of hard-sphere diameter $\sigma_{22}$, whose intermolecular parameters were determined in the work of Patel *et al.*[224]. The third molecule considered here, $CO_2$, is modelled as two tangentially bonded hard-sphere segments of equal diameter $\sigma_{33}$, with molecular parameters obtained from the work of Galindo and Blas[205,206]. It is important to mention that the polar and quadrupolar interactions of $H_2O$ and $CO_2$ are treated in an effective way via the dispersive interactions. Although, it is worth to mention that $CO_2-CO_2$ and $CO_2-H_2O$ association interactions have been discussed by previous authors, such as Ji *et al.*[225], who treated the quadropular moment of $CO_2$ and $H_2O$ molecules via association, and Valtz *et al.*[19], who has suggested that the unusual large interaction parameters they found for the $H_2O$ + $CO_2$ mixture is due to the lack of a cross-association scheme. However, Valtz *et al.* realised that when incorporating this kind of unlike interactions the bonding energy values obtained were close to zero and as such they rejected the idea. Therefore, we have considered both $CH_4$ and $CO_2$ to be non-associating molecules and thus no unlike association was considered.

We examine the phase equilibria of the $H_2O + CH_4 + CO_2$ ternary system

using the SAFT-VR approach. Since this theory has already been presented and used previously,[59,202] here we only give an brief overview of the main expressions. As any other SAFT version, the SAFT-VR approach is written in terms of the Helmholtz free energy, which can be expressed as a sum of four microscopic contributions: an ideal contribution ($A^{IDEAL}$), a monomer term ($A^{MONO}$) that takes into account the attractive and repulsive forces between the segments that form the molecules, a chain contribution ($A^{CHAIN}$) that accounts for the connectivity of segments within the molecules, and an association contribution ($A^{ASSOC}$) that accounts for the hydrogen bonding interactions between molecules. Then, the Helmholtz free energy is written as,

$$\frac{A}{Nk_BT} = \frac{A^{IDEAL}}{Nk_BT} + \frac{A^{MONO}}{Nk_BT} + \frac{A^{CHAIN}}{Nk_BT} + \frac{A^{ASSOC}}{Nk_BT} \tag{6.2}$$

where $N$ is the total number of molecules, $T$ is the temperature, and $k_B$ is the Boltzmann constant.

The Helmholtz free energy of an ideal mixture of $n$ components is given by[226],

$$\frac{A^{IDEAL}}{Nk_BT} = \sum_{i=1}^{n} x_i \ln \rho_i \Lambda_i^3 - 1 \tag{6.3}$$

where $\rho_i = \frac{N_i}{V}$ represents the molecular number density of component $i$, $N_i$, $x_i$, and $\Lambda_i$ are the number of molecules, the molar fraction, and the thermal de Broglie wavelength of species $i$, respectively; and $V$ is the volume of the system.

The monomer free energy is given by a second-order high-temperature expansion of Barker and Henderson perturbation theory for mixtures[227–229],

$$\frac{A^{MONO}}{Nk_BT} = \frac{A^{HS}}{Nk_BT} + \frac{A_1}{Nk_BT} + \frac{A_2}{Nk_BT} \tag{6.4}$$

where $\frac{A^{HS}}{Nk_BT}$ is the free energy of reference hard-sphere mixture, which is obtained from the expression of Boublik[230] (equivalent to that of Mansoori *et al.*[231]); while $\frac{A_1}{Nk_BT}$ and $\frac{A_2}{Nk_BT}$ are the first- and second-order perturbation terms associated with the attractive interactions $u_{ij}(r_{ij})$ given by Eq. 7.1, where the former is treated in the context of the M1Xb mixing rule[59,202] and the latter is obtained using the local compressibility approximation.

The contribution to the free energy due to chain formation of square-well segments for a mixture of chains is given by[232],

$$\frac{A^{CHAIN}}{Nk_BT} = -\sum_{i=1}^{n} x_i \left(m_i - 1\right) \ln y_{ii}^{SW}(\sigma_{ii}) \tag{6.5}$$

where $m_i$ is the number of segments of component $i$, and $y_{ii}^{SW}(\sigma_{ii})$ is the background correlation function , $y_{ii}^{SW}(\sigma_{ii}) = g_{ii}^{SW}(\sigma_{ii}) \exp\left(-\beta\epsilon_{ii}\right)$, which is given in terms of the contact pair radial distribution function for a mixture of square-well segments corresponding to the $i-i$ interaction. $g_{ii}^{SW}(\sigma_{ii})$ is obtained from a first-order high-temperature expansion[227–229] (see references[59,202] for further details). Note that in our system, the only chain formation to account for in the free energy is due to the $CO_2$ chain model molecule, since both $H_2O$ and

$CH_4$ are modelled as spherical segments.

Finally, the contribution to the free energy due to the association of $s_i$ sites on a molecule of species $i$ can be obtained from the theory of Wertheim[233–236] as,

$$\frac{A^{ASSOC}}{Nk_BT} = \sum_{i=1}^{n} x_i \left[ \sum_{a=1}^{s_i} \left( \ln X_{a,i} - \frac{X_{a,i}}{2} \right) + \frac{s_i}{2} \right] \tag{6.6}$$

where the first sum is over component $i$ and the second over all $s_i$ sites of type $a$ on a molecule $i$. The fraction $X_{a,i}$ of molecules $i$ not bonded at site $a$ is given by the mass action equation as[237,238]:

$$X_{a,i} = \frac{1}{1 + \rho \sum_{j=1}^{n} x_j \sum_{b=1}^{s_j} X_{b,j} \Delta_{a,b,i,j}} \tag{6.7}$$

Here, $\Delta_{a,b,i,j}$ characterises the association between site $a$ on molecule $i$ and site $b$ on molecule $j$ and can be written as the following:

$$\Delta_{a,b,i,j} = K_{a,b,i,j} f_{a,b,i,j} g_{ij}^{SW}(\sigma_{ij}) \tag{6.8}$$

where the Mayer $f$-function of the $a-b$ site-site association interaction ($\phi_{a,b,i,j}$) is given by $f_{a,b,i,j} = \exp(-\frac{\phi_{a,b,i,j}}{k_BT}) - 1$, and $K_{a,b,i,j}$ is the available volume for bonding, whose expression can be found elsewhere[59,202,237,238]. Since there is only one associating component in the mixture (i.e. the $H_2O$ molecule) that is only allowed to form one type of hydrogen bond (i.e. $H-O$), with no unlike

association interactions between $H_2O-CO_2$ and $H_2O-CH_4$, the association contribution can be greatly simplified, and the fractions $X_{a,i}$ of $H_2O$ molecules not bonded at any of the four sites are equivalent.

The study of phase equilibria in mixtures also requires the determination of a number of cross interaction parameters, which account for the interactions between unlike components in the mixture. The Lorentz arithmetic mean is used for the unlike hard-core diameter,

$$\sigma_{ij} = \frac{\sigma_{ii} + \sigma_{jj}}{2} \tag{6.9}$$

and the unlike square-well potential range parameter is given by,

$$\lambda_{ij} = \frac{\lambda_{ii}\sigma_{ii} + \lambda_{jj}\sigma_{jj}}{\sigma_{ii} + \sigma_{jj}} \tag{6.10}$$

The unlike square-well dispersive energy parameter is given by a modified Berthelot rule as,

$$\epsilon_{ij} = \xi_{ij}\sqrt{\epsilon_{ii}\epsilon_{jj}} \tag{6.11}$$

where $\xi_{ij}$ describes the departure of the system from the geometric mean; it is usually determined by comparison with mixture data and then used to predict properties at different conditions.

Other thermodynamic properties, such as the chemical potential ($\mu$), compressibility factor ($Z$), and other thermodynamic derivatives needed in our

calculations can be easily obtained from the Helmholtz free energy using standard thermodynamic relations.

## 6.4 Results and discussion

The SAFT-VR approach requires the determination of a number of intermolecular parameters to describe the thermodynamic properties of real substances. For the non-associating $CH_4$ and $CO_2$ molecules, four parameters are needed to characterise the model, namely the chain length ($m_i$), the hard-core diameter of the segments ($\sigma_{ii}$), the depth ($\epsilon_{ii}$) and range ($\lambda_{ii}$) of the SW potential. In the case of $H_2O$ (associating), apart from the $m_1$, $\sigma_{11}$, $\epsilon_{11}$ and $\lambda_{11}$ set of parameters, additional parameters are necessary to describe the hydrogen bonding interactions such as the number and type of associating sites, the site-site energy parameter ($\epsilon^{hb}_{11}$) and the volume available for bonding ($K^{hb}_{11}$, which is given in terms of $r_{c_{11}}$, $r_{d_{11}}$ and $\sigma_{11}$ [239]). These parameters are usually obtained by fitting the theory to the experimental values of the vapour pressure and saturated liquid densities. In this work, we use the set of parameters obtained previously in the work of Clark *et al.*[207] for $H_2O$, Patel *et al.*[224] for $CH_4$ and work of Galindo and Blas[205,206] for $CO_2$, as reported in Table 8.1. This set of parameters has been shown to provide an excellent description of the phase behaviour at a wide range of temperatures, except the area near the critical point. It is known that SAFT, as any other classical

equation of state or mean field approach, does not consider the density fluctuations that occur near the critical point and hence the correct physics of the problem is not described and an over-prediction of its coordinates is expected. This can be easily addressed in an effective way by re-scaling the conformal parameters ($\sigma_c$ and $\epsilon_c$) to the experimental critical temperature and pressure. The re-scaled parameters are also presented in Table 8.1. The remaining, non-conformal parameters, are kept fixed in reduced units, but their corresponding values in real units are also presented in the table for clarity. It is obvious that use of the rescaled parameters produces a detriment in the calculated saturated liquid density of pure components, as it has been shown in previous works[205–207]. However, these sets of parameters provide a good description of the coexistence compositions and critical curves. A more satisfactory description of these systems could be obtained using the new version of SAFT-VR proposed by Forte *et al.*[240] in combination with the renormalization-group theory.

A summary of the results obtained for the three binary mixtures involved will be presented before discussing the phase equilibria diagram obtained for the ternary mixture. As mentioned before, the two binaries containing water exhibit type *III* phase behaviour. The most representative feature of this type of mixtures is that, in a PT projection of the phase diagram, the gas-liquid critical line is discontinuous and presents two branches. One of them, starting at the critical point of the less volatile compound, moves towards higher

Table 6.1: Optimised and Rescaled Square-Well Intermolecular Potential Parameters for Water[207], Methane[224] and Carbon Dioxide[205,206]

| $Molecule$ | $Water$ | $Methane$ | $CO_2$ |
|---|---|---|---|
| $m$ | 1 | 1 | 2 |
| $\sigma$ (Å) | 3.033 | 3.6847 | 2.7864 |
| $\epsilon/k_B$ (K) | 300.4330 | 167.3 | 179.27 |
| $\lambda$ | 1.718250 | 1.4479 | 1.515727 |
| $\epsilon^{HB}/k_B$ (K) | 1336.951 | | |
| $K^{HB}$ (Å$^3$) | 0.893687 | | |
| $\sigma_c$ (Å) | 3.469657 | 4.05805 | 3.136386 |
| $\epsilon_c/k_B$ (K) | 276.2362 | 156.464 | 168.8419 |
| $\epsilon_c^{HB}/k_B$ (K) | 1229.273 | | |
| $K_c^{HB}$ (Å$^3$) | 1.337913 | | |

pressures with negative slope, goes through a temperature minimum, and then continues with positive slope reaching temperatures higher than the one corresponding to the initial critical point. Due to the occurrence of this temperature minimum, this particular case of type *III* is also denoted as type*IIIm*, or alternatively it is referred to as well as type*IIIb* . The existence of phase equilibria beyond the critical temperature of the heaviest compound is characteristic of this type of systems only, and is commonly referred to as gas-gas inmiscibility of second kind, although the densities of the coexisting phases in the higher pressure and temperature ranges are typically liquid like. The other branch of the gas-liquid critical line starts at the lightest compound critical point, and it is very short, ending at a upper critical end point (UCEP), meeting there a three phase (liquid-liquid-vapour) equilibrium line coming from the

low temperature and pressure region. This global behaviour means that there is a continuous transition from liquid-vapour to a wide region of liquid-liquid equilibria for the mixture, which added to the temperature minimum of the high pressure critical line and the three phase line constitutes a remarkably complex scenario representing a demanding challenge for any EoS. This type of phase behaviour is typical of mixtures with a large degree of inmiscibility between the pure compounds.

### 6.4.1 $H_2O$ + $CO_2$ binary mixture

For the $H_2O + CO_2$ binary, the calculations performed in this paper repeated the scheme proposed in earlier works[203,204], so only a brief description wil be presented here. Fig. 6.1 recalls the estimated PT phase diagram, exhibiting the distinctive features described above, and let us just recall that a single binary unlike dispersive energy parameter ($\xi_{12} = 0,9742$), was fitted to improve the description of the experimental temperature minimum of the high temperature branch of the fluid-fluid critical line. This model represents adequately the whole phase diagram, with a satisfactory quantitative agreement with experimental literature data. Fig. 6.1 plots available vapour pressure experimental data for pure water[2–10] and $CO_2$[11–16], as well as data on the high pressure branch of the liquid vapour critical line[17,18] and three phase line[19], showing remarkable quantitative agreement in all cases.

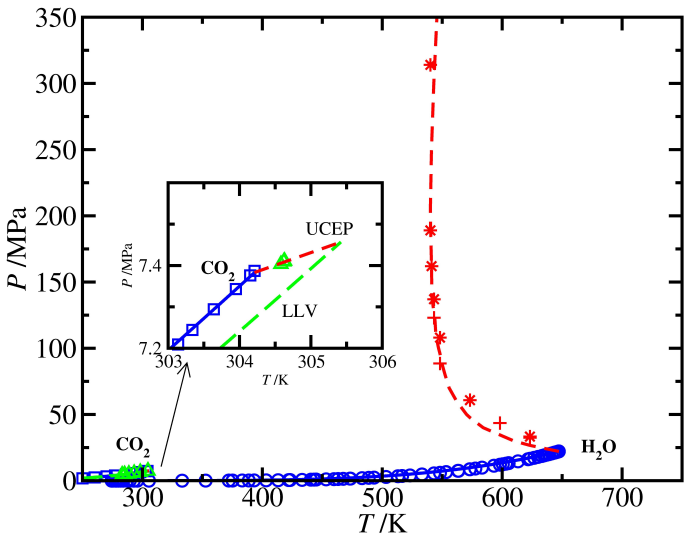


Figure 6.1: $PT$ projection of the phase diagram for the water(1) + carbon dioxide(2) binary mixture. The circles correspond to the experimental vapour pressure data of pure water[2–10], the squares to the experimental vapour pressure of pure carbon dioxide[11–16], the stars[17] and pluses[18] to the experimental gas-liquid critical line, and the triangles to the three-phase line[19]. The continuous curves are the SAFT-VR predictions for the vapour-pressures, the dashed curves for the critical lines and the long-dashed curve for the LLV three-phase line. The inset shows the region close to the critical point of pure $CO_2$.

### 6.4.2 $H_2O$ + $CH_4$ binary mixture

The $H_2O$ + $CH_4$ mixture behaviour is similar to the previous case, as noted. A comprehensive review of the global phase equilibria of the water + $n$-alkane mixtures series has been presented by Galindo *et al.*[214]. For this homologous series, the influence of the strong hydrogen bonding between water

molecules is one of the main causes that results in type III behaviour, up to *n*-eicosane. Nevertheless, it is necessary to keep in mind that, strictly speaking, the $H_2O + CH_4$ mixture can not be regarded as the first member of this family, due to the particularities exhibited by $CH_4$ if compared with other linear alkanes, as for instance its anomalous critical pressure[241]. For this reason, this binary mixture deserves an individual detailed study and parameters obtained from other mixtures of the same family do not yield accurate estimations if they are applied in a transferable manner to this particular solution. In this case, the computed PT phase diagram is presented in Fig. 6.2. Experimental data[21–24] of the temperature minimum of the high pressure branch of the LV critical line have been plotted also in this figure, showing good agreement with the SAFT estimated curve. The inset of the figure represents the Tx projection of this branch of the critical line, and this view of the estimated curve shows a shift of the calculated minimum towards higher water content compositions. Despite this displacement, it must be recalled here that for the calculations presented here, no binary mixing rule parameter was determined, and the results shown arise directly from the use of the pure component characteristic parameters listed in Table 8.1. The reason why in this case this $\xi_{12}$ parameter is not necessary may be connected with the fact that methane is a non polar molecule, so the representation of the molecule as a single sphere interacting through a square well potential is rather realistic, while on the other hand the use of two tangent spheres for carbon dioxide appears not to suffice, as its

quadrupolar nature is not explicitly accounted for, and this entails the need of a correcting factor to improve the representation of the mixture behaviour. In this case, the magnification of the region close to the $CH_4$ critical point has not been shown as an inset in the Figure, as we did in the case of the precedent binary mixture, because the LLV three pase line is virtually superposed to the pure compound saturation curve, so this representation would be worthless here.

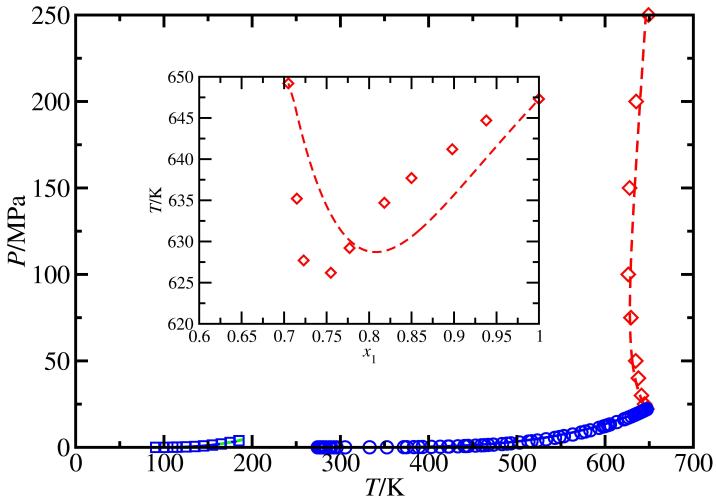


Figure 6.2: $PT$ projection of the phase diagrama for the water(1) + methane(2) binary mixture. The circles to the experimental vapour pressure data of pure water[2–10], the squares to the experimental vapour pressure of pure methane[20], and the diamonds[21–24] to the experimental gas-liquid critical line at high temperature. The continuous curves are the SAFT-VR predictions for the vapour-pressures, the dashed curves for the critical lines and the long-dashed curve for the LLV three-phase line. The inset shows the $Px$ projection of the gas-liquid critical line at high temperature of the mixture.

Fig.6.3a shows Px projections of the phase diagram, at temperatures ranging from 350 to 550 K, together with the experimental data of Fletcher *et al.*[25]. This range of temperatures lies above the UCEP, so no three phase equilibria appears, and below the temperature minimum of the high temperature branch of the liquid vapour critical line. The trend shown in this case by the coexistence envelope is the typical III phase equilibrium type transition from vapour liquid equilibrium at low pressures to liquid liquid equilibrium at high pressures. Fig.6.3b plots Tx projections of the phase diagram at pressures ranging from 5 to 100 MPa, showing the estimated high pressure liquid liquid equilibria of the system, together with the corresponding experimental points of the LV critical line for the higher pressures of this calculation (30, 50 and 100 MPa). The correspondence between these experimental points and the estimated high pressure LL coexistence curves is very good, and it must be taken into account that the range of pressures here is very far from the one where the pure compound experimental data used for characteristic parameter fitting were placed, ensuring a remarkable extrapolation ability for the theory over wide ranges of temperature and pressure, which is essential for the practical application that justifies this analysis.

### 6.4.3 $CH_4$ + $CO_2$ binary mixture

The $CH_4$ + $CO_2$ binary mixture exhibits type I behaviour, with a continuous liquid vapour critical line connecting both pure compounds critical

points, as shown in Fig.6.4. This critical locus presents a maximum, indicating large positive deviations from Raoult's law, a characteristic feature of binary mixtures presenting weak intermolecular interactions.

Fig. 6.5a shows the Px projection of the phase diagram, at temperatures ranging form 170 to 300 K, compared with the experimental data[27,28], and the experimental critical line. Finally, the Tx projection has been plotted in Fig. 6.5b, together with the experimental data of Donnelly and Katz[26]. In both cases the theory reproduces accurately the vapour liquid equilibria of the binary, without considering any crossed interaction characteristic parameter.

### 6.4.4 $H_2O$ + $CO_2$ + $CH_4$ ternary mixture

Once we have analyzed the phase behaviour of the three binary mixtures forming the $H_2O + CO_2 + CH_4$ ternary system, we have applied the SAFT-VR approach to obtain the phase behaviour of the ternary mixture at different thermodynamic conditions.

We first consider the phase behaviour of the mixture at similar conditions at which the system is found in tight-gas reservoirs. Fig. 6.6a and Fig. 6.6b show the triangular phase diagram of the mixture at 375.5 and 324.5K, and different pressures, respectively. At these thermodynamic conditions, the $CH_4$

+ $CO_2$ binary mixture exhibits a single fluid homogeneous phase (the critical point of $CH_4$ is located at 190.6 K and 4.61 MPa, and that corresponding to $CO_2$ at 304 K and 7.3 MPa. On the other hand, at 375.5 and 324.5 K and the pressures considered in Fig. 6.6a and Fig. 6.6b , the other two binary mixtures of the ternary system, i.e., $H_2O$ + $CO_2$ and $CH_4$ + $H_2O$, exhibit the characteristic LL immiscibility of type III phase behaviour.

The theoretical predictions obtained from the SAFT-VR approach are compared with experimental data taken from the literature at different thermodynamic conditions. As it is shown, the theory is able to provide an excellent description of the phase behaviour. It is important to recall here that the results presented in Fig. 6.6a and Fig. 6.6b are pure predictions, since no further fitting has been performed. As it has been already explained, we have fitted the unlike binary interaction parameters associated to the $H_2O$ + $CO_2$ dispersive interactions to experimental data taken from literature. Apart from that, no further experimental information from the ternary system has been used in the calculations presented in this work.

From the point of the phase envelopes of the binary mixtures involved it is easy to understant the phase diagrams shown in Fig. 6.6a and Fig. 6.6b, where the system exhibits large two-phase LL immiscibility regions. As previously mentioned, the $CH_4$ + $CO_2$ binary mixture is completely miscible at these thermodynamic conditions, and this explains why the coexistence envelopes do not cut the $CH_4$ - $CO_2$ axis of Fig. 6.6a and Fig. 6.6b. At $x_{CH_4} \approx 0$, which

corresponds to a nearly pure $H_2O + CO_2$ binary system, the mixture exhibits LL immiscibility between a water-rich liquid phase ($x_{H_2O} \approx 0.98$) and a carbon dioxide-rich liquid phase ($x_{CO_2} \approx 0.95$). As the composition of the methane is increased, the relative composition of $CO_2$ in the $CO_2$-rich liquid phase decreases (the composition of the water-rich liquid phase is nearly constant and only varies from $x_{H_2O} \approx 0.98$ in the $H_2O + CO_2$ binary system to $x_{H_2O} \approx 0.99$ in the $CH_4 + H_2O$ binary mixture, approximately) and changes continuously to a methane-rich liquid phase (with $x_{CH_4} \approx 0.95$ when $x_{CO_2} \approx 0$).

To explore in more detail the complex topology of the phase diagram of this ternary mixture, we have performed some additional calculations at different thermodynamic conditions, close to those at which the tight-gas reservoirs exist. We consider the effect of pressure on the phase behaviour of the system at the high-temperature region in Fig. 6.7a. Since the vapour pressure of pure water at 500 K is 3.4 MPa, the ternary mixture exhibits LL immiscibility at all the pressures considered here. It is important to remember that aqueous mixtures of carbon dioxide and methane exhibit type III phase behaviour, and consequently, the corresponding ternary diagram should present at least one region of two-phase LL separation.

Fig. 6.7a, shows the composition of one the liquid phases, i.e., the water-rich liquid phase, which is nearly constant as the pressure is reduced from 100 up to 5 MPa ($x_{H_2O} \approx 0.92$ at all the pressures). The composition of the other phase varies significantly as the pressure is decreased, from $x_{H_2O} \approx 0.2 - 0.3$ at

the highest pressures (20-100 MPa), up to $x_{H_2O} \approx 0.4-0.5$ and $x_{H_2O} \approx 0.7-0.8$ at 10 and 5 MPa, respectively. It is obvious from the ensuing discussion that the size of the LL immiscibility region should decrease as the pressure is lowered, an expected behaviour in systems including one associative compound ($H_2O$).

We have also considered the effect of the temperature, at constant pressure, on the phase behaviour of the ternary mixture. As can be seen in Fig. 6.7b, as the temperature is reduced from 500 up to 300 K approximately, the phase envelope corresponding to the water-poor liquid phase is shifted towards regions of lower compositions of $H_2O$, from $x_{H_2O} \approx 0.45$ up to $x_{H_2O} \approx 0.99$. This is a result of the increasing of the LL inmiscibility as the temperature decreases, as expected. On the contrary, the phase envelope corresponding to the water-rich liquid phase remains essentially at the same position in the triangular phase diagram as the temperature is decreased. This effect can be understood clearly from a molecular perspective: as the temperature decreases the association due to hydrogen bonding between water molecules increases, and as a consequence of this, the mutual solubility of water with carbon dioxide and methane decreases, resulting in larger LL immiscibility regions.

As we have seen in the previous figures, the phase behaviour of the system is dominated by relatively large LL immiscibility regions. The topology of the phase diagram at these thermodynamic conditions is characterized by a two-phase LL coexistence region, with one water-rich liquid phase and one water-

poor liquid phase (which can be $CO_2$-rich or $CH_4$-rich liquid phase depending on composition). The phase envelope associated to the $H_2O$-rich liquid phase (close to the pure water corner of the triangular diagram) connects the $CH_4$ – $H_2O$ and $H_2O$ – $CO_2$, whereas the other phase envelope, associated to the water-poor liquid phase (carbon dioxide- or methane-rich phase) connects the same axis in the opposite side of the phase diagram. In addition to the two-phase coexistence region, the phase diagram at high temperatures also exhibits a one-phase homogeneous region. As the temperature of the system decreases and/or the pressure is increased, the phase envelope associated to the $H_2O$-poor liquid phase approaches to the $CH_4$ – $CO_2$ axis, as it has been shown previously in Fig. 6.7a and Fig. 6.7b. As a consequence, the two-phase LL immiscibility region increases, as expected, and the one-phase homogeneous region becomes smaller.

As we have discussed previously, the topology of this phase diagram (at these conditions) is a consequence of the $H_2O$ – $CO_2$ and $H_2O$ – $CH_4$ immiscibility. However, the ultimate reason why a one-phase homogeneous phase exists in the phase diagram is due to the miscibility at all proportions of $CH_4$ and $CO_2$, i.e., the $CH_4$ + $CO_2$ mixture does not exhibit LL neither VL phase separation. But, what does it happen if the temperature of the system is decreased, at the appropriate pressure, so that we ensure that the thermodynamic state of the mixture is located inside the VL coexistence region of the $CH_4$ + $CO_2$ binary mixture?

Fig. 6.7c shows the triangular diagram of the $H_2O + CO_2 + CH_4$ ternary mixture at 275 K and 7.5 MPa. As it can be seen, the topology of the phase diagram is completely different than that shown in Fig. 6.7a and Fig. refs-fig:figure7c, since it displays one central LLV three-phase region, three LL two-phase coexistence regions (two LL zones and one VL region), and three monophasic homogenous phases. Fig. 6.8 shows a schematic diagram with the same topology than that exhibited by the mixture in Fig. 6.7c.

One of the two-phase regions can not be distinguished due to its proximity to the $CH_4 - CO_2$ axis of the diagram. The three one-phase homogenous regions, located near the vertexes of the triangular diagram, can not be seen neither due to the same reason, their very small size.

In the triangular central region two liquid phases coexist in equilibrium with a vapour phase. The compositions of each phase are defined by the coordinates of the central triangle in the phase diagram: the $H_2O$-rich liquid phase is composed by nearly pure $H_2O$ ($x_{H_2O} \approx 0.996$), with a liquid-like packing fraction $\eta_{L_1} \approx 0.49$, the second liquid phase is formed by a mixture of $CO_2$ ($x_{CO_2} \approx 0.778$) and $CH_4$ ($x_{CH_4} \approx 0.210$), with a liquid-like packing fraction $\eta_{L_2} \approx 0.22$, and the vapour phase, with a composition of $x_{CO_2} \approx 0.647$ and $x_{CH_4} \approx 0.351$), and a vapour-like packing fraction $\eta_V \approx 0.11$.

This behaviour can be explained from a molecular perspective: the $H_2O - CH_4$ and $H_2O - CO_2$ interactions are very unfavourable due to self-association between $H_2O$ molecules (these mixtures exhibit LL immiscibility).

At high temperatures and pressures, since the $CH_4$ + $CO_2$ mixture exhibits only a homogeneous liquid phase, the ternary system minimizes its free energy by segregating the system into a water-rich liquid phase, dominated by hydrogen bonding interactions, and a second water-poor liquid phase, dominated by the dispersive interactions. This second liquid phase changes its methane-rich to carbon dioxide-rich character according to the relative $H_2O$ − $CO_2$ and $H_2O$ − $CH_4$ affinity at the corresponding pressures and temperatures. However, at low temperatures and pressures, the $CH_4$ + $CO_2$ mixture exhibits VL phase separation. This region eventually interacts with the LL two-phase region dominated by hydrogen bonding, resulting in the new topology shown in Fig. 6.7c.

Due to the proximity of the LLV three-phase region to the triangular axis of the diagram it is difficult to distinguish clearly the exact location of the coexistence regions. Fig. 6.8 shows a schematic diagram with the same topology than that exhibited by the mixture presented in Fig. 6.7c. As can be seen, the system has a central three-phase coexistence region. Each of the sides of the triangular region connects three two-phase regions with the corresponding two-component coexistence axis, indicating that the three binary mixtures that form the ternary system exhibit two-phase separation at these thermodynamic conditions. In the particular case of the mixture shown in Fig. 6.7c, the $H_2O$ + $CO_2$ and + $CH_4$ binary mixtures exhibit LL separation and the last mixture ($CO_2$ + $CH_4$) presents VL coexistence at the particular

thermodynamic conditions.

As we have mentioned, the proximity of the three-phase region to the triangular axis of the phase diagram, which is a consequencie of the large LL immiscilibity regions exhibited by two of the three binary mixtures that form the system ($H_2O + CO_2$ and $+ CH_4$ binary mixtures) and the low mutual solubilities between water and carbon dioxide and methane, makes really difficult to see if the system really exhibits three-phase separation. We have included two additional figures that help to understand the phase behaviour exhibited by the same at the same thermodynamic conditions presented in Fig. 6.7c. Fig. 6.9 shows the carbon dioxide composition and the water composition *versus* the methane composition at the same conditions as those presented in Fig. 6.7c. As can be seen, the blue, red, and violet curves are the phase enveloped associated to the two-phase coexistence regions previously shown in the triangular diagram of Fig. 6.7c, which end at the vertex of the triangular region (red triangles in this figure) and at the three axis of the triangular diagram.

We have also analized the phase behaviour of the ternary mixture at low temperatures, with particular emphasis on the effect of temperature and pressure on the three-phase LLV immiscibility region. Fig. 6.10 shows the effect of pressure, at six different temperatures on the three-phase triangular region. The three two-phase regions and the three one-phase homogenous phases have not been displayed in these representations for the sake of clarity. However,

all the phases involved at each temperature and pressure shown in this figure are topologically equivalent to that of Fig. 6.8. As it can be seen in Fig. 6.10a, at 275 K, the LLV three-phase region decreases in size as the pressure is increased, as expected from the previous discussion. In particular, the two phases near the $CH_4 - CO_2$ axis of the phase diagram, i.e., the water-poor liquid phase and the $CO_2$-rich vapour phase, become more similar as the pressure is increased. At 8.60 MPa approximately, both phases become critical in the presence of the second (water-rich) liquid phase. At pressures above 8.60 MPa approximately, the system exhibits LL two-phase separation, as we have seen previously in Fig. 6.7b.

When the temperature is raised, the same qualitative behaviour is observed. However, the LLV three-phase region becomes smaller as temperature increases, as expected. At the lowest pressure (7.5 MPa), the triangular region of coexistence becomes narrower as the temperature is near 300 K. In addition, the range in pressures at which the LLV three-phase region is stable decreases as temperature increases. For instance, at 295 K, the pressure at which the three-phase coexistence vanishes is below 8 MPa, whereas at 300 K, the pressure value is equal to 7.66 MPa, which means that the range at which the three phases coexist is smaller than 0.2 MPa.

All the plots shown in Fig. 6.10 have a common feature: when the pressure is increased, the system exhibiting three phases in coexistence evolves to show two-phase equilibrium phase behaviour, or in other words, the system crosses

a critical endpoint. In binary mixtures (of fluids), a critical endpoint is the endpoint of a three-phase line in which two of the phases become critical in the presence of the third phase in coexistence. For instance, mixtures exhibiting LL immiscibility (types II, III, IV, V, and VI) have at least one critical endpoint (mixtures of type VI have two critical endpoints and mixtures of type IV have three). There exist two different natures of critical endpoints depending on the two phases that become critical: (1) critical endpoint of nature $L_1 = L_2 + V$, in which the two liquid phases are critical in the presence of a vapour phase; and (2) critical endpoint of nature $L_1 = V + L_2$, i.e., the liquid phase 1 and the vapour phase V are critical in the presence of the liquid phase 2. In particular, the second type of critical endpoint appears as an upper critical endpoint in mixtures that exhibit type III phase behaviour, as in the $H_2O + CO_2$ and $H_2O + CH_4$ binary mixtures studied in this work.

According to the rule phase, critical endpoints are states with zero degress of freedom, which means that they are fixed points in the corresponding phase diagram. However, in ternary mixtures, due to the presence of an additional component, the three-phase states lie on a surface (in the multidimensional thermodynamic phase space), instead of a line (as it occurs in binary mixtures), and consequently, the critical endpoint states are not longer fixed points in the phase diagram, but lie along a line, i.e., along critical endlines.

We have determined from SAFT-VR the upper critical endpoint temperatures and pressures, as function of the $CO_2$ mole fraction on a $H_2O$ free basis,

i.e., $x^*_{CO_2} = x_{CO_2}/(x_{CO_2} + x_{CH_4})$. As can be seen in Fig. 6.11 , a continuous critical endpoing locus (in the $Px^*$ and $Tx^*$ projections of the phase diagram) of nature $L_2 = V + L_1$ separates the three-phase surface $L_1L_2V$ (lower temperature part of the diagrams) from a two-phase region $L_1L_2$ (higher temperature part of the diagram). It should be noted that the limit $x^*_{CO_2} = 0$ represents the upper critical endpoint of the binary mixture $H_2O(1) + CH_4(2)$ and the limit $x^*_{CO_2} = 1$ the upper critical endpoint of the binary mixture $H_2O(1) + CO_2(2)$. In fact, this figure can be understood better in the context of pseudobinary mixtures, i.e., the $H_2O(1) + CH_4(2) + CO_2(3)$ ternary mixture can be viewed as a binary mixture of $H_2O$ and a second pseudocomponent, which is a mixture of $CO_2$ and $CH_4$ controlled by the mole fraction $x^*_{CO_2}$. Under this point of view, the upper critical endpoint of the $H_2O(1) + CH_4(2)$ real binary mixture, at $x^*_{CO_2} = 0$, 190.6 K, and 4.6 MPa, changes continuously to the second $H_2O(1) + CO_2(2)$ real binary mixture, at $x^*_{CO_2} = 1$, 305.4 K, and 7.46 MPa, as the mole fraction $x^*_{CO_2}$ is increased.

Finally, we have also considered the effect of temperature, at six different temperatures on the three-phase triangular region. As can be seen in Fig. 6.10 , the three-phase coexistence region decreases in size as the temperature rises. As the pressure varies from 6 up to 7.5 MPa, the same qualitative behaviour is observed, although the temperature at which the system passes from a three-phase to a two-phase behaviour increases. This trend is clearly reversed for the two highest pressures, 8 and 8.5 MPa. It should be noted that at pressure

6-7.5 MPa the system does not exhibits critical behaviour, i.e., the system passes from a three-phase to a two-phase region without crossing a critical endpoint, as can be seen clearly in Fig. 6.9b (close to the $x^*_{CO_2} \approx 0$ region). In other words, the critical endpoint pressures of the ternary mixture close to the $x^*_{CO_2} \approx 0$ region, or equivalently, close to the region of the upper critical endpoint of the $H_2O(1) + CO_2$ real binary mixture, are always higher than 7.5 MPa. As a consequence of this, at pressures below 7.5 MPa, the system passes from the $L_1L_2V$ three-phase region to the $L_1L_2$ surface without crossing a critical endpoint. This change of behaviour is due to the presence of the vapour pressure curve of pure $CO_2$ in this region: when the temperature of the system is decreased at the pressure is below $\sim 7.5 MPa$ (the critical pressure of $CO_2$ is 7.3 MPa approximately), the system crossed the vapour pressure curve of pure $CO_2$ and the ternary systems passes directly (not critically) from the three-phase to the two-phase region. Although this mechanism might seem peculiar, a similar scenario occurs in binary mixtures when the system crosses the vapour pressure curve of one of the components from the two-phase to the one-phase region.

## 6.5 Conclusions

The results described in the precedent section, that include a detailed description of the global phase behaviour of this ternary mixture are a proof

of the ability of the SAFT-VR EoS to describe remarkably complex phase equilibria using only a reduced number of molecular based characteristic parameters. It has been shown that, for the set of binary mixtures involved, only the $H_2O + CO_2$ one demanded the determination of an unlike interaction energy combining rule parameter, with the aim to improve the estimation of the minimum of the high temperature branch of the discontinuous LV critical line, a feature that is characteristic of its type III binary phase diagram. Nevertheless, the purely predictive results obtained for the other aqueous binary did not need any supplementary mixing parameter determination, and the calculations obtained from the pure component parameters yielded fairly good results if compared with experimental data. The same situation holds for the simpler type I $CH_4 + CO_2$ binary mixture.

Once these preliminary results on the constituent binary mixtures were obtained, it must be recalled that the rest of the phase equilibria calculations presented here were performed without fitting any supplementary parameter. This fact underlines the predictive power of SAFT-VR EoS when applied to the estimation of complex multicomponent phase equilibria landscapes, a matter of primary importance for applied purposes that has not received enough attention in the literature although it constitutes a demanding challenge for any thermodynamic model.

Our attention has then been focused on the pressure and temperature ranges of interest in the application that motivated this work, i. e., the ther-

modynamic conditions that are presumed to occur in tight gas reservoirs. The obtained phase equilibria behaviour for the ternary mixture is a result of the competition of the wide high pressure liquid liquid separation regions, typical of the binary aqueous mixtures, and the effect induced at lower pressures by the $CH_4 + CO_2$ liquid vapour critical curve. This combination of two type III and one type I binary mixtures led to the appearance of two clearly differenced regions. At pressures above the maximum of the $CH_4 + CO_2$ LV critical line, the ternary diagrams obtained show a wide region of LL equilibria, and an homogeneous phase close to the completely miscible (in these conditions) $CH_4 + CO_2$ mixture. This is a direct consequence of the well known high pressure LL equilibria obtained previously for both aqueous binaries. The boundaries of this LL separation region agrees well with the available experimental data, and the effect of temperature and pressure has been shown and rationalized according to the mutual interactions between the three molecules present.

This first scenario of phase behaviour for the ternary mixture changes abruptly in the temperature and pressure range where the $CH_4 + CO_2$ shows LV equilibria. In this range of conditions, the wide LL gap in the ternary diagram is transformed into a situation where a central three phase LLV equilibria region, three LL equilibria regions, and three tiny monophasic regions placed closer to each pure compound coexist. So, for these temperature and pressure combinations, a modification in the mixture composition can lead to one, two or three phases in equilibrium. The topology of this LLV three

phase equilibrium region has been then explored, by performing calculations at different temperature and pressure values. The aim now was to locate in every case the three phase to two phase equilibrium transition coordinates, this is, the critical endpoints for the ternary mixture, that, contrarily to what happens in binary mixtures, lie along a line connecting the upper critical endpoints of both aqueous binary mixtures. Thus, this ternary critical endpoint line, of nature $L_1 = V + L_2$, has been traced and its trend plotted against temperature and pressure. Nevertheless, this transition from ternary three phase to two phase equilibria in the mixture may occur as well directly (without crossing a critical endpoint), and the transition is produced crossing the saturation curve of one of the pure compounds, $CO_2$ in this case.

This final summary depicts a complex and rather unexpected phase behaviour for this ternary mixture, which emphasizes the need to handle versatile and robust theoretical models when any related practical application is envisaged. SAFT-VR has shown here again its suitability to reproduce the existing phase equilibria experimental data with remarkable accuracy, offering also estimations of the phase equilibria trend of the mixture over wide ranges of temperature and pressure. All this is obtained on a molecular basis, with transferable parameters that may be applied to estimate an additional large ensemble of thermodynamic or even interfacial properties if needed.

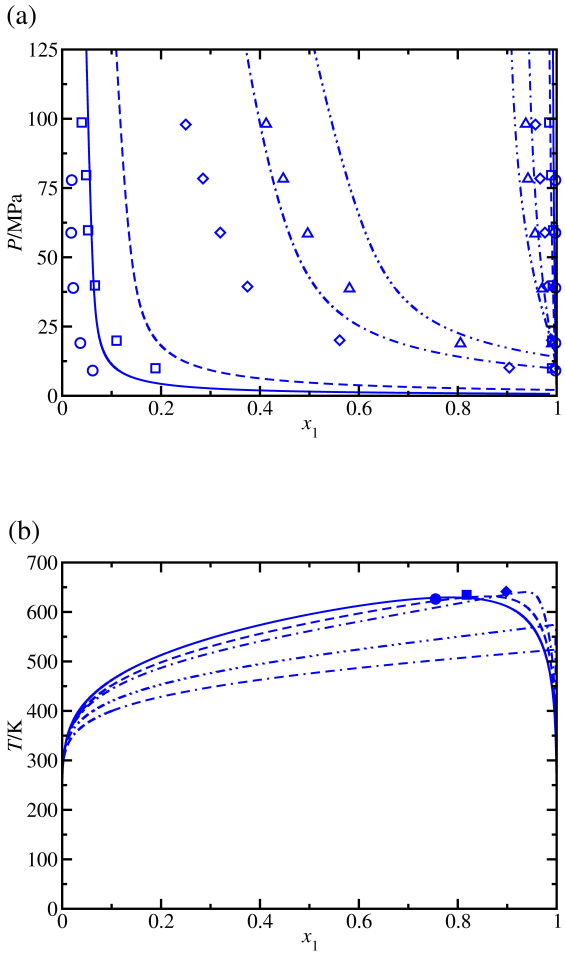


Figure 6.3: (a) $Px$ and (b) $Tx$ projection of the phase diagram for the water(1) + methane(2) binary mixture at different temperatures and pressures, respectively. The symbols correspond to the experimental data taken from the literature and the curves to the predictions obtained from SAFT-VR (a) at 423.15 K (circles[25] and continuous curves), 473.15 K (squares[25] and dashed curves), 573.15 K (diamonds[25] and dot-dashed curves), and 603.15 K (triangles[25] and dash-dash-dotted curves) and (b) at 100 MPa (circle[21–24] and continuous curve), 50 MPa (square[21–24] and dashed curve), 30 MPa (diamond[21–24] and dot-dashed curve), 10 MPa (dot-dot-dashed curve), and 5 MPa (dash-dash-dotted curve).

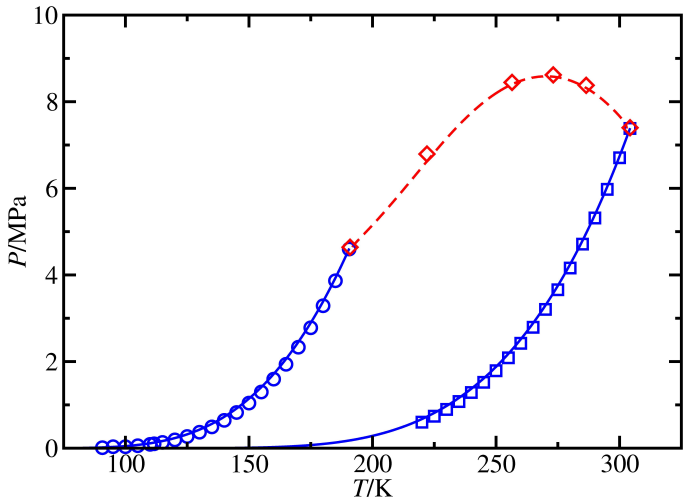


Figure 6.4: $PT$ projection of the phase diagram for the methane(1) + carbon dioxide(2) binary mixture. The circles correspond to the experimental vapour pressure data of pure methane[20], the squares to the experimental vapour pressure of pure carbon dioxide[11–16], and the diamonds[26] to the experimental gas-liquid critical line. The continuous curves are the SAFT-VR predictions for the vapour-pressures and the dashed curves for the gas-liquid critical line.

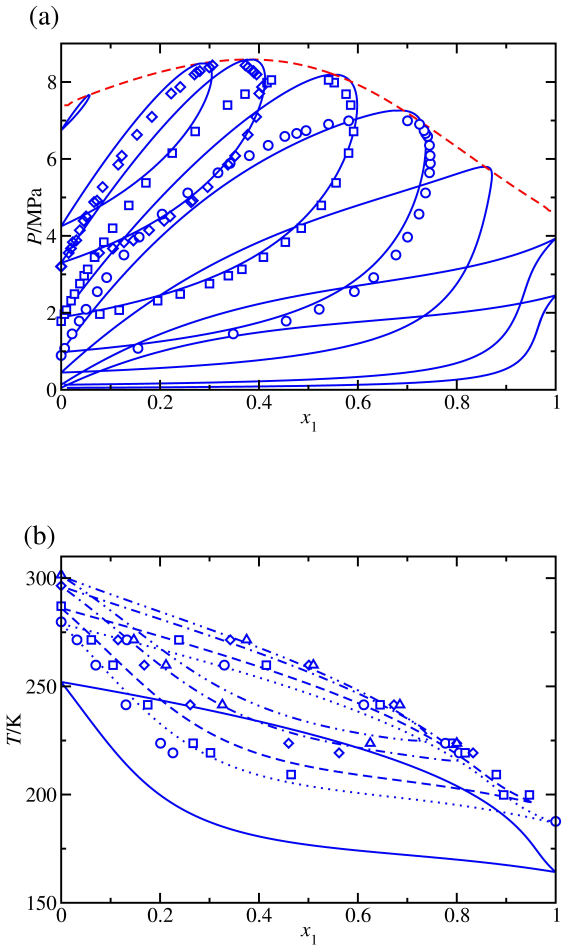


Figure 6.5: (a) $Px$ and (b) $Tx$ projections of the phase diagram for the methane(1) + carbon dioxide(2) binary mixture at different temperatures and pressures, respectively. The symbols correspond to the experimental data taken from the literature and the continuous curves to the predictions obtained from SAFT-VR: (a) at (from bottom to top) 170, 185, 210, 230 (circles[27]), 250 (squares[27]), 270 (diamonds[27,28]), and 300 K; (b) at 2 MPa (continuous curve), 4.137 MPa (circles[26] and dotted curve), 4.930 MPa (squares[26] and dashed curve), 6.206 MPa (diamonds[26] and dot-dashed curve), and 6.895 MPa (triangles[26] and dot-dot-dashed curve).

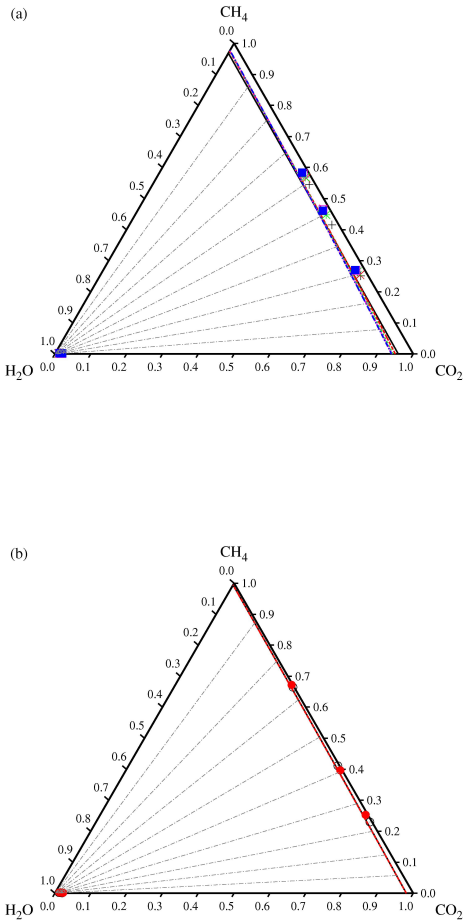


Figure 6.6: Ternary phase diagram of the mixture $H_2O(1)$ + $CO_2(2)$ + $CH_4(3)$ at different temperatures and pressures. The symbols correspond to the experimental data taken from the literature[29] and the curves to the predictions obtained from SAFT-VR at (a) 375.5 K and 10.5 MPa (pluses and continuous curves), 20.5 MPa (crosses and dashed curves), 30.3 MPa (stars and dotted curves), 40.2 MPa (open squares and dot-dashed curves), 50.0 MPa (filled square and dot-long dashed-dashed curves) and (b) 324.5 K and 30.5 MPa (open circles and continuous curves) and 50.0 MPa (filled circles and dashed curves).

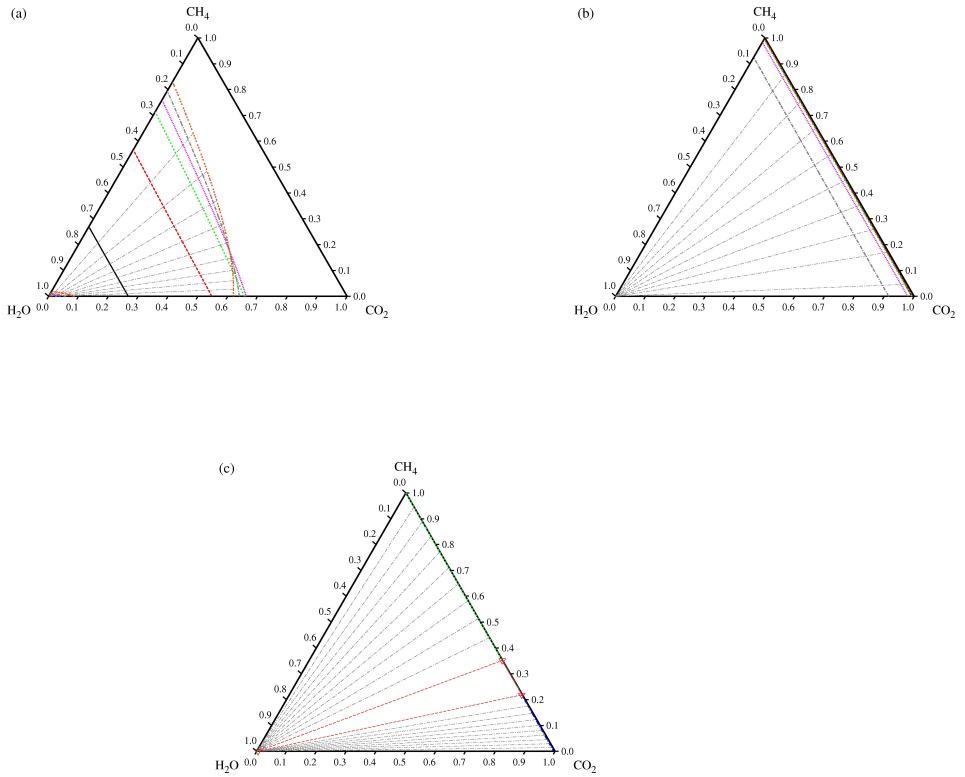


Figure 6.7: Ternary phase diagram of the mixture $H_2O(1)$ + $CO_2(2)$ + $CH_4(3)$ at different temperatures and pressures predictions obtained from SAFT-VR. (a) Two-phase liquid-liquid coexistence at 500 K and 5 MPa (continuous curves), 10 MPa (dashed curves), 20 MPa (dotted curves), 30 MPa (small-dotted curves), 50 MPa (dot-dashed curves), 100 MPa (tree-dot curves), and (b) two-phase liquid-liquid coexistence at 7.5 MPa and 300 K (continuous curves), 310 K (continuous curves), 320 K (continuous curves), 350 K (continuous curves), and 400 K (continuous curves), and (c) three-phase liquid-liquid-vapour coexistence at 7.5 MPa and 275 K. The dot-dashed lines in all parts of the figure correspond to the two-phase tie-lines at 100 MPa in (a), at 300 K in (b), and 275 K and 7.5 MPa in (c). The triangles correspond to the compositions of the three-phase liquid-liquid-vapour in coexistence in (c).

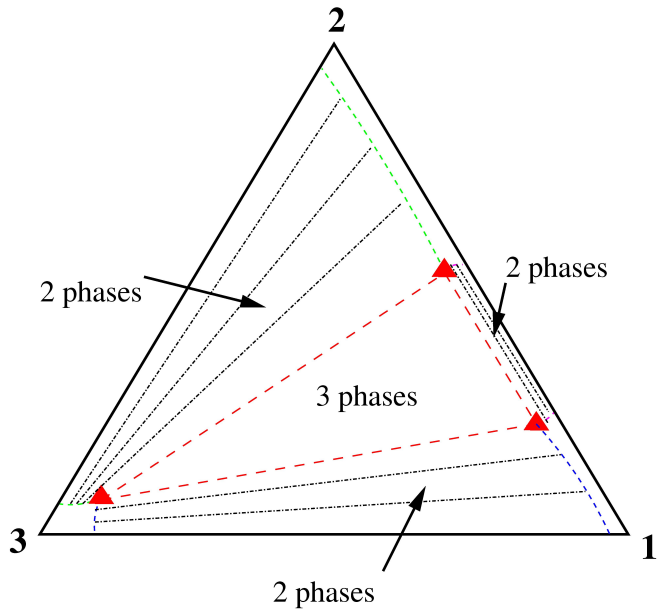


Figure 6.8: Schematic diagram of a hypotherical ternary mixture that exhibits three-phase separation (triangular region) and three two-phase regions associated to the binary mixtures 1-2, 2-3, and 1-3 of the ternary systems. The red triangules represent the compositions of the three phases in coexistence, the red dashed lines the boundaries of this region, and the blue, green, and violet dashed lines thecoexsitence envelopes of the two-phase regions of the diagram. The dot-dashed lines inside of thethree two-phase regions are the corresponding tie-lines. The zones located between the axis of the triangular diagram, the two-phase coexistence envelopes, and the three red triangles represent the one-phase regions of the phase diagram.

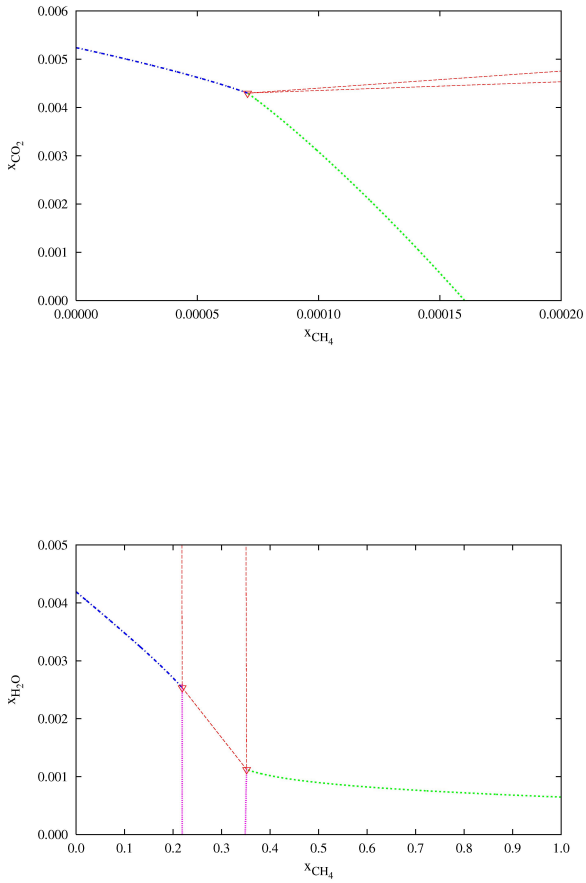


Figure 6.9: (a) $Px$ and (b) $Tx$ projections of the phase diagram for the methane(1) + carbon dioxide(2) binary mixture at different temperatures and pressures, respectively. The symbols correspond to the experimental data taken from the literature and the continuous curves to the predictions obtained from SAFT-VR: (a) at (from bottom to top) 170, 185, 210, 230 (circles[27]), 250 (squares[27]), 270 (diamonds[27,28]), and 300 K; (b) at 2 MPa (continuous curve), 4.137 MPa (circles[26] and dotted curve), 4.930 MPa (squares[26] and dashed curve), 6.206 MPa (diamonds[26] and dot-dashed curve), and 6.895 MPa (triangles[26] and dot-dot-dashed curve).

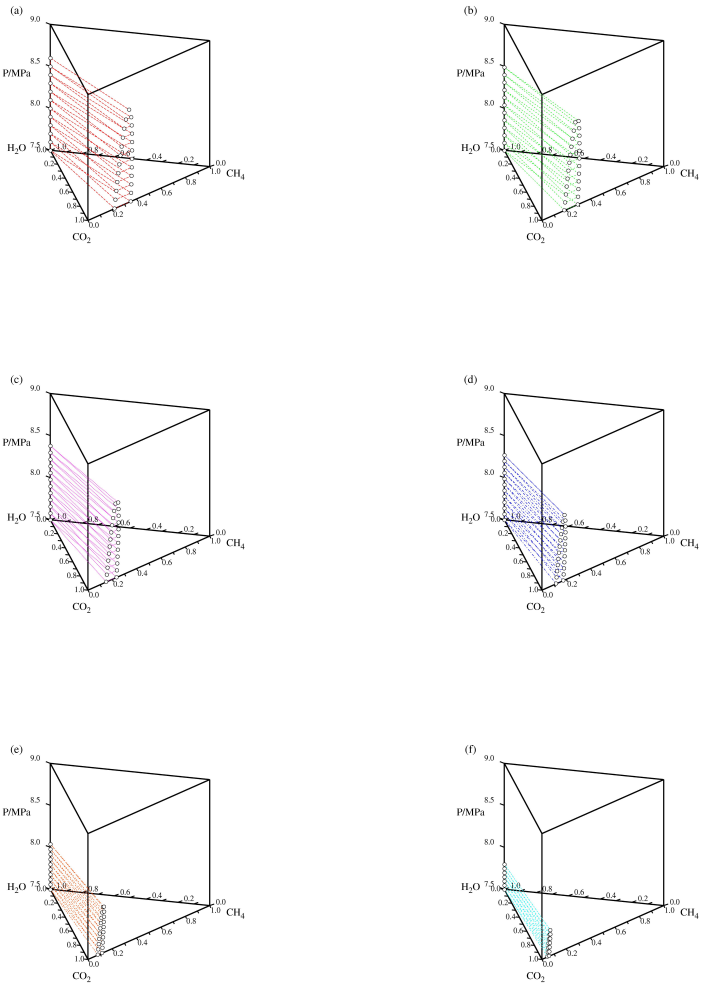


Figure 6.10: Tridimensional view of the ternary diagram, as a function of pressure, of the mixture $H_2O(1) + CO_2(2) + CH_4(3)$ as predicted from SAFT-VR at 275 K (a), 275 K (b), 280 K (c), 290 K (d), 295 K (e), 300 K (f). The dashed lines represent the sides of the triangles that bound the three-phase LLV coexistence region and the circles their corresponding compositions. The existing two-phase liquid-liquid and two-phase vapour-liquid coexistence curves, as well as the their corresponding tie-lines are not included to clarify the graphs.

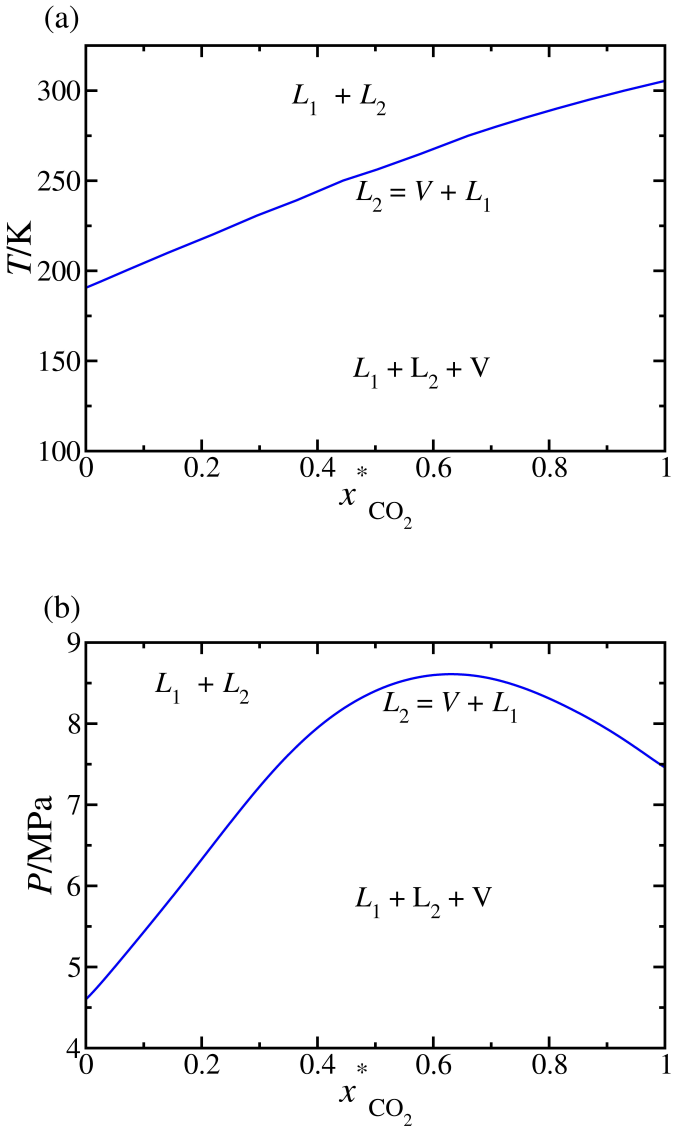


Figure 6.11: Upper critical endpoint temperatures (a) and pressures (a) as functions of the mole fraction of $x^*_{CO_2}$, the carbon dioxide mole fraction free basis.

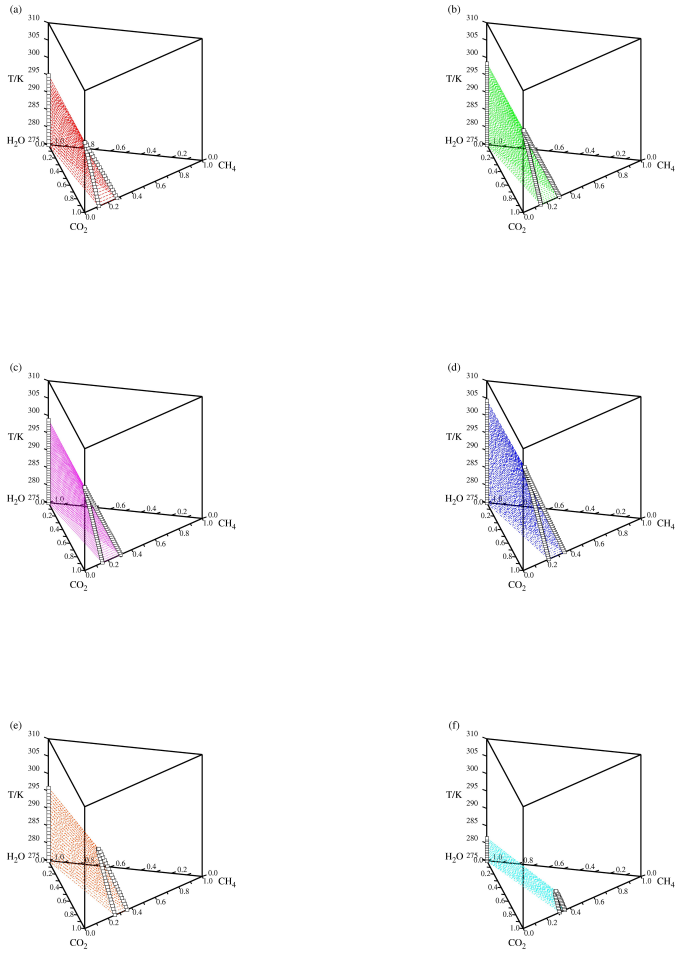


Figure 6.12: Tridimensional view of the ternary diagram, as a function of temperature, of the mixture $H_2O(1)$ + $CO_2(2)$ + $CH_4(3)$ as predicted from SAFT-VR at 6 MPa (a), 6.5 MPa (b), 7 MPa (c), 7.5 MPa (d), 8 MPa (e), 8.5 MPa (f). The dashed lines represent the sides of the triangules that bound the three-phase LLV coexistence region and the squares their corresponding compositions. The existing two-phase liquid-liquid and two-phase vapour-liquid coexistence curves, as well as the their corresponding tie-lines are not included to clarify the graphs.

# Chapter 7

# Simultaneous application of the Gradient Theory and Monte Carlo molecular simulation for the investigation of methane/ water interfacial properties

## 7.1 Abstract

This work is dedicated to the simultaneous application of the Gradient Theory of fluid interfaces and Monte Carlo molecular simulations for the description of the interfacial behaviour of the methane/water mixture. Macroscopic (interfacial tension, adsorption) and microscopic (density profiles, interfacial thickness) properties are investigated. The Gradient Theory is coupled in this work with the SAFT-VR Mie equation of state. The results obtained are compared with Monte Carlo simulations, where the fluid interface is explicitly considered in biphasic simulation boxes at both constant pressure and volume (NPT and NVT ensembles), using reliable united atom molecular models. On one hand, both methods provide very good estimations of the interfacial tension of this mixture over a broad range of thermodynamic conditions. On the other hand, microscopic properties computed with both Gradient Theory and MC simulations are in very good agreement with each other, which confirms the consistency of both approaches. Interfacial tension minima at high pressure and prewetting transitions in the vicinity of saturation conditions are also investigated.

## 7.2 Introduction

Methane is the major component in reservoir fluids, and like water is also present to a certain extent in natural reservoirs. Therefore the knowledge of

methane-water high pressure interfacial properties is essential for the exploration, production and processing of petroleum fluids[242,243]. The accurate determination of this property is especially important for the development of methods intended to enhance natural gas recovery from non conventional sources, as low permeability substrate reservoirs, where the injection of an external aqueous base fluid plays a key role. The knowledge of the capillary pressure between water and hydrocarbon phases, which is related to interfacial tension (IFT), is also of great importance for many industries.

The interfacial tension of methane-water mixture has been extensively measured. Schmidt *et al.*[244] reviewed the existing experimental data available in literature. Even if experimental data cover very wide temperature and pressure ranges: 273-473 K and 0.01-240 MPa, the majority of the data was measured at 298 K (approximately representing a third of all data points collected by Schmidt *et al.*[244]).

While methane-water interfacial tension experiments are well documented in the literature (Schmidt *et al.*[244]), the modeling of the IFT of this mixture has received much less attention. Let us mention the recent work of Biscay *et al.*[158] who performed Monte Carlo simulations in the $NP_N\Delta T$ ensemble at 373 K for pressures up to 500 bar and the one of Goufhi and Malfreyt[245] who have shown that the formation of a methane layer at the methane-water interface is thermodynamically favoured. In their review, Schmidt *et al.*[244] computed the IFT of the mixture with the linear gradient theory (LGT) of

interfaces. Although the LGT can constitute in some cases a computationally efficient and reliable theory to describe inhomogeneous fluids, this theoretical framework which is based on the assumption that the density profiles are distributed linearly, cannot describe accurately the phenomenon of adsorption at the interface. In order words, the density profiles are not obtained by minimization of the free energy in this approach but are instead taken as an input of the theory. Note, that in the case of methane-water binary mixture, this assumption is not correct as methane presents significant adsorption at the interface. It should be mentioned also that the thermodynamic models used by Schmidt *et al.*[244], cubic equations of state, are known to poorly describe the phase equilibria of this challenging system. A different approach is proposed here which makes use of an explicit description of the hydrogen bonding interaction in the free energy function through the use of the Statistical Associating Fluid Theory (SAFT). It will be shown that this challenging system can be adequately described if the gradient theory itself (i.e. with no a priori assumptions on density profiles) is coupled to the above mentioned molecular based equation of state.

From a macroscopic point of view, there are many approaches for computing the interfacial tension of simple fluids or mixtures. To mention just a few, let us quote first simple correlations such as the parachor method[246–248] and its derivatives, the corresponding-states principle[249,250] and other thermodynamic correlations[251–253]. Let us mention also theories that take into account

the density gradients in the interface such as the perturbation theory[254], integral and density functional theories[155,255–262] (in Ref.[155], a good review of the state-of-the-art of this approach can be found) or the gradient theory of fluid interfaces[146,263].

Among these approaches, the gradient theory of fluid interfaces plays a central role in the interfacial tension modelling of fluid mixtures. The foundations of this theory were established in the seminal work of van der Waals[263], and the theory was reformulated later in 1958 by Cahn and Hilliard[146]. The underlying basis of the theory is the conversion of the statistical mechanics of inhomogeneous fluid into a nonlinear boundary conditions problem that, once solved, provides access to density and stress distributions through the fluid interface. This approach has been already applied with remarkable success to a wide variety of fluids: hydrocarbons and their mixtures[71,147–149,264–276], polar compounds and their mixtures[270,277–280], polymer and polymer melts[281–284], near critical interfaces[285–288], and other liquid-liquid interfaces[289,290]. If this theory is combined with a thermodynamic model giving a reliable description of both phase equilibria and densities in the bulk phase, the gradient theory becomes a very efficient approach[73] to better understand interfacial behaviour. In this work, the gradient theory is coupled with the SAFT-VR-Mie[291] equation of state to describe the interfacial properties of the methane/water mixture. This recently proposed coupling has been successfully applied for the case study of $CO_2$-water mixture, but no simulations data were available at

that time to assess the microscopic description of the interface (density profiles, adsorption, prewetting)[131]. Another example of successful combination of an inhomogeneous fluid theory, in this case the Density Functional Theory, with a molecular based equation of state, is the so-called SAFT-VR-DFT approach[155,259–262], that has been recently applied to the precise description of the high pressure interfacial properties of carbon dioxide + n-alkane or water mixtures[186].

Even if macroscopic interfacial properties, such as interfacial tension, can be measured, it is very difficult to obtain experimental information at the molecular level for this kind of complex systems. Such microscopic information about the structure of the interfaces and the link between molecular model details and macroscopic interfacial properties can be obtained from a theoretical perspective using molecular simulation techniques. It is well known that the simulation of inhomogeneous systems is remarkably demanding from a computing point of view. Some reliable and fast new methods have been proposed recently to determine fluid interfacial properties during this type of simulations, representing an alternative route to the classical calculation of pressure tensor components. Among these recent competitive techniques, the Test-Area (TA)[63], wandering interface (WIM)[64], or Expanded Ensemble[65] methods may be outlined. These area sampling methods represent an alternative route to the determination of interfacial properties, as reviewed and discussed by Errington and Kofke[72]. These methods are being readily used to

describe a wide variety of systems, and as example the TA has been applied to the cases of Lennard Jones chains[68], water[1], the Mie potential[74] or binary mixtures[132].

The aim of this work is to simultaneously apply the Gradient Theory (GT) of fluid interfaces and Monte Carlo (MC) molecular simulations for the description of the interfacial properties of the methane/water mixture.

The work is organized as follows. First, the principal details of the Monte Carlo simulations are given. Then, a brief recall of the gradient theory follows. Results and Discussions are presented in the next section and finally conclusions are summarized.

## 7.3 Monte Carlo simulation procedure

The coexistence of fluid phases and interfacial properties for the studied mixture has been analyzed by considering a single inhomogeneous biphasic simulation box using constant pressure (NPT ensemble) and constant volume (NVT) Monte Carlo simulations. This explicit interface simulation technique has the advantage of providing direct access to the structure of the interface, allowing the simultaneous determination of bulk coexistence properties (densities of the present phases), different interfacial properties (interfacial tension, adsorption coefficients), and microscopic properties as density profiles across the interface, interface thickness, radial distribution functions, etc.

Nevertheless, the scaling of the system, potential instability of the simulated box, correct determination of the statistics of the determined properties, and handling of the long range corrections in the multiphasic system represent important issues that must be carefully considered as they affect to a great extent the numerical results of all the properties estimated.

The quantitative results obtained depend also to a great extent of the molecular model selected for each of the species present. The molecule of methane is often represented as a single Lennard Jones sphere[132,133], and this united atom representation, although very simple, offers accurate results not only for phase equilibria but also for bulk properties in a wide pressure and temperature ranges, including second derivative properties[187,188]. In this work, the parameterization chosen for methane is the one proposed by Möller *et al.*[132] Concerning water, a considerable large number of molecular models have been proposed in the literature. In this case, we have selected a rigid non polarizable model, the so-called TIP4P-2005[106]. This model considers three punctual electric charges placed on each molecule atom, and an additional Lennard Jones interacting site placed in the bisector of the angle formed by the molecule bonds. This model has been shown to provide accurate estimates of water bulk properties, if compared with other similar versions, but also is remarkably proficient in the estimation of interfacial properties, as shown by de Miguel and Vega[1].

The procedure used to simulate the biphasic interfaces is the following.

## 7.3. MONTE CARLO SIMULATION PROCEDURE

In the case where equilibrium between hardly miscible phases is analyzed, the first step entails the equilibration of two independent simulation boxes. One of them contained 256 methane molecules, and the other 1372 water molecules. Both boxes were equilibrated in the NPT ensemble at the desired temperature and pressure. Simulations were organized in cycles, where each cycle consisted in $N_P$ attempts to displace a molecule, $N_P$ standing for the number of molecules in the simulation box, $N_P$ attempts to rotate a molecule in the case of water, and one attempt to change volume. Maximum distance, rotation angles and volume displacements were monitored along the run to approach a 30% acceptance ratio. The usual periodic boundary conditions and minimum image convention apply in all cases in this work. The dimensions of the parallepipedic simulation box,$L_x$, $L_y$ and $L_z$ were adjusted to facilitate the subsequent assembly of a biphasic box, and thus the dimensions $L_x$ and $L_y$ were kept constant with a value $L_x$=$L_y$=37.3 Å, which corresponds to ten times the methane Lennard-Jones characteristic core parameter $\sigma$. This way, the volume variations of the simulation box were performed by variations in the $L_z$ distance. For the case of water, the coulombic interactions were accounted for using the Reaction Field method, instead of the widely used Ewald summation technique. In a recent paper[129], it has been shown that, from a quantitative point of view, the use of Reaction Field in the determination of water interfacial properties using Monte Carlo Simulation yields equivalent results to those obtained with the Ewald sums method, with the advantage

of a very considerable reduction in computing times. For the Lennard Jones contribution to the internal energy, the potential was truncated at a cut-off radius of rc=5$\sigma_{LJ}$, and no further long-range corrections were applied.

Once both boxes were equilibrated, a slab composed by the water simulation box in the middle, and two replicas of the methane box at both ends in the z direction was assembled, by simply displacing the appropriate value of the z coordinate for both methane boxes. This yielded an inhomogeneous simulation box containing two explicit interfaces between both fluids. For the case of liquid-liquid equilibria of fluid phases with different composition of the mixture, the procedure was similar, but each box equilibrated separately contained a mixture of water and methane, whose composition had been tentatively determined previously using the SAFT-VR Mie EOS, and then used to determine the number of molecules of each variety that had to be included in each box. Note that the recent work of Miguez *et al.*[130] presents an account of the phase equilibria for this binary mixture, described using the SAFT-VR approach. Next, once the biphasic box was constructed, it was allowed to evolve under NPT conditions until the interface was equilibrated, which usually took an average of 106 cycles. After this, the production stage followed, under NVT conditions this time, so the interfacial tension could be computed using the sampling area method denoted as TA method[63], and the mechanical route, determining the pressure components through the method proposed by de Miguel and Jackson[66]. In both cases the interfacial tension values deter-

mined agreed to each other within the error bars determined by the usual block averaging method, and the values plotted in this paper represent the average of both values. At this stage of the calculation, the box was divided in 100 identical slabs, perpendicular to the z-axis, and the density in each of them was computed to construct the density profile of the box across the interfaces.

## 7.4 Density Gradient Theory

The gradient theory has been described extensively by several authors. Therefore, the discussion on this theory will be limited to its most significant features. For further details, the reader is referred for instance to Bongiorno *et al.*[258,292], Davis *et al.*[266,293], Carey's thesis[265] or Davis monography[151].

Using the assumption that the molecular gradients in the interface are small compared with the reciprocal of the intermolecular distance, the gradient theory allows expanding the Helmholtz free energy in a Taylor series around the homogeneous state and truncated after the second order term to give:

$$F = \int_V [f_0(n) + \sum_i \sum_j \frac{1}{2} c_{ij} \nabla n_i \nabla n_j] dV \tag{7.1}$$

where $\nabla n_i$ represents the local density gradient of component i. Thus, in the absence of an external potential, the Helmholtz free energy density of an heterogeneous fluid can be expressed as the sum of two contributions: the Helmholtz free energy $f_0$(n) of an homogeneous fluid at local composition n,

and a corrective term which is function of the local density gradients. The coefficients $c_{ij}$ denote the so-called influence parameters, whose physical interpretation is related to the molecular structure of the interface, and essentially determine the density gradients response to the local deviations of the chemical potentials from their bulk value[292].

According to the minimum free energy criterion applied in Eq 7.1, in the case of a planar interface, with the assumption that the density dependence of the influence parameters can be neglected[147,274,294] the equilibrium densities $n_i$(z) must satisfy the following Euler-Lagrange equations:

$$\sum_j c_{ij} \frac{d^2 n_j}{dz^2} = \mu_i^0(n_1, ..., n_N) - \mu_i \equiv \Delta\mu_i(n_1, ..., n_N) \quad for \quad i, j = 1, ..., N \quad (7.2)$$

where $\mu_i^0 \equiv (\frac{\partial f_0}{\partial n_i})_{T,V,n_j}$ , and $\mu_i$ stands for the chemical potential of component i in the coexisting bulk phases. This set of equations, that allow to compute the density profile of each component across the interface, is solved here by a Galerkin method[151].

Once the density profiles are known, the interfacial tension $\gamma$ can be calculated through the use of the following equation:

$$\gamma = \int_{-\infty}^{+\infty} \sum_i \sum_j c_{ij} \frac{dn_i}{dz} \frac{dn_j}{dz} dz = \int_{-\infty}^{+\infty} 2[f_0(n) - \sum_i n_i \mu_i + P] dz \quad (7.3)$$

Thus, once the phase equilibrium is obtained, the only inputs of the gra-

dient theory are the free energy density of the homogeneous fluid and the influence parameters of the inhomogeneous fluid. A single equation of state is used to model both the equilibrium properties and the free energy density in the interface. Hence, given an EOS and a set of influence parameters, the gradient theory provides an unified theory for predicting both the fluid phase behaviour and interfacial properties (surface tension, density profiles,...).

In this work, the Helmholtz free energy of the methane-water mixture is calculated with SAFT-VR Mie EOS[291]. This equation of state is a modified version of the original SAFT-VR equation[59] in which a n-6 variable Mie potential is used as a reference intermolecular potential to describe chain and associating molecules. The concept of using this generalised Lennard-Jones potential for the elementary building block of homonuclear chains of spherical segments has proven[291] to be very fruitful in order to model simultaneously the fluid phase behaviour and second-derivative properties of real fluids. This equation can be written in terms of the residual Helmholtz free energy as follows:

$$\frac{F^{RES}}{NkT} = \frac{F^{MONO}}{NkT} + \frac{F^{CHAIN}}{NkT} + \frac{F^{ASSOC}}{NkT} \tag{7.4}$$

where N is the number of molecules, T is the temperature and k is the Boltzmann constant.

In the case of mixtures containing both chain and associating molecules, the free energy can be expressed as a sum of three microscopic contributions: a monomer term $F^{MONO}$, which takes into account the attractive and repul-

sive forces between the segments that form the molecules, a chain contribution $F^{CHAIN}$, which accounts for the connectivity of the molecules, and an association term $F^{ASSOC}$, which takes into account the contribution to the free energy due to hydrogen-bonding interactions.

For a detailed description of these contributions, the reader is referred to earlier publications[213,291]. As in the case of all SAFT EOSs, the SAFT-VR Mie approach requires the determination of the intermolecular potential parameters which are typically obtained by fitting to experimental macroscopic data. The parameters used in the SAFT-VR Mie EOS for methane and water were obtained in previous works[131,291]. They are summarized in Table 8.1.

Table 7.1: SAFT-VR Mie molecular parameters for methane and water and influence parameters used in the Gradient Theory.

| | $m$ | $\sigma(\mathring{A})$ | $\epsilon/\kappa(K)$ | $\lambda_{rep}$ | $\kappa^{AB}$ | $\Psi^{AB}/\kappa(K)$ | $C(10^{-20} \cdot m^5 \cdot mol^{-2})$ |
|---|---|---|---|---|---|---|---|
| $CH_4$ | 1 | 3.7203 | 124.43 | 8.8688 | | | 2.0387 |
| $H_2O$ | 1 | 3.0856 | 177.6851 | 6.1232 | 0.046477 | 1406 | 1.3989 |

As proposed originally by Carey[265], the crossed influence parameters $c_{ij}$ are related to the geometric mean of the pure component influence parameters $c_i$ and $c_j$ by:

$$c_{ij} = \beta_{ij}\sqrt{c_i c_j} \tag{7.5}$$

where $\beta_{ij}$ stands for an adjustable binary interaction parameter that must be comprised between 0 and 1[265]. It is important to point out that the influence parameter of the pure fluid can be obtained through the use of a rigorous

theoretical expression[286,292] which requires the knowledge of the direct correlation function of the homogeneous fluid. However, this quantity is not readily available for most of the systems of practical interest so that the influence parameters are generally estimated from measurable or computable quantities such as the surface tension. In this work, they were derived from the experimental surface tension, as previously described in previous references[131,274]. The values of the influence parameters obtained for water and methane are given in Table 8.1.

## 7.5 Results and discussion

### 7.5.1 Interfacial tension

Fig. 7.1a shows the comparison between the experimental interfacial tensions at 298 K and the ones computed with the gradient theory and the molecular simulation. The experimental data are taken from different studies[30,32,33,295]. More experimental data sets exist at this temperature and were reviewed by Schmidt *et al.*[244] As they are in agreement with the ones plotted here, we did not add them for clarity. The optimal value $\beta_{12}$=0.75 for the interaction coefficient of the influence parameter allows to satisfactory reproduce the interfacial tensions up to high pressures with the gradient theory as the calculated IFTs are within the sets of experimental data. Two interfacial tension values were calculated at 2 and 8 MPa, respectively, using MC

molecular simulation, and the agreement between these values and the GT and experimental values is very satisfactory, as shown in this plot.

As shown in Fig. 7.1b, the GT+SAFT-VR Mie approach yields also a satisfactory prediction of the interfacial tension of $CH_4/H_2O$ mixture at higher temperatures and pressures: T =373 K and 473 K and pressures up to 260 MPa. Indeed, the theory seems to be able to correctly capture the minimum in IFT with increasing pressure. This minimum has been observed by Wiegand and Franck[30] for other water-hydrocarbon systems. As it is going to be demonstrated, the gradient theory allows to explain the presence of this minimum.

First of all, as pressure increases, the interfacial thickness decreases slightly as shown in Fig. 7.3 at 373 K. The interfacial thickness plotted in Fig. 8.2 is computed with the 10-90 criterion applied to the water density. This decrease is sometimes used to explain the increase in IFT at high pressure. However, its trend alone cannot justify the minimum in the IFT-pressure isotherm.

We have computed the relative adsorption of methane (as defined by Gibbs) with the following equation (cf. Ref.[131] for details):

$$\Gamma_{12} = -\alpha_1 \int_{-\infty}^{+\infty} \Delta C(z) dz \tag{7.6}$$

where $\Delta$C(z) is the symmetric interface segregation that represents the local

relative concentration of the two species, given by:

$$\Delta C(z) = \frac{n_2(z) - n_2^{II}}{\alpha_2} - \frac{n_1(z) - n_1^{II}}{\alpha_1} \tag{7.7}$$

where $n_i(z)$ as defined previously and the symmetric concentrations $\alpha_i$ (i=1 for methane, i=2 for water) in Eq. 7.7 are given by:

$$\alpha_i = \frac{n_i^{II} - n_i^{I}}{(n_1^{II} + n_2^{II}) - (n_1^{I} + n_2^{I})} \tag{7.8}$$

where I denotes the $CH_4$ rich phase and II the water rich phase.

As an example, Fig. 7.3 shows the pressure dependence of methane adsorption at 373 K, plotted together with estimated IFT values for comparison. In the low pressure range, as pressure increases, the adsorption of methane in the interface increases rapidly until it reaches a maximum around 20 MPa. Meanwhile, IFT decreases with an important slope. Between approximately 20 and 80 MPa, methane adsorption is positive but decreases with pressure; while IFT is still decreases but more slightly. Around 80 MPa, methane adsorption vanishes; and at the same pressure IFT reaches its minimum. Beyond 80 MPa, methane adsorption becomes negative; and then IFT increases with pressure. These results show that this unusual behaviour of IFT with pressure (presence of a minimum) should be essentially attributed to methane adsorption, and not to the shrinkage of the interface.

### 7.5.2 Density profiles

One of the main advantages of both methods is that they can be used to compute molecular scale interfacial properties, including density profiles, which are hardly accessible to experimental observation.

Fig. 7.4 depicts, as an example, the structure in $CH_4/H_2O$ interface at 298 K for two pressures: 2 MPa (Fig. 8.5a) and 8 MPa (Fig. 8.5b). The behaviour is in agreement with the one observed previously, for instance, for the case of the $CO_2$-water interface[131] or mixtures made up of hydrocarbon with $N_2$, $CO_2$ or $CH_4$[149]. The density of water increases monotically across the interface with the traditional tanh shape. No change in the shape of the water profile is evident with increasing pressure. In addition, the free energy of the system is minimized by the adsorption of methane molecules at the interface, which is illustrated in Fig. 7.4. The adsorption peak is located on the methane rich side of the interface due, to the low solubility of methane in water rich phase in this pressure and temperature conditions. The same result were obtained by Biscay *et al.*[34] for this system. These results are in perfect agreement with the conclusions of the work of Ghoufi and Malfreyt[245] who established that the formation of a methane film at the methane/water interface is thermodynamically favoured and is the starting point of the formation of hydrophobic cages around methane molecules due to hydrophobic forces[296]. Fig. 7.4 shows also the good agreement between the density profiles computed with the gradient theory with the ones obtained from MC molecu-

lar simulations. This result highlights the consistency of the Gradient Theory when it is combined with an equation of state based on a rigorous statistical mechanics foundation and a realistic intermolecular potential model for each substance. It must be noted here that the molecular simulation profiles of the interface shown in Fig. 7.4 correspond to only half of the simulation box, because as it has been already explained, symmetrical boxes containing two explicit interfaces are used in this case. Fig. 7.5 will show later a complete simulation box profile. The reason for the choice done in Fig. 7.4 is to focus on the shape of the profiles across a single interface. A comparison between GT and MC profiles shows that the equilibrium bulk density values agree very well to each other, and although MC profiles show the cited methane adsorption at the interface, the height of this peak is underestimated if compared with the GT profile.

The density profiles computed with GT were previously compared with Molecular Dynamics estimations for Lennard-Jones mixtures[297] and binary alkane mixtures[298] and a good agreement was observed between both methods.

Fig. 7.5 shows the profiles across the interface for the mixture at 550 K and 75 MPa. In this high pressure conditions the mixture shows a phase split with liquid-liquid equilibria between a water-rich and a methane-rich phase -which is typical for this kind of binary mixture, and corresponds to type III-b according to the classification of Scott and van Konynenburg, as it is discussed in detail in Ref.[130]. Nevertheless, and contrarily to the case shown

in Fig. 7.4, no adsorption of any of the species is shown in the interface. Note that although GT and MC display slight discrepancies in the corresponding densities of the richest compound in each phase, the overall trend is very similar with both approaches. It should be mentioned here that, contrarily to the plot made in Fig. 7.4, now the complete density profile across the central region of the simulation box is shown, and only both ends of the box have been trimmed.

### 7.5.3 Prewetting

All the thermodynamic conditions explored experimentally correspond to temperatures above the critical temperature of methane. Comparisons with molecular simulations at these conditions (see Figs. 7.4 and 7.5) show clearly the physical consistency of the density profiles computed with the gradient theory. In this work we have decided to also explore other thermodynamic conditions (below the critical point of methane) where phenomena that are more interesting from a fundamental point of view can be found. Particularly, we have computed with both methods the density profiles of methane at the gaseous methane/liquid water interface at the approach of the saturation pressure of $CH_4$.

Fig. 8.7 depicts the density profile of methane just below its saturation pressure at 170K. Methane accumulates and forms a thin liquid film that perfectly wets the interface between the gaseous methane and the liquid water.

As the pressure increases, this adsorbed layer grows thicker continuously just below the saturation pressure of methane. This change in the surface coverage from a thin to a thick liquid film represents a prewetting transition[299], which means that $T_{cw}<T<T_c$, $T_{cw}$ being the critical wetting temperature. In a previous work[131], we have shown that the gradient theory could predict such a prewetting phenomenon, but no molecular simulations were available to support (or not) these results. Here, the MC methane density profiles are in very good agreement with the ones obtained with GT which demonstrates the consistency of the two approaches.

## 7.6 Conclusions

In this work, the gradient theory of fluid interfaces and Monte Carlo molecular simulations were simultaneously applied for the description of the interfacial behaviour of the methane/water mixture. The interfacial tension of the mixture could be modeled accurately both with GT and MC molecular simulations in a broad range of thermodynamic conditions.

One of the most attractive features of both methods is that they also provide the interfacial density profiles of each component across the interface. A nearly systematic adsorption of methane in the interface is observed, and a prewetting transition has been detected just below the saturation pressure of methane as the thin liquid methane film appearing at lower pressures grows

thicker in the immediacy of the saturation pressure. Both methods lead to very similar density profiles for all the thermodynamic conditions considered, which confirms the consistency of these two approaches. We have also highlighted the usefulness of the Gradient Theory in providing insight in the appearance of subtle phenomena such as the minimum of surface tension at relative high pressure. According to this work, this behavior should be attributed to the variation of methane adsorption with pressure.

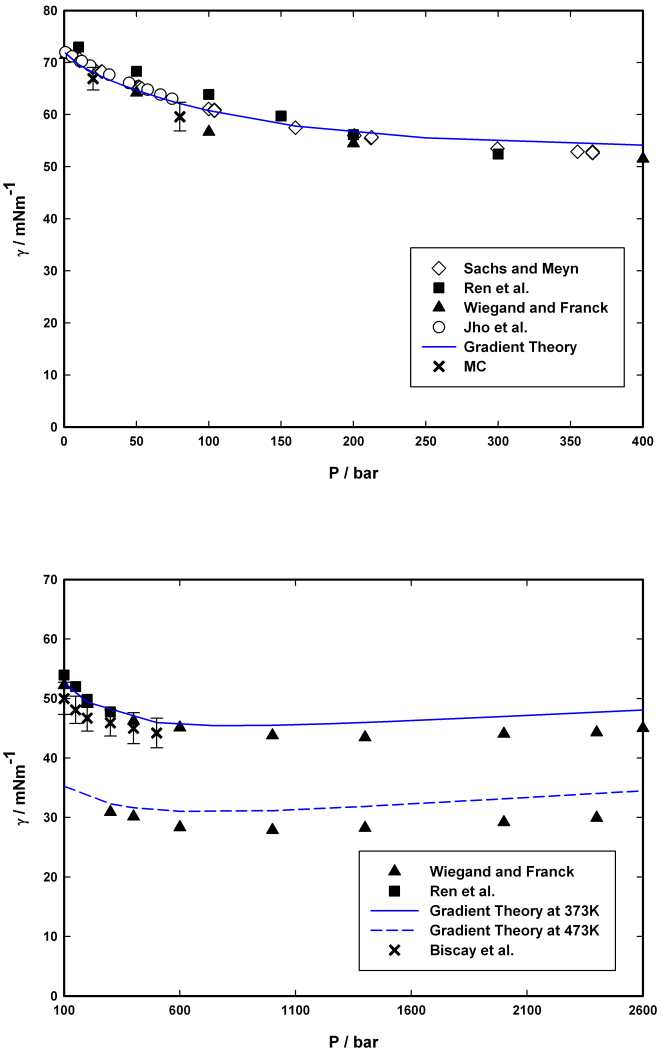


Figure 7.1: Interfacial tension versus pressure for methane/water mixture in the liquid-liquid region of the phase diagram. Experimental data: (filled triangles) Wiegand and Franck[30], (open circles) Jho *et al.*[31], (open diamonds) Sachs and Meyn[32], (filled squares) Ren *et al.*[33], (crosses) MC results, (continuous and dashed curves) Gradient theory of fluid interfaces with $\beta_{12}$=0.75. (a) T = 298 K. (b) T = 373 K and T = 473 K (crosses) MC results from Ref.[34]

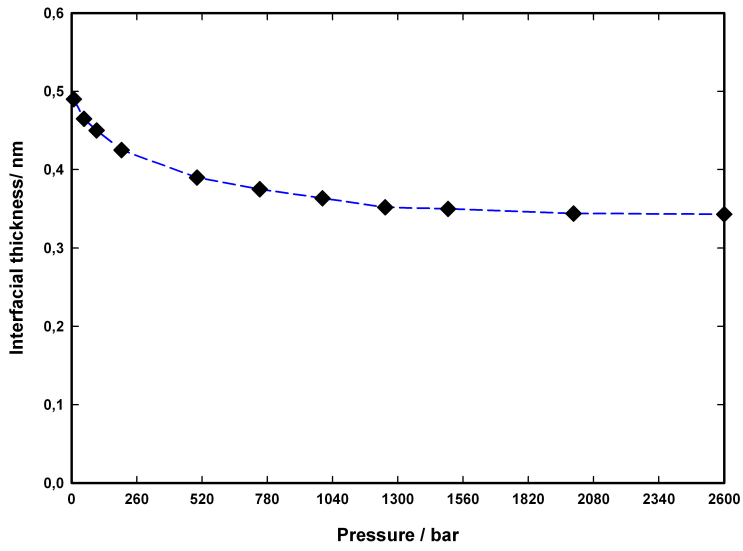


Figure 7.2: Interfacial thickness versus pressure at T = 373 K (liquid-liquid region) computed with Gradient Theory and 10-90 criterion applied to water density.

.

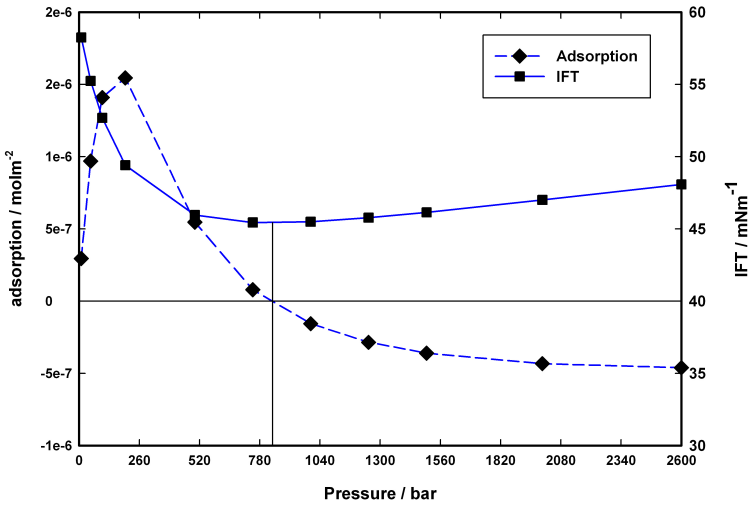


Figure 7.3: (filled diamonds) Methane adsorption ($\Gamma_{12}$) at 373 K (liquid-liquid region) computed with Eq. 7.6. (filled squares) Interfacial tension at 373 K (same as in Fig. 8.2).

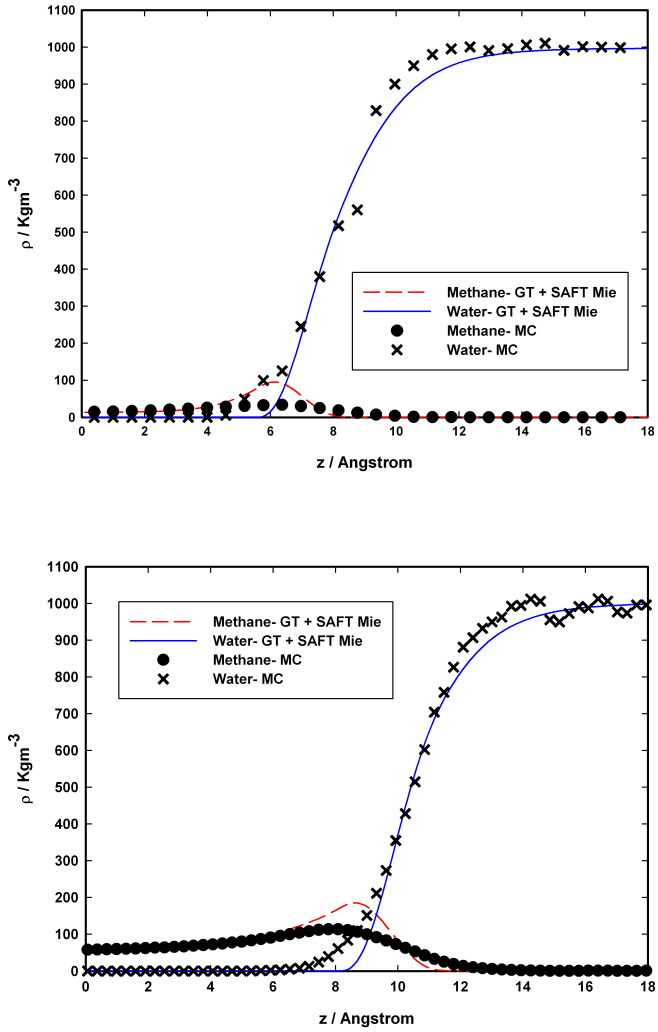


Figure 7.4: Density profiles across the interface (liquid-liquid region) for methane/water mixture at 298 K and (a) 2 MPa, (b) 8 MPa: (continuous curve) Water (GT), (dashed curve) Methane (GT), (crosses) Water (MC simulation), (filled circles) Methane (MC simulation).

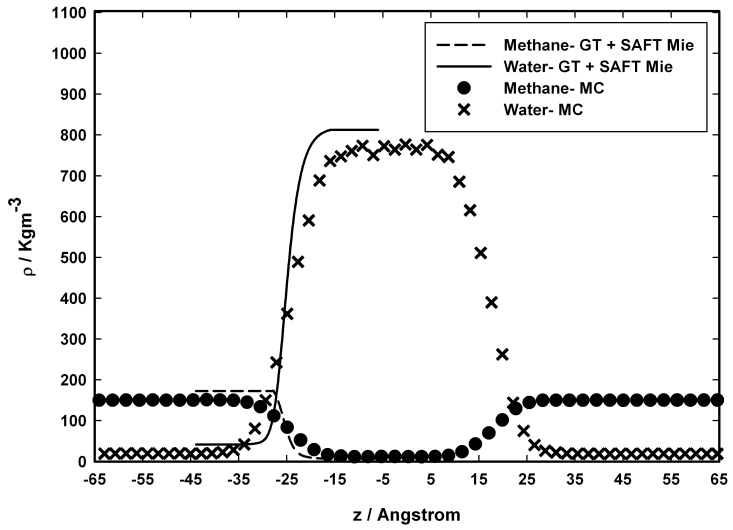


Figure 7.5: Density profiles across the interface for methane/water mixture at 550 K and 8 MPa (liquid-liquid region). See inset for legend.

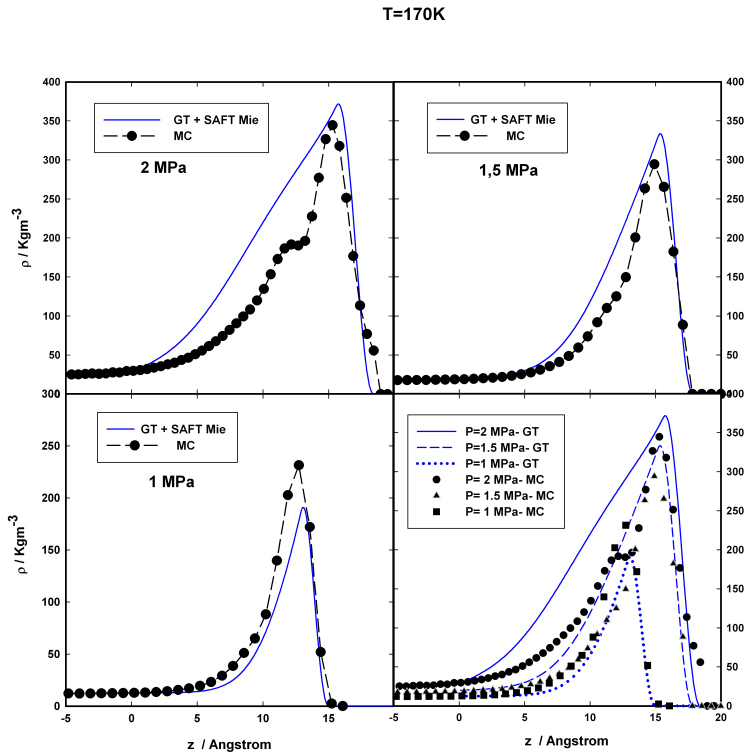


Figure 7.6: Methane density profile at the methane/water interface (gas-liquid region close to the three-phase line) at T = 170 K and (a) P=2 MPa, (b) 1.5MPa, (c) P=1 MPa, (d) Comparison of the three pressure values. See the inset for legend details.

# Chapter 8

# Determination of the interfacial properties of the mixture $CO_2 + H_2O + CH_4$ in the LLV triphasic region using Monte Carlo molecular simulation

## 8.1 Abstract

In this work, we have investigated the interfacial behaviour of the carbon dioxide + water, and methane + carbon dioxide + water mixtures using Monte Carlo molecular simulation. Simulations were performed considering explicit fluid interfaces in biphasic simulation boxes where macroscopic (interfacial tension, adsorption) and microscopic (density profiles) interfacial properties were calculated. Methane was modelled following the united-atom approach, as a single LJ sphere. On the other hand, water and carbon dioxide were represented using more complex models, considering rigid non polarizable structures with both Lennard-Jones sites and point electric charges, corresponding to the well-known TIP4P/2005 and EPM2 models, respectively. Carbon dioxide + water results obtained were compared with gradient theory+ SAFT-VR Mie estimations published in a previous work. For the case of the ternary mixture, a detailed methane/carbon dioxide adsorption analysis in contact with a rich-water fluid phase were performed at different temperature and pressure conditions (including the triphasic liquid-liquid-vapour (LLV) conditions).

## 8.2 Introduction

In the last few years, the precise determination of inhomogeneous fluid systems including $H_2O$, $CH_4$ and $CO_2$ interfacial properties has received much attention due to its relevant industrial and environmental implications. These

fluids are greatly involved, for instance, in processes of enhanced natural gas recovery from the so-called non conventional sources, and also the studies concerning geological $CO_2$ storage[242,243]. In these two applications, the interactions between the fluid and the solid substrate play an essential role, and the conditions of adsorption, wetting, or confinement effects are determined by the interfacial interactions present. In this context, obtaining an accurate description of the interfacial properties between the fluids present is a key step towards a better understanding of the physics of the problem. Experimental data for these properties are still scarce, due to the considerable technical difficulties associated to the design and operation of experimental setups working especially in ranges of extreme pressures and temperatures. This handicap makes theoretical estimation even more important, and the critical evaluation of existing theories and the development of new approaches are undoubtedly highly desirable goals.

For these reasons, a number of new and interesting works are being published in this field, proposing different approaches. For instance, the group of Jackson has presented remarkable results studying the interfacial properties for this type of fluid systems with a combination of the Density Functional Theory (DFT) and the SAFT-VR[59,202] molecular equation of state (EoS), applied to $CO_2$ mixtures[186], or in a more general perspective to reservoir fluids[300]. With a similar approach, Lafitte *et al.*[131] combined the Density Gradient Theory (DGT) with the SAFT-VR Mie[291] EoS to describe the interfacial behaviour

of $CH_4$ + $H_2O$. Hu *et al.*[301] have studied the interfacial tension of the $CO_2$ + $H_2O$ mixture using DFT. These inhomogeneous media theories, DGT and DFT, have proved to be versatile and reliable, and their ability to describe different types of interfacial behaviours, combined with their solid physical foundations, is to be underlined.

Molecular Simulation is another very valuable approach for this type of systems. Although much slower than other theories, which does not allow to explore wide condition ranges, the possibility to obtain a precise characterization of the microscopic fluid structure for a given molecular model offers an important added value. The possibility to obtain a link between the details of the molecular models, and the influence of every variable on the macroscopic interfacial structure and properties is to be also cited. Despite this potentiality, it must be reminded that the quantitative interfacial properties results depend to a great extent of the molecular models chosen to describe the fluids, and also on the precise treatment of all variables involved in the simulation. For instance, a rigorous treatment of the long-range corrections of both the coulombic and dispersive terms of the intermolecular potential determine to a great extent the quantitative results obtained from the calculation, as shown recently[302].

The cited molecules have been widely studied using various Molecular Simulation techniques either in bulk homogenous conditions, or for inhomogeneous fluids presenting interfaces. In a recent work, Miqueu *et al.*[70] studied the $CO_2$

+ $H_2O$ interfaces using inhomogeneous Monte Carlo (MC) simulation, comparing the results with the DGT + SAFT VR Mie approach. Nielsen *et al.*[303] have focused also on this binary mixture, using Molecular Dynamics (MD) and concentrating their attention in the conditions of $CO_2$ geological storage. Neyt *et al.*[304] used byphasic and Gibbs Ensemble MC to analyze the interfacial properties of mixtures of $CO_2$ with several alkanes.

In this context. The main objective of this work is to study the use of Monte Carlo molecular simulations to describe the interfacial behavior of the $H_2O + CH_4 + CO_2$ ternary mixture in bulk conditions, focusing on several regions that yield different interfacial scenarios, in pressure and temperature ranges related with the practical applications described above.

## 8.3 Models and simulation details

The methodology used in this paper is same used in a previous work[70]. Now, the described technique has been used to study the interfacial properties of the coexisting fluid phases of two different systems: $H_2O + CO_2$ binary mixture and $H_2O + CH_4 + CO_2$ ternary mixture, in the latter case focusing of the triphasic liquid-liquid-vapour (LLV) region.

Methane is modelled, following the united-atom approach, as a single Lennard-Jones sphere, using the parametrization proposed by Möller et al.[132]. This model, albeit simple, offers accurate results in the calculation of inter-

facial properties, as shown by several authors[70,158,245]. Concerning $CO_2$, a considerably large number of molecular models have been proposed in the literature, but the most usual model is a linear-rigid chain molecule with three segments, representing each of the $C$ and $O$ atoms. In this rigid non polarizable models each segment or interacting site consists of a combination of a LJ site plus an electric point charge. This structure mimics the typical anisotropic feature of carbon dioxide, including the large quadrupole moment value accounted for the three partial charges. The parametrization chosen for this molecular structure is the one proposed by Harris and Yung[15], the so-called EPM2 model, because this model were optimized to reproduce accurately thermophysical properties, such as the critical point[15] or VLE of binary mixtures[137]. In the case of water, the well-known rigid non polarizable $TIP4P/2005$[106] model was selected. This model considers four interacting sites placed on the oxygen atom $O$, on each of the hydrogen atoms $H$, and along the $H-O-H$ bisector the so called M-site. This model has been shown to provide accurate estimates of water bulk properties, if compared with other similar versions, but also is remarkably proficient in the estimation of interfacial properties, as shown by Vega and de Miguel[1]. Table 8.1 summarizes the characteristic parameters for all the molecular models used in this work.

For these models, the intermolecular interactions between two sites, $a$ and $b$, of different molecules $i \neq j$ are defined by the site-site potential defined as follows:

Table 8.1: Lennard-Jones well depth $\epsilon$ and size $\sigma$, partial charges $q$, and geometry, of the $CH_4$, $H_2O$ and $CO_2$ models used.

| *Atom* | $\epsilon/\kappa(K)$ | $\sigma(\mathring{A})$ | $q(e)$ | *Geometry* |
|---|---|---|---|---|
| $Lennard-Jones\ CH_4$ | 149.92 | 3.7327 | 0 | |
| $TIP4P/2005\ H_2O$ | | | | |
| $O$ | 93.20 | 3.1589 | 0.0 | $O-H: 0.9572\mathring{A}$ |
| $H$ | 0.0 | 0.0 | 0.5564 | $O-M: 0.1546\mathring{A}$ |
| $M$ | 0.0 | 0.0 | $-1.1128$ | $H-O-H: 104.52°$ |
| $EPM2\ CO_2$ | | | | |
| $C$ | 28.129 | 2.757 | 0.6512 | $C-O: 1.149\mathring{A}$ |
| $O$ | 80.507 | 3.033 | $-0.3256$ | $O-C-O: 180°$ |

$$u_{ab} = 4\epsilon_{ab}\left(\left(\frac{\sigma_{ab}}{r_{ab}}\right)^{12} - \left(\frac{\sigma_{ab}}{r_{ab}}\right)^{6}\right) + \frac{1}{4\pi\epsilon_0}\frac{q_a q_b}{r_{ab}}$$

where $r_{ab}$ is the distance between sites, $q_a$ and $q_b$ are the partial charges on these sites, and $\epsilon_{ab}$ and $\sigma_{ab}$ are the LJ cross parameters computed from $\epsilon_a$, $\epsilon_b$ and $\sigma_a$, $\sigma_b$, respectively, using the Lorentz-Berthelot mixing rules.

The LJ contribution to the internal energy was computed with a spherical cut-off radius ($r_c$), and long-range corrections (LRCs) was evaluated with the method proposed by Janeček[111], and later modified by MacDowell and Blas[119].The Janeček's method accounts very accurately for the LRCs in inhomogeneous systems along the whole range of temperatures in which the system exhibits vapour-liquid coexistence[305], and what is more important, when the method is employed, the values of interfacial properties obtained with the cut-off distance $r_c = 2.5\sigma$ are identical with those obtained for cut-off distance $r_c = 5.5\sigma$[111,305]. Consequently, the cut-off radius was set to $3\sigma$ in

this case. The coulombic interactions were dealt with the Reaction Field (RF) methodology, instead of the widely used Ewald summation tecnique. Previous works have shown that the use of the RF method yields analogous results to the computationally much more demanding Ewald sum method in the calculation of the interfacial tension and coexistence densities of diverse systems: liquid-vapor simulations of water[129], liquid-liquid simulations of $CH_4 + H_2O$ binary mixture[70]or biomolecular systems[306].

The procedure used to simulate the multiphasic interfaces, which was first introduced by Liu[58] can be summarized as follows. In the case of biphasic phase equilibria, the first step is the equilibration of two independent simulation boxes, in the $NPT$ ensemble at the estimated coexistence temperature and pressure. The dimensions $L_x$ and $L_y$ of these boxes were kept constant with a value $L_x = L_y = 35$ $\mathring{A}$ and volume variations were performed by variations only in the $L_z$ distance to facilitate the posterior assembly of a biphasic box. The usual periodic boundary conditions and minimum image convention were applied. The number of molecules of each specie in the two boxes depends obviosly on the composition of the involved equilibrium phases, which has been determinated by using the SAFT-VR equation of state[59,202]. In a recent paper, a detailed phase equilibria study of the ternary mixture $H_2O + CH_4 + CO_2$, and the invloved binaries was performed using this approach[130]. A similar approach has been recently used by Forte*et al.*[307] to describe accurately the phase diagram of ternary mixtures containing $H_2O$, $CO_2$ and several

alkanes. The number of molecules was adjusted in every case depending on the system composition, but always having at least 1024 water present in the system. It must be emphasized here that this initial guess of the equilibria conditions is essential for the eventual success of the molecular simulation, because if the initial values of the involved variables are far from the coexisting conditions of the molecular models used the boxes will not develop a stabilized interface after they have been put in contact. At this point, it is important to remind that although the molecular model on which the equation of state is grounded is not the same than the used in the MC simulations, the guess provided by the auxiliar thermodynamic model will be an essential and useful guide if the model is reliable enough, as it is the case here.

Once both boxes have equilibrated separatedly, an inhomogeneous biphasic simulation box is constructed assembling, in the $z$ direction, the simulation box with the denser phase in the middle, to optimize CPU time, and two replicas of the other box at both ends, by simply displacing the appropriate value of the $z$ coordinate. Then, this biphasic simulation box is allowed to evolve at constant temperature and volume ($NVT$) conditions until two parallel explicit interfaces are fully equilibrated. The $NPT$ and $NVT$ Monte Carlo simulations were organized in cycles. Each cycle consists in $N$ ($N$ standing for the total number of molecules in the box) attempts to either displace or rotate a randomly chosen molecule (both movements with equal probability), plus one volume change try in the case of bulk $NPT$ calculations. The ac-

ceptance ratios for translational, rotational moves and volume changes were adjusted along the run to approximately 30%. After the initial equilibration period,consisting in approximately $10^6$ cycles, we generated between $2 \times 10^6$ cycles to accumulate averages of the desired interfacial properties.

The interfacial density profile and coexisting phase densities were averaged dividing the box in 100 identical parallel slabs in the $z$ direction. Also, the center of mass of the simulation box was fixed at the center of the box to avoid profile fluctuations. Minimum image convention and fully periodic boundary conditions were considered as usual. Excluding the interface, coexisting phase densities were computed as the average of the 25 central slabs in each phase using the final density profile.

The surface tension was computed using two methods: the mechanical and thermodynamic routes. In the first case, the interfacial tension is calculated determining the pressure components through the perturbative method proposed by de de Miguel and Jackson[66]. In the second case, the Test-Area (TA) technique proposed by Gloor et al.[63], was used to determine the interfacial tension. The TA method has been applied by different authors to determine the vapour-liquid interfacial properties of several water models[1,129], binary fuid mixtures[70], and recently it has been used to determine the solid-fuid interfacial tension of a confined LJ fuid[139]. The uncertainty of the determined properties were obtained by the usual block averaging technique.

In the case of triphasic phase equilibrium phases methodology followed is

nearly the same, with only minor changes. In the first step, three independent simulation boxes were equilibrited with the corresponding number of molecules of each fluid. In the second step, a small change is introduced in the construction of the inhomogeneous triphasic simulation box. This box was constructed by assembling four, instead of three, equilibrated boxes. Therefore, one of the boxes, corresponding to the vapour phase that coexists with the two other liquid phases, was replied at both ends in the $z$ direction, because the three coexisting phases must be in direct mutual contact, and at the same time periodic boundary conditions have to be considered.

## 8.4 Results

### 8.4.1 $H_2O + CO_2$

The simulation technique that consider byphasic boxes with contact between the coexisting phases has the advantage of providing direct access to the structure of the interface, allowing the simultaneous determination of bulk coexistence properties (densities of the present phases), interfacial properties, and microscopic structural properties as density profiles across the interface etc. As an example, Fig. 8.1 shows the density profile shape of $H_2O + CO_2$ binary mixture across a single interface at 298.15 K and two different pressures: 2 MPa and 8 MPa. The water density profile increases monotonically across the interface with the traditional *tanh* shape, and no change in its shape is

observed with increasing pressure. However, the density of $CO_2$ presents an adsorption peak located on the $CO_2$-rich side of the interface due to the low solubility of $CO_2$ in the $H_2O$-rich phase at these pressure and temperature conditions. This behavior is in agreement with the observed by Miqueu et al.[70] and Biscay et al.[158] for the case of $CH_4$ + $H_2O$ mixture, and mixtures made up of hydrocarbon with $N_2$, $CO_2$ or $CH_4$[149].

Fig. 8.1 also serves to illustrate the effect of the treatment of the long range corrections (LRCs) to the intermolecular potential on the interface structure. Although the coulombic interactions are predominant for these models if compared with the dispersive Lennard-Jones (LJ) interactions, a recent work[302] has shown that interfacial properties are very sensitive to the rigorous treatment of LJ LRCs. In this work, the Coulombic interactions have been treated with the Reaction Field method[129], and the Janeček method[111], in the formulation of Blas and MacDowell,[119], was used to deal with dispersive interactions. Fig. 8.1a shows the performance of this combined treatment, that results in a good agreement with the mixture density profiles across the interface determined using an alternative theoretical approach, the Gradient Theory, as published by Lafitte *et al.*[131]. With this setting, MC and GT profiles equilibrium bulk density values agree very well to each other, and although MC profiles show the cited $CO_2$ adsorption at the interface, the height of this peak is underestimated when compared with the GT profile. On the otehr hand, the use of a pure truncation of the LJ potential and no further treatment of

LRCs results in a different estimation of interfacial mixture density profiles, in the same direction of the case of pure liquid vapour interfacial properties shown in the previous work[302].

Fig. 8.2 depicts the density profiles of the gas $CO_2$/ liquid $H_2O$ interface just below the saturation pressure of $CO_2$ at 287 K. We have decided to explore these thermodynamic conditions because they evidence interesting phenomena from a fundamental point of view. As shown, $CO_2$ accumulates creating a thin liquid film that perfectly wets the interface with the liquid $H_2O$. As pressure increases, this adsorbed layer grows thicker continuously just below the saturation pressure of $CO_2$. This represents a prewetting transition[299], which means that $T_{cw} < T < T_c$, $T_{cw}$ representing the critical wetting temperature. Here, $CO_2$ density profiles obtained using inhomogeneous LRCs provide also the best agreement with those obtained with GT[131]. This result demonstrates that LRCs are essential to compute accurately not only the $CO_2$ inferfacial behavior, but the phase equilibria itself, as Fig. 8.2 shows that the pure truncation of the potential leads to an incorrect location of the saturation transition of $CO_2$.

The MC interfacial tension results are plotted in Fig.8.3, against those computed by GT[131], and the experimental values[308] at 298.15 K and 287 K. MC interfacial tensions were computed using Test-Area[63] and de Miguel and Jackson[66] methods. As equivalent interfacial tension values were obtained, only TA values were plotted in Fig.8.3 for clarity. The agreement between

MC values, experimental and theoretical values is satisfactory, as shown in this plot. Nevertheless, interfacial tension is much more sensitive to LRCs in the prewetting transition conditions, if compared to liquid-liquid or vapor-liquid equilibria, as shown in Fig.8.3b. This is in agreement with the fact that the $CO_2$ vapor-liquid phase transition at 287 K was only adequately estimated using LRCs in MC simulations. Interfacial tension values computed using inhomogeneous LRCs are in this case in much better agreement with both GT and experimental values.

### 8.4.2 $H_2O + CO_2 + CH_4$

Once we have analyzed using MC simulation the interfacial behavior of $CH_4 + H_2O$[70] and $CO_2 + H_2O$ binary mixtures, the next objective is to analize the interfacial behaviour of the ternary mixture. As described in detail in a previous work[130], the global phase diagram of this mixture is rather complex. This is a combination of the type $III$ behaviour, according to the classification of Scott and van Konynenburg[209], of the two binary mixtures containing $H_2O$, and the type $I$ $CH_4 + CO_2$ binary. Now, using again the SAFT-VR phase diagram analysis of the ternary mixture as guiding tool the interfacial properties and fluid phase equilibria of this ternary mixture will be analyzed, considering different types of interfacial behaviour, and including the triphasic liquid-liquid-vapour (LLV) conditions, for the difficulties associated to the description of this elusive region. The phase behavior of the

ternary system is dominated at high pressures by relatively large LL immiscibility regions, as shown Fig. 8.4a. The topology of the phase diagram at these thermodynamic conditions is characterized by a two-phase LL coexistence region, with one $H_2O$-rich liquid phase, whose composition is nearly constant ($x_{H_2O} \approx 0.999$), and another liquid phase without $H_2O$, whose composition varies continuously from a $CO_2$-rich liquid phase ($x_{CO_2} \approx 0.999$) to a $CH_4$-rich liquid phase ($x_{CH_4} \approx 0.999$).

At higher temperature and pressure conditions, as for instance 550K and 30 MPa (Fig. 8.4b), the two-phase LL immiscibility region shrinks, as shown Fig. 8.4b. As a result ot this reduction, there is a new $H_2O$-poor liquid phase whose water composition varies between $x_{H_2O} \approx 0.3 - 0.4$ whereas $CO_2$ and $CH_4$ composition changes inversely between $x_{CO_2,CH_4} \approx 0.7 - 0.3$. On the contrary, the phase envelope corresponding to the $H_2O$-rich liquid phase remains essentially at the same position in the triangular phase diagram.

Fig. 8.4c despicts the triangular diagram of the $H_2O + CO_2 + CH_4$ ternary mixture at 275 K and 6.3 MPa. Now, the topology of the phase diagram is completely different than that shown in Fig. 8.4a or Fig. 8.4b, since it displays one triangular central LLV three-phase region, where two liquid phases coexist in equilibrium with a vapour phase. The compositions of each phase are defined by the coordinates of the central triangle in the phase diagram: the $H_2O$-rich liquid phase is composed of nearly pure $H_2O$ ($x_{H_2O} \approx 0.996$), the second liquid phase is formed by a mixture of $CO_2$ ($x_{CO_2} \approx 0.778$) and $CH_4$

($x_{CH_4} \approx 0.210$), and the vapour phase, with a composition of $x_{CO_2} \approx 0.647$ and $x_{CH_4} \approx 0.351$). The reason to choice these three (T,P) conditions is that the interfacial behaviour is in each case different, as it will be shown later, and will serve to demonstrate the ability of the tested molecular models, and the MC technique described above, in the description of the different interfacial scenarios, and also the comparison of the location of the different phase equilibria boundaries with the results provided by the SAFT-VR model.

$H_2O + CO_2 + CH_4$ density profiles across the interface computed by MC molecular simulation at 298.15 K and 10 MPa, are plotted in Fig. 8.5. The three profiles correspond to the tie lines depicted in Fig. 8.4a. The first comment to be noted is that the MC simulation provides an excellent coincidence with the estimation of the phase behavior obtained from SAFT-VR, as the equilibrium conditions and composition of the coexisting phases are very close to each other. In all three cases, a $H_2O$-rich liquid phase composed almost of pure water coexists with one waterless phase whose composition varies between: Fig. 8.5a ($x_{CH_4} \approx 0.3$ and $x_{CO_2} \approx 0.7$), Fig. 8.5b ($x_{CH_4} \approx 0.5$ and $x_{CO_2} \approx 0.5$) and Fig. 8.5c ($x_{CH_4} \approx 0.7$ and $x_{CO_2} \approx 0.3$). Water density profile increases monotonically across the interface with the traditional *tanh* shape, as it would appear in a typical pure fluid liquid-vapour interface. However, the densities of $CO_2$ and $CH_4$ present an adsorption peak located on the other phase side, due to the low solubility of the coexisting phases at these pres-

sure and temperature conditions. The $CO_2$ preferential adsorption peak is much higher than that of $CH_4$, because of $H_2O$ molecules are more likely to associate with $CO_2$ than with $CH_4$.

Fig. 8.6 shows the profiles across the interface for the mixture at 550 K and 30 MPa, at the concentrations corresponding to the two tie lines in Fig. 8.4b. In these high-pressure conditions the mixture shows phase equilibria between a $H_2O$-rich phase and a $H_2O$-poor phase. Fig. 8.6a corresponding to $x_{CH_4} \approx 0.4$, $x_{CO_2} \approx 0.3$, $x_{H_2O} \approx 0.3$, and Fig. 8.6b to $x_{CH_4} \approx 0.3$, $x_{CO_2} \approx 0.4$, $x_{H_2O} \approx 0.3$. Now, contrarily to the case shown in Fig. 8.5, only a very slight adsorption of $CO_2$ is shown in the interface, and the LL equilibria is obtained with all the profiles approaching the *tanh* shape. The difference between the first case shown is to be underlined here.

Finally, MC simulation is able to reproduce the triphasic LLV phase equilibrium of this ternary mixture, predicted by SAFT-VR at conditions around 275K and 6.3 MPa, as shown Fig. 8.7. In this figure, we can see the three phase coexistence, corresponding to the three vertex of the triangle plotted in Fig. 8.4c: i) a $H_2O$-rich liquid phase composed of nearly pure water, ii) a $CO_2$-rich liquid phase composed by $CO_2$ and $CH_4$, and iii) one $CO_2$-rich vapor phase also constitued by $CO_2$ and $CH_4$.There is an excelent agreement between MC simulations and the mole fractions of the three phases predicted by SAFT-VR. Within the simulation box, the vapour phase was replied at both ends in the $z$ direction, in order to reproduce the direct contact between

the coexisting phases and respect the periodic boundary conditions.

## 8.5 Conclusions

In this work, MC molecular simulations was applied to reproduce the coexistence fluid phases and interfacial properties of two different mixtures: $CO_2 + H_2O$ binary mixture and $CO_2 + H_2O + CH_4$ ternary mixture. MC molecular simulation provides an accurately description of the $CO_2 + H_2O$ interfacial tension and interfacial density profiles of each component across the interface according to theorical and experimental predictions, which confirms the consistency of this method.

Finally, MC molecular simulations was applied to describe the interfacial behavior of the $CO_2 + H_2O + CH_4$ ternary mixture, using preliminary SAFT-VR information. Coexistence fluid phases were examinated across of interfacial density profiles of each component at different thermodynamic conditions. A nearly systematic adsorption of $CH_4$ and $CO_2$ in the interface is observed an varies with pressure.

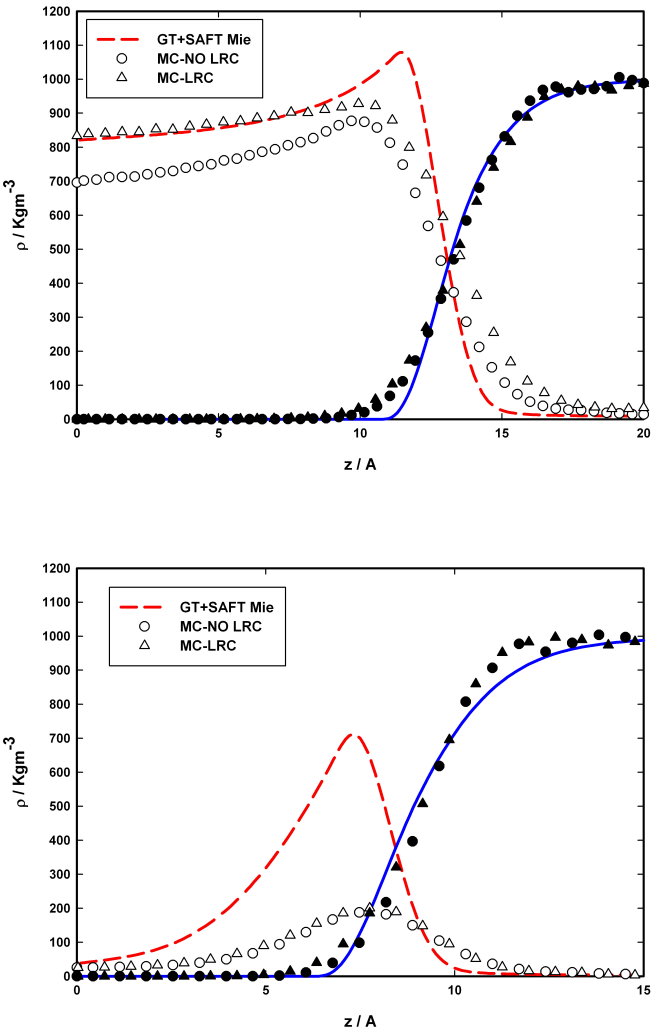


Figure 8.1: Density profiles across the interface (liquid-liquid region) for $H_2O/CO_2$ mixture at 298.15 K and (a) 2 MPa, (b) 10 MPa: (continuous curve) $H_2O$ (GT), (dashed curve) $CO_2$ (GT), (filled circles) $H_2O$ (MC-NO LRC), (filled triangles) $H_2O$ (MC-NO LRC), (open circles) $CO_2$ (MC-NO LRC), (open triangles) $CO_2$ (MC-LRC).

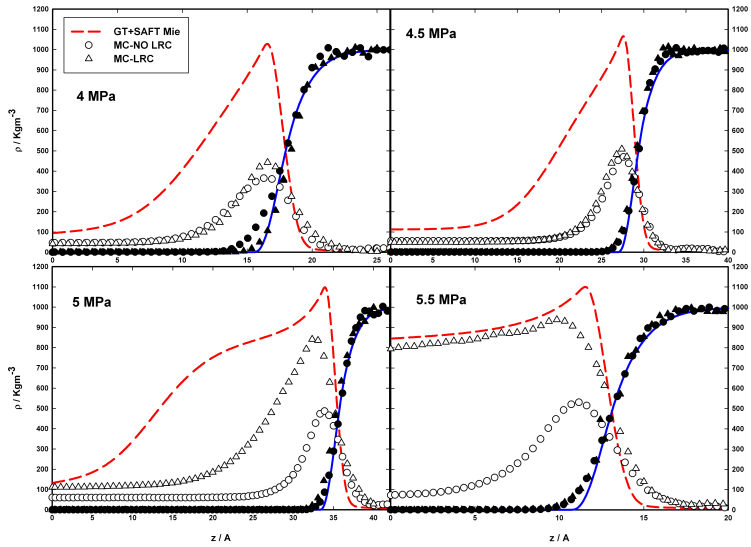


Figure 8.2: Methane density profile at the $H_2O/CO_2$ interface (gas-liquid region close to the three-phase line) at T = 287 K and (a) P=4 MPa, (b) 4.5MPa, (c) P=5 MPa, (d) 5.5 MPa. Same legend details that Fig. 8.1.

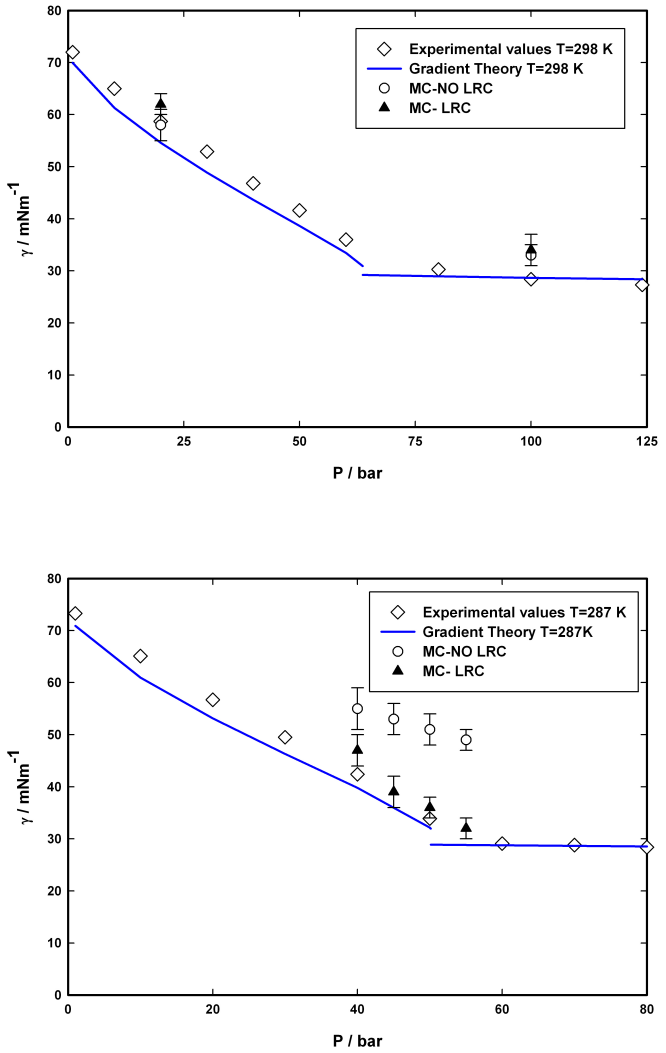


Figure 8.3: Interfacial tension versus pressure for $H_2O$ + $CO_2$ mixture at (a) 298.15 K and (b) 287 K: (continuous curve) GT prediction, (open circles) MC-NO LRC calculations, (filled triangles) MC-LRC calculations, (open diamonds) experimental data.

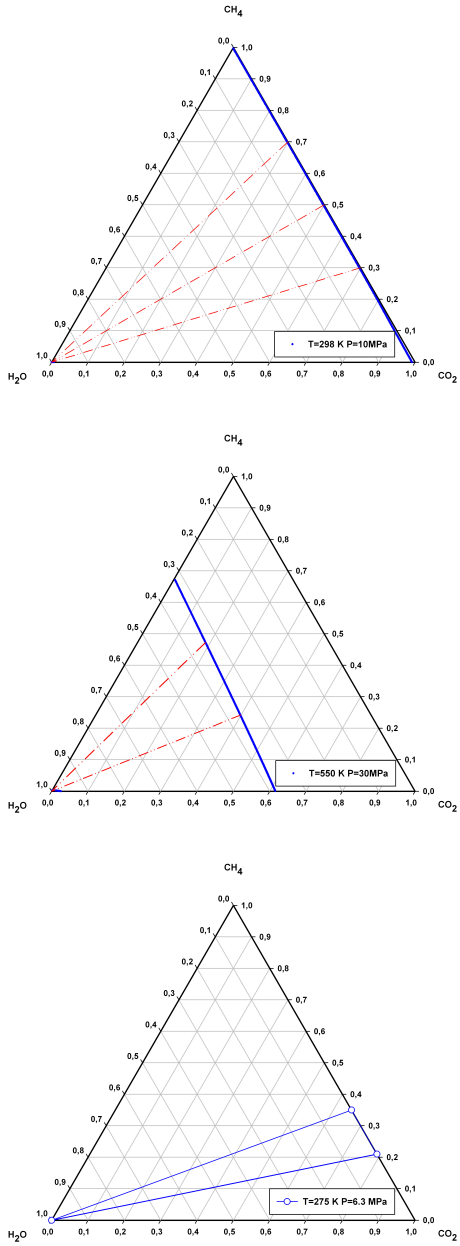


Figure 8.4: Ternary phase diagram of the mixture $H_2O$ + $CO_2$ + $CH_4$ obtained from SAFT-VR predictions at different temperatures and pressures: (a) T=298.15 K P=10 MPa, (b) T=550 K P=30 MPa, (c) T=275 K P=6.3 MPa

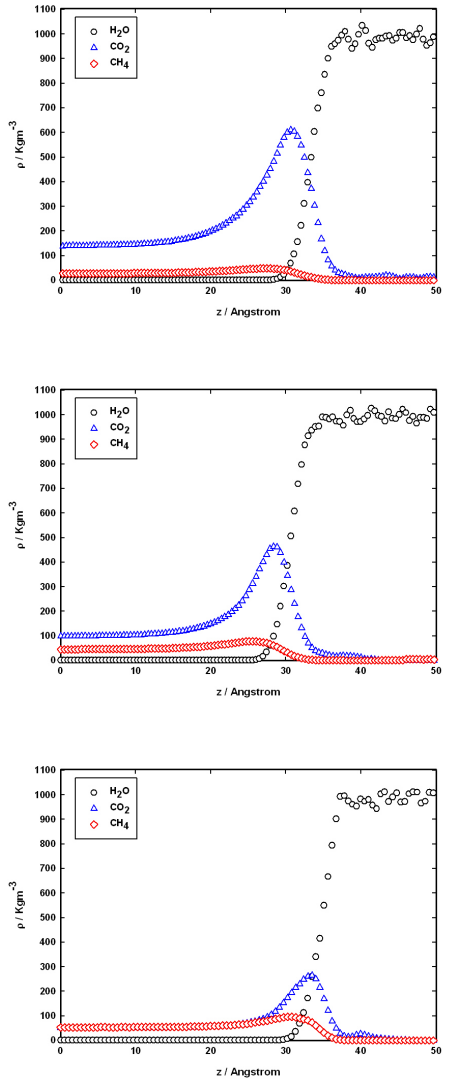


Figure 8.5: Density profiles across the interface for $H_2O/CO_2/CH_4$ mixture at 298.15 K and 10 MPa. The system exhibits the equilibrium of two fluid phases: one phase composed of pure water and other phase consisting of different $CO_2$ and $CH_4$ composition (a) $x_{CH_4} \approx$ 0.3 and $x_{CO_2} \approx$ 0.7, (b) $x_{CH_4} \approx$ 0.5 and $x_{CO_2} \approx$ 0.5, (c) $x_{CH_4} \approx$ 0.7 and $x_{CO_2} \approx$ 0.3

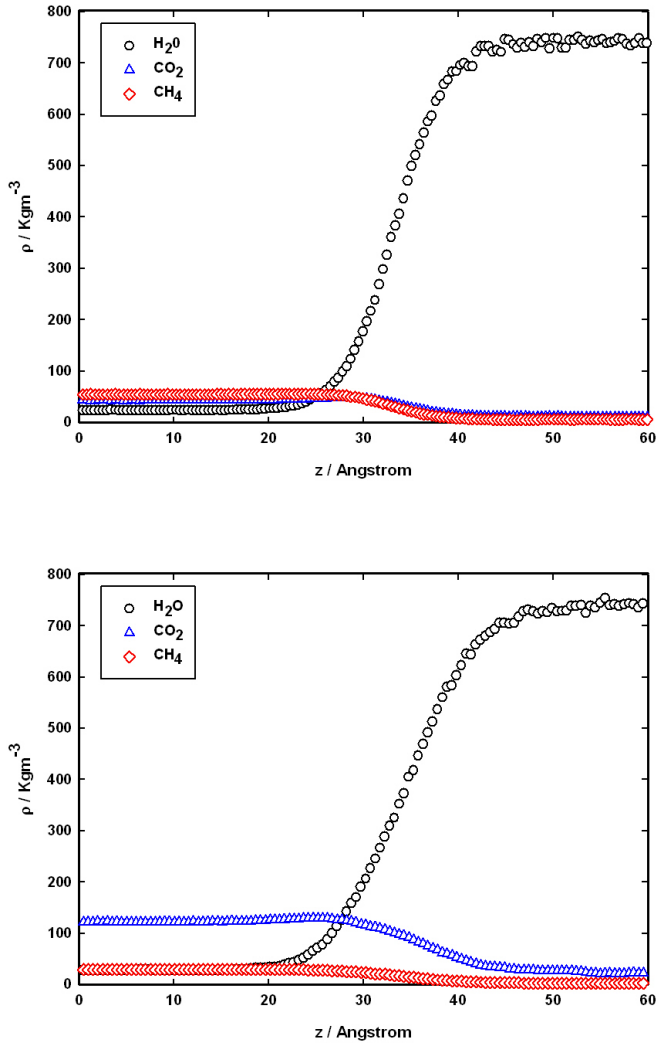


Figure 8.6: Density profiles across the interface for $H_2O/CO_2/CH_4$ mixture at 550 K and 30 MPa. The system exhibits the equilibrium of two fluid phases: one $H_2O$-rich phase and one $H_2O$-poor phase whole simulated compositions was (a)$x_{CH_4} \approx 0.4$, $x_{CO_2} \approx 0.3$, $x_{H_2O} \approx 0.3$ , (b)$x_{CH_4} \approx 0.3$, $x_{CO_2} \approx 0.4$, $x_{H_2O} \approx 0.3$.

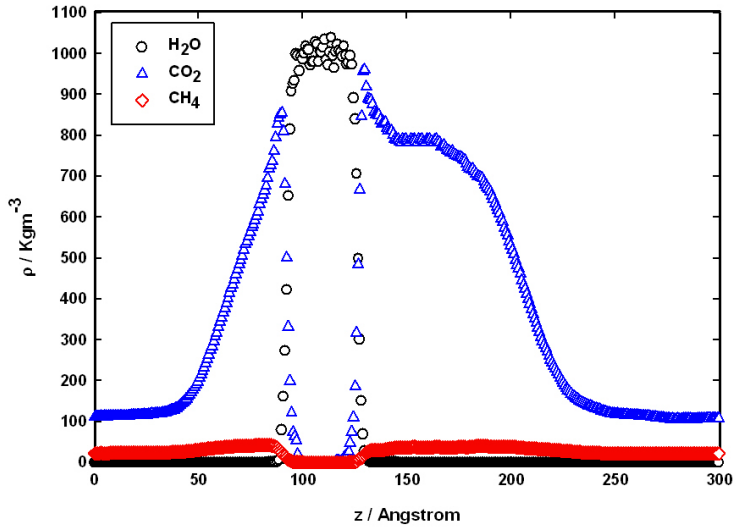


Figure 8.7: $H_2O/CO_2/CH_4$ density profiles with triphasic liquid-liquid-vapour coexistence at 275 K and 6.3 MPa.

# Chapter 9

# Conclusiones

El objetivo principal de este trabajo era determinar las propiedades interfaciales de fluidos involucrados en la extracción de gas natural desde depósitos no convencionales, en particular metano, agua y dióxido de carbono, usando el método de simulación molecular de Monte Carlo. Se consideró de entre las opciones posibles la simulación de coexistencia directa de fases con interfase explícita. Se han utilizado modelos moleculares rígidos no polarizables, en los que las interacciones intermoleculares se calculan como adición de interacción entre sitios que representan cada átomo, donde se incluye un término dispersivo modelado a través de potencial de interacción Lennard-Jones, y cargas eléctricas puntuales aisladas.

Evaluando los resultados expuestos a lo largo de esta memoria, pueden extraerse en primer lugar una serie de conclusiones sobre la metodología de cálculo.

- El método de campo de reacción es una alternativa de gran utilidad para tratar el efecto de las interacciones coulombianas entre cargas eléctricas en este tipo de simulaciones. Se ha verificado determinando propiedades interfaciales para diversos modelos de agua, y comparando de forma cuantitativa los resultados con los obtenidos mediante el método de las sumas de Ewald, que resultan mucho más costosas desde el punto de vista computacional.

- Se ha demostrado que para obtener valores precisos de propiedades interfaciales, como la tensión interfacial, mediante la técnica de cálculo citada, es preciso calcular con rigor las correcciones de largo alcance también para el término de interacción dispersivo. Se ha ensayado la metodología propuesta por Blas y MacDowell para este cálculo, aplicada al caso de metano, agua y dióxido de carbono puros. Se determinó la tensión interfacial tanto por la ruta termodinámica usando el método del Test-Area, como por la ruta mecánica calculando las componentes del tensor de presiones. Los resultados obtenidos por las distintas rutas son consistentes si el tratamiento de las correcciones de largo alcance es el correcto.

- Se ha extendido el método de cálculo de la tensión interfacial conocido como Test-Area al colectivo termodinámico Gran Canónico. Se ha comprobado el método determinando la tensión interfacial de un fluido

Lennad-Jones confinado entre paredes plano paralelas interaccionantes, contrastando los resultados con los obtenidos mediante otras técnicas posibles.

Una vez establecidas las condiciones de cálculo óptimas, fijando la metodología empleada de forma rigurosa, se han realizado cálculos para diversos sistemas, obteniéndose las siguientes conclusiones:

- En primer lugar se ha mostrado la capacidad de la metodología de simulación molecular puesta a punto para determinar propiedades interfaciales de metano, agua y dióxido de carbono puros en situación de confinamiento, en poros planos interaccionantes. Se han analizado perfiles de densidad, coeficientes de adsorción, o tensión interfacial.

- A la hora de plantear el estudio de propiedades interfaciales de mezclas, se ha puesto de manifiesto que es fundamental contar con un modelo molecular termodinámico preciso que permita estimar las condiciones iniciales de la simulación. Este conjunto de variables de entrada debe incluir una estimación precisa de temperatura, presión, tipo de equilibrio y composición de fases coexistentes. En este caso se ha probado que la ecuación de estado SAFT-VR es una elección óptima, ya que permite estimar el complejo diagrama de fases ternario de la mezcla ternaria objeto de estudio. Se ha analizado en detalles este diagrama estimado en amplias regiones de presión y temperatura, comparando de forma

exhaustiva con la información experimental disponible. Se ha constatado que sin la ayuda de un modelo macroscópico robusto y fiable es muy improbable conseguir el equilibrado mediante simulación molecular de las fases coexistentes y por tanto la determinación de las propiedades interfaciales buscadas.

- La metodología expuesta, que combina la determinación del equilibrio de fases mediante la ecuación de estado SAFT-VR, y el uso de esta información para construir las cajas de simulación molecular, se ha revelado muy efectivo en el cálculo de propiedades interfaciales de mezclas binarias de metano, agua y dióxido de carbono. En distintas condiciones de presión y temperatura se ha mostrado que los modelos moleculares citados describen con detalle comportamientos como equilibrio entre fases fluidas sin adsorción, equilibrios con adsorción preferencial en la interfase, o transiciones de tipo prewetting. Se ha comparado la física en varios casos con la descrita por otra teoría de fluidos inhomogéneos, la Teoría del Gradiente combinada con una ecuación de estado SAFT-VR. La correspondencia entre ambas perspectivas debe ser puesta de manifiesto.

- Por último, esta metodología de cálculo es aplicable también al caso de propiedades interfaciales de mezclas multicomponentes generalizadas, habiéndose aplicado en este caso a la mezcla ternaria objeto de estudio.

En estas condiciones, se ha conseguido obtener una descripción incluso de las condiciones de equilibrio trifásico, mediante el equilibrado de dos fases líquidas y una gaseosa coexistiendo en una única caja de simulación.

Estas conclusiones muestran la versatilidad y aplicabilidad de las técnicas de cálculo de simulación molecular de Monte Carlo ensayadas para el caso de la aplicación práctica que motivó este estudio, la determinación precisa de propiedades interfaciales en fluidos complejos involucrados en la extracción de gas natural desde depósitos no convencionales.

# References


[1] C. Vega and E. de Miguel. *J. Chem. Phys.*, 126:154707, 2007. xi, 37, 48, 50, 55, 56, 57, 58, 80, 87, 101, 111, 132, 135, 206, 207, 235, 239

[2] A. J. Apelblat. *J. Chem. Thermodyn.*, 31:869, 1999. xiv, 168, 169, 171

[3] F. Keyes. *J. Mech. Eng. Sci.*, 53:132, 1931.

[4] I. M. Abdulagatov. *J. Chem. Thermodyn.*, 29:1387, 1997.

[5] I. M. Abdulagatov. *J. Chem. Eng. Data*, 43:830, 1998.

[6] W. J. Gildseth. *J. Chem. Eng. Data*, 17:402, 1972.

[7] N. S. Osborne. *J. Res. Nat. Bur. Std.*, 10:155, 1933.

[8] D. R. Douslin and A. Osborn. *J. Sci. Instr.*, 42:369, 1965.

[9] A. Egerton. *Philos. Trans. R. Soc. Lond. Ser. A*, 231:147, 1932.

[10] L. Besley. *J. Chem. Thermodyn.*, 5:397, 1973. xiv, 168, 169, 171

[11] C. F. Jenkin and D. R. Pye. *Philos. Trans. R. Soc. Lond. Ser. A*, 213:67, 1914. xiv, xv, 168, 169, 189

[12] J. Sengers, H. Levelt, and W. T. Chen. *J. Chem. Phys.*, 56:595, 1972.

[13] C. H. Meyers and M. S. van Dusen. *J. Res. Nat. Bur. Std.*, 10:281, 1933.

[14] L. A. Webster and A. J. Kidney. *J. Chem. Eng. Data*, 46:759, 2001.

[15] J. G. Harris and K. H. Yung. *J. Phys. Chem.*, 99:12021, 1995. 73, 74, 134, 235

[16] P. Nowak, T. Tielkes, R. Kleinrham, and W. Wagner. *J. Chem. Thermodyn.*, 29:885, 1997. xiv, xv, 168, 169, 189

[17] K. Toedheide and E. U. Franck. *Z. Phys. Chem. NF.*, 37:387, 1963. xiv, 168, 169

[18] S. Takenouchi and G. C. Kennedy. *Am. J. Sci.*, 262:1055, 1964. xiv, 168, 169

[19] A. Valtz, A. Chapoy, C. Coquelet, P. Paricaud, and D. Richon. *Fluid Phase Equilib.*, 226:333, 2004. xiv, 156, 160, 168, 169

[20] B. D. Smith and R. Srivastava. *Physical Science Data: Thermodynamic Data for Pure Componentes, Part A: Hydrocarbons and Ketones.* Elsevier, 1986. xiv, xv, 171, 189

[21] R. G. Sultanov, V. G. Skripka, and A. Y. Namiot. *Zhurnal Fizicheskoi Khimii*, 46:2160, 1972. xiv, xv, 170, 171, 188

[22] H. Welsch. PhD thesis, University of Karlsruhe, 1973.

[23] E. Brunner. *J. Chem. Thermodyn.*, 22:335, 1990.

[24] V. M. Shmonov, R. J. Sadus, and U. Franck. *J. Phys. Chem.*, 97:9054, 1993. xiv, xv, 170, 171, 188

[25] D. A. Fletcher, R. F. McMeeking, and D. Parkin. *J. Chem. Inf. Comput. Sci.*, 36:746, 1996. xv, 172, 188

[26] H. G. Donnelly and D. L. Katz. *Ind. Eng. Chem.*, 46:511, 1954. xv, xvi, xix, 157, 173, 189, 190, 194

[27] M. S. W. Wei, T. S. Brown, A. J. Kidnay, and E. D. Sloan. *J. Chem. Eng. Data*, 40:726, 1995. xvi, xix, 173, 190, 194

[28] F. A. Somait and A. J. Kidnay. *J. Chem. Eng. Data*, 23:301, 1978. xvi, xix, 173, 190, 194

[29] J. F. Qin, R. J. Rosenbauer, and Z. Duan. *J. Chem. Eng. Data*, 53:1246, 2008. xvi, 158, 191

[30] G. Wiegand and E. U. Franck. *Phys. Chem. Chem. Phys.*, 98:809, 1994. xx, 214, 215, 222

[31] C. Jho, D. Nealon, S. Shogbola, and A. D. J. King. *J. Colloid Interface Sci.*, 65:141, 1978. xx, 222

[32] W. Sachs and V. Meyn. *Colloids Surf. A*, 94:291, 1995. xx, 214, 222

[33] Q. Y. Ren, G. J. Chen, W. Yan, and T. M. Guo. *J. Chem. Eng. Data*, 45:610, 2000. xx, 214, 222

[34] F. Biscay, A. Ghoufi, F. Goujon, V. Lachet, and P. Malfreyt. *J. Chem. Phys.*, 130:184710, 2009. xx, 63, 80, 111, 217, 222

[35] *World Energy Outlook*. Energy Information Administration, 2011. 6

[36] S. A. Holditch. *J. P. T.*, 58:86, 2006. 7

[37] *Tight Gas Reservoirs: Technology Intensive Resources. Exploration and Production*. Total Know-How Series, 2007. 8

[38] *Unconventional Gas*. National Petroleum Council Global Oil and Gas Study, 2007. 8

[39] E. C. Donaldson and D. Tiab. $2^{nd}$*Ed.Petrophysics: Theory and Practice of Measuring Reservoir Rock and Fluid Transport Properties*. Elsevier, 2004. 8

[40] S. M. Thompson, K. E. Gubbins, J. P. R. B. Walton, R. A. R. Chantry, and J. S. A. Rowlinson. *J. Chem. Phys.*, 81:603, 1984. 14

[41] N. Metropolis. *Los Alamos Science*, 12:125, 1987. 15

[42] N. Metropolis and S. Ulam. *J. Am. Stat. Assoc.*, 44:335, 1949.

[43] N. Metropolis, A.W. Rosenbluth, M. N. Rosenbluth, A. H. Teller, and E. Teller. *J. Chem. Phys.*, 21:1087, 1953. 16, 17, 23

[44] B. J. Alder and T. E. Wainwright. *J. Chem. Phys.*, 31:459, 1959. 15

[45] E. Segre. *From X-Rays to Quarks*. W. H. Freeman & Co., 1980. 15

[46] L. Kelvin. *Philos. Mag.*, 2:1, 1901. 15

[47] M. P. Allen and D. J. Tildesley. *Computer Simulation of Liquids*. Clarendon Press, 1987. 20, 22

[48] D. Frenkel and B. Smit. *Understanding Molecular Simulation*. Academic Press, 2002. 20, 22, 48, 78, 115

[49] D. P. Landau and K. Binder. *A Guide to Monte Carlo Simulations in Statystical Physics, 2nd ed.* Cambridge, 2005. 20

[50] R. J. Sadus. *Molecular simulation of fluids: theory, algorithms, and object-orientation*. Elsevier, 1999. 20

[51] *The Art of molecular dynamics simulation*. Cambridge Univ. Press, 2005. 20

[52] D. M. Heyes. *The Liquid state: applications of molecular simulations.* Wiley, 1998. 20

[53] P. Ungerer, B. Tavitian, and A. Boutin. *Applications of molecular simulation in the oil and gas industry: Monte Carlo methods.* Technip, París, 2005. 20

[54] J. M. Thijssen. *Computational Physics.* Cambridge Univ. Press, 2003. 20

[55] W. Krauth. *Statistical Mechanics: Algorithms and Computations.* Oxford Univ. Press, 2006. 20

[56] D. Möller and J. Fischer. *Mol. Phys.*, 69:463, 1990. 26

[57] A. Z. Panagiotopoulos. *Mol. Phys.*, 61:812, 1987. 26

[58] K. S. Liu. *J. Chem. Phys.*, 60:4226, 1974. 27, 237

[59] A. Gil-Villegas, A. Galindo, P. J. Whitehead, S. J. Mills, G. Jackson, and A. N. Burgess. *J. Chem. Phys.*, 106:4168, 1997. 31, 156, 161, 162, 163, 212, 232, 237

[60] D. Henderson. *Fundamentals of Inhomogeneous Fluids.* Marcel Dekker, Inc., 1992. 34

[61] J. S. Rowlinson and B. Widom. *Molecular Theory of Capillarity.* Dover Pub., 1982. 34

[62] P. G. de Gennes, F. Brochard-Wyart, and D. Quéré. *Capillarity and Wetting Phenomena: Drops, Bubbles, Pearls, Waves*. Springer, 2004. 34

[63] G. J. Gloor, G. Jackson, F. J. Blas, and E. de Miguel. *J. Chem. Phys.*, 123:134703, 2005. 34, 35, 48, 54, 79, 101, 102, 104, 105, 111, 119, 132, 134, 136, 137, 140, 205, 209, 239, 242

[64] L. G.MacDowell and P. Bryk. *Phys. Rev. E*, 75:061609, 2007. 34, 48, 101, 132, 205

[65] E. de Miguel. *J. Phys. Chem. B*, 112:4674, 2008. 34, 48, 101, 111, 132, 205

[66] E. de Miguel and G. Jackson. *J. Chem. Phys.*, 125:164109, 2006. 35, 38, 54, 79, 111, 134, 137, 209, 239, 242

[67] J. H. Irving and J. G. Kirkwood. *J. Chem. Phys.*, 18:817, 1950. 35, 39, 105, 115

[68] F. J. Blas, L. G. MacDowell, E. de Miguel, and G. Jackson. *J. Chem. Phys.*, 129:144703, 2008. 37, 48, 80, 101, 111, 132, 206

[69] C. Ibergay, A. Ghoufi, F. Goujon, P. Ungerer, A. Boutin, B. Rousseau, and P. Malfreyt. *Phys. Rev. E*, 75:051602, 2007. 37, 52, 63, 140

[70] C. Miqueu, J. M. Míguez, M. M. Piñeiro, T. Lafitte, and B. Mendiboure.

*J. Phys. Chem. B*, 115:9618, 2011. 37, 73, 80, 100, 101, 132, 233, 234, 235, 237, 239, 241, 243

[71] C. Miqueu, B. Mendiboure, A. Graciaa, and J. Lachaise. *J. Fuel*, 87:612, 2008. 42, 204

[72] J. R. Errington and D. A. Kofke. *J. Chem. Phys.*, 127:174709, 2007. 48, 205

[73] G. Galliero, M. M. Piñeiro, B. Mendiboure, C. Miqueu, T. Lafitte, and D. Bessières. *J. Chem. Phys.*, 130:104704, 2009. 48, 80, 100, 101, 132, 140, 204

[74] P. ç, Y. Reyes-Mercado, and Y. Duda. *Phys. Lett. A*, 372:7024, 2008. 48, 80, 101, 132, 206

[75] U. Essmann, L. Perera, M. L. Berkowitz, T. Darden, H. Lee, and L. G. Pedersen. *J. Chem. Phys.*, 103:8577, 1995. 48

[76] L. Onsager. *J. Am. Chem. Soc.*, 58:1486, 1936. 49

[77] J. A. Barker and R. O. Watts. *Discuss. Faraday Soc.*, 53:161, 1972. 49

[78] J. A. Barker and R. O. Watts. *Mol. Phys.*, 28:1069, 1974.

[79] R. O. Watts. *Mol. Phys.*, 28:1069, 1974.

[80] M. Neumann and O. Steinhauser. *Mol. Phys.*, 39:437, 1980.

[81] M. Neumann. *Mol. Phys.*, 50:841, 1983.

[82] M. Neumann, O. Steinhauser, and G. S. Pauley. *Mol. Phys.*, 52:97, 1984.

[83] M. Neumann. *J. Chem. Phys.*, 82:5663, 1985. 49, 52, 53, 137

[84] M. Neumann. *J. Chem. Phys.*, 85:1567, 1986.

[85] I. P. Omelyan. *Phys. Lett. A*, 223:295, 1996. 49

[86] I. P. Omelyan. *Com. Phys. Comm.*, 107:113, 1997.

[87] G. Hummer, D. K. Soumpasi, and M. Neumann. *Mol. Phys.*, 77:769, 1992. 49

[88] I. G. Tironi, R. Sperb, P. E. Smith, and W. F. van Gusteren. *J. Chem. Phys.*, 102:5451, 1995.

[89] P. H. Hunenberger and W. F. van Gusteren. *J. Chem. Phys.*, 108:6117, 1998.

[90] M. Bergdorf, C. Peter, and P. H. Hunenberger. *J. Chem. Phys.*, 119:9129, 2003.

[91] C. Peter, W. F. van Gusteren, and P. H. Hunenberger. *J. Chem. Phys.*, 119:12205, 2003.

[92] S. Boresch and O. Steinhauser. *J. Chem. Phys.*, 11:8271, 2003. 49

[93] T. N. Heinz and P. H. Hunenberger. *J. Chem. Phys.*, 123:034107, 2005.

[94] A. Baumketner. *J. Chem. Phys.*, 130:104106, 2009. 49

[95] X. Rozanska and C. Chipot. *J. Chem. Phys.*, 112:9691, 2000. 49

[96] M. Nina and T. Simonson. *J. Phys. Chem. B*, 106:3696, 2002. 49

[97] A. M. J. J. Bonvin, M. Sunnerhagen, G. Otting, and W. F. van Gusteren. *J. Mol. Biol.*, 282:859, 1998. 49

[98] A. Baumketner and J. E. Shea. *J. Phys. Chem. B*, 109:21322, 2005. 49

[99] S. Gnanakaran, R. Nussinov, and A. E. García. *J. Am. Chem. Soc.*, 128:2158, 2006.

[100] Y. G. Mu, L. Nordenskiold, and J. P. Tam. *Biophys. J.*, 90:3983, 2006.

[101] H. Verli, A. Calazans, R. Brindeiro, A. Tanuri, and J. A. Guimaraes. *J. Mol. Graphics Modell.*, 26:62, 2007.

[102] T. Soares, M. Christen, K. F. Hu, and W. F. van Gusteren. *Tetrahedron*, 60:7775, 2004. 49

[103] S. Murad and I. K. Puri. *Chem. Phys. Lett.*, 467:110, 2008. 49, 137

[104] S. Murad and I. K. Puri. *Chem. Phys. Lett.*, 476:267, 2009. 49, 137

[105] J. Kolafa, F. Moucka, and I. Nezbeda. *Collect. Czech. Chem. Commun.*, 73:481, 2008. 49

[106] J. L. F. Abascal and C. Vega. *J. Chem. Phys.*, 123:234505, 2005. 49, 50, 73, 74, 84, 133, 135, 207, 235

[107] J. Wang and X. C. Zeng. *J. Theor. Comput. Chem.*, 8:733, 2009. 50, 52

[108] H. J.C. Berendsen, J. R. Grigera, and T. P. Straatsma. *J. Chem. Phys.*, 91:6269, 1987. 50

[109] W. L. Jorgensen, J. Chandrasekhar, J. Madura, R. W. Impey, and M. Klein. *J. Chem. Phys.*, 79:926, 1983. 50, 73, 74

[110] H. W. Horn, W. C. Swope, J. W. Pitera, J. D. Madura, T. J. Dick, G. L. Hura, and T. Head-Gordon. *J. Chem. Phys.*, 120:9665, 2004. 50, 73, 74

[111] J. Janeček. *J. Phys. Chem. B*, 110:6264, 2006. 52, 63, 65, 67, 77, 140, 236, 241

[112] G. A. Chapela, G. Saville, S. M. Thompson, and J. S. Rowlinson. *J. Chem. Soc. Far. Trans.*, 73:1133, 1977. 63

[113] E. M. Blokhuis, D. Bedeaux, C. D. Holcomb, and J. A. Zollweg. *Mol. Phys.*, 95:665, 1995. 63

[114] M. Guo and B. C.-Y. Lu. *J. Chem. Phys.*, 106:3688, 1997. 63

[115] A. Ghoufi, F. Goujon, V. Lachet, and P. Malfreyt. *J. Chem. Phys.*, 128:154716, 2008. 63

[116] A. Ghoufi, F. Goujon, V. Lachet, and P. Malfreyt. *Phys. Rev. E*, 77:031601, 2008.

[117] F. Biscay, A. Ghoufi, F. Goujon, and P. Malfreyt. *J. Phys. Chem. B*, 112:13885, 2008.

[118] F. Biscay, A. Ghoufi, and P. Malfreyt. *J. Phys. Chem. B*, 134:044709, 2011. 63, 111

[119] L. G. MacDowell and F. J. Blas. *J. Chem. Phys.*, 131:074705, 2009. 63, 64, 65, 68, 70, 77, 140, 236, 241

[120] M. Mecke, J. Winkelmann, and J. Fischer. *J. Chem. Phys.*, 107:9264, 1997. 63

[121] M. Mecke, J. Winkelmann, and J. Fischer. *J. Chem. Phys.*, 110:1188, 1999. 63

[122] K. C. Daoulas, V. A. Harmandaris, and V. G. Mavrantzas. *Macromol.*, 23:4430, 2005. 63

[123] J. Janeček, H. Krienke, and G. Schmeer. *J. Phys. Chem. B*, 110:6916, 2006. 63, 65

[124] V. K. Shen, R. D. Mountain, and J. R. Errington. *J. Phys. Chem. B*, 111:6198, 2007.

[125] J. Janeček. *J. Chem. Phys.*, 131:124513, 2009.

[126] J. Benet, L. G. MacDowell, and C. Menduiña. *J. Chem. Eng. Data*, 55:5465, 2010. 63

[127] P. J. int Veld, A. E. Ismail, and G. S. Grest. *J. Chem. Phys.*, 127:144711, 2007. 64

[128] J. Alejandre and G. A. Chapela. *J. Chem. Phys.*, 132:014701, 2010. 64

[129] J. M. Míguez, D. González-Salgado, J. L. Legido, and M. M. Piñeiro. *J. Chem. Phys.*, 132:184102, 2010. 72, 78, 80, 101, 111, 135, 137, 208, 237, 239, 241

[130] J. M. Míguez, M. C. dos Ramos, M. M. Piñeiro, and F. J. Blas. *J. Phys. Chem. B*, 115:9604, 2011. 73, 117, 131, 209, 218, 237, 243

[131] T. Lafitte, B. Mendiboure, M. M. Piñeiro, D. Bessières, and C. Miqueu. *J. Phys. Chem. B*, 114:11110, 2010. 73, 100, 132, 157, 205, 213, 214, 215, 217, 220, 232, 241, 242

[132] D. Möller, J. Oprzynski, and J. Fischer. *Mol. Phys.*, 75:1455, 1992. 73, 74, 133, 206, 207, 234

[133] M. G. Martin and J. I. Siepmann. *J. Phys. Chem. B*, 102:2569, 1998. 73, 74, 207

[134] C. S. Murthy, K. Singer, and I. R. McDonald. *Mol. Phys.*, 44:13, 1981. 73, 74

[135] D. Möller and J. Fischer. *Fluid Phase Equilib.*, 100:35, 1994.

[136] C. S. Murthy, S. F. Oshea, and I. R. Mc Donald. *Mol. Phys.*, 50:531, 1983. 73, 74

[137] J. J. Potoff and J. I. Siepmann. *AIChE J.*, 47:1676, 2001. 73, 74, 235

[138] Z. Zhang and Z. Duan. *J. Chem. Phys.*, 122:214507, 2005. 73, 74

[139] J. M. Míguez, M. M. Piñeiro, A. I. Moreno-Ventas Bravo, and F. J. Blas. *J. Chem. Phys.*, 136:114707, 2012. 80, 239

[140] U. Setzmann and W. Wagner. *J. Phys. Chem. Ref. Data*, 20:1061, 1991. 83, 87

[141] G. R. Somayajulu. *Int. J. Thermophys.*, 9:559, 1988. 85, 87

[142] W. Wagner and A. Pruss. *J. Phys. Chem. Ref. Data*, 31:387, 2002. 86

[143] *Physical Chemistry of Aqueous Systems: Proceedings of the 12th International Conference on the Properties of Water and Steam*, volume a107-a138, Orlando, Fl, 1994. 86

[144] R. Span and W. Wagner. *J. Phys. Chem. Ref. Data*, 25:1509, 1996. 90

[145] W. Rathjen and J. Straub. *Heat Transfer in Boiling.* Academic Press, 1977. 91

[146] J. W. Cahn and J. E. Hilliard. *J. Chem. Phys.*, 28:258, 1958. 100, 204

[147] B. S. Carey, H. T. Davis, and L. E. Scriven. *AIChE J.*, 26:705, 1980. 204, 211

[148] C. Miqueu, B. Mendiboure, A. Graciaa, and J. Lachaise. *Fluid Phase Equilib.*, 218:189, 2004.

[149] C. Miqueu, B. Mendiboure, A. Graciaa, and J. Lachaise. *Ind. Eng. Chem. Res.*, 44:3321, 2005. 100, 204, 217, 241

[150] R. Evans. *Density Functionals in the Theory of Nonuniform Fluids. In Fundamentals of Inhomogeneous Fluids.* Dekker, 1992. 100

[151] H. T. Davis. *Statistical Mechanics of Phases, Interfaces and Thin Films.* Wiley-VCH, 1996. 100, 210, 211

[152] Y. Rosenfeld. *Phys. Rev. Lett.*, 63:980, 1989. 101

[153] Y. X. Yu and J. Z. Wu. *J. Chem. Phys.*, 117:2368, 2002.

[154] Y. X. Yu and J. Z. Wu. *J. Chem. Phys.*, 119:2288, 2003. 101

[155] F. Llovell, A. Galindo, F. J. Blas, and G. Jackson. *J. Chem. Phys.*, 133:024704, 2010. 101, 204, 205

[156] E. de Miguel and G. Jackson. *Mol. Phys.*, 104:3717, 2006. 101, 108, 111

[157] P. E. Brumby, A. J. Haslam, E. de Miguel, and G. Jackson. *Mol. Phys.*, 109:169, 2010. 101, 111

[158] F. Biscay, A. Ghoufi, V. Lachet, and P. Malfreyt. *J. Chem. Phys.*, 131:124707, 2009. 101, 132, 202, 235, 241

[159] Y. Hamada, K. Koga, and H. Tanaka. *J. Chem. Phys.*, 127:084908, 2007. 102, 112

[160] J. K. Singh and S. K. Kwak. *J. Chem. Phys.*, 126:024702, 2007. 102

[161] S. K. Das and K. Binder. *Mol. Phys.*, 109:1043, 2011. 102

[162] L. D. Gelb, K. E. Gubbins, R. Radhakrishnan, and M. Sliwinska-Bartkowiak. *Rep. Prog. Phys.*, 62:1573, 1999. 102

[163] L. A. del Pino, A. L. Benavides, and A. Gil-Villegas. *Mol. Sim.*, 29:345, 2003. 102

[164] R. Evans. *J. Phys.: Condens. Matter*, 2:8989, 1990. 102

[165] B. Widom. *J. Chem. Phys.*, 19:563, 1963. 103, 118

[166] R. Eppenga and D. Frenkel. *Mol. Phys.*, 52:1303, 1984. 108, 111

[167] V. I. Harismiadis, J. Vorholz, and A. Z. Panagiotopoulos. *J. Chem. Phys.*, 105:8469, 1996. 108

[168] A. Oleinikova and I. Brovchenko. *Phys. Rev. E*, 76:041603, 2007. 112, 133

[169] H. Domínguez, M. P. Allen, and R. Evans. *Mol. Phys.*, 96:209, 1999. 112, 133

[170] W. A. Steele. *The Interaction of Gases with Solid Surfaces*. Pergamon, 1974. 112, 134

[171] U.S. Environmental Protection Agency. Inventory of u.s. greenhouse gas emissions and sinks: 1990-2000. Technical report, Washington, DC, 2002. 130

[172] S. Arrhenius. *Philos. Mag.*, 41:237, 1896. 130

[173] Intergovernmental Panel on Climate Change. Climate change 2001: A scientific basis, intergovernmental panel on climate change. Technical report, Cambridge, UK, 2003. 130

[174] U.S. Environmental Protection Agency. Global warning: Climate. Technical report, Washington, DC, 2002. 130

[175] Framework Convention on Climate Change. Revised guidelines for the preparation of national communications by parties included in annex i to the convention. Technical report, Geneva, 2006. 130

[176] *Economic Benefits of a Technology Strategy and R & D Program in Carbon Sequestration*, Kyoto, Japan, 2002.

[177] M. C. MacCracken. *J. Air & Waste Manage. Assoc.*, 58:735, 2008. 130

[178] C. M. White, B. R. Strazisar, E. J. Granite, J. S. Hoffman, and H. W. Pennline. *J. Air & Waste Manage. Assoc.*, 53:645, 2003. 130

[179] M. I. Hoffert, K. Caldeira, G. Benford, D. R. Criswell, C. Green, H. Herzog, A. K. Jain, H. S. Kheshgi, K. S. Lackner, and J. S. Lewis. *Science*, 298:981, 2002. 130

[180] *Technologies for $CO_2$ Emission Reduction. International Conference on Sustainable Future of the Global System*, Kyoto, Japan, 1999. 130

[181] C. Marchetti. *Nucl. Sci. Eng.*, 90:521, 1985. 130

[182] S. Bachu. *Energy Convers. Mgmt.*, 43:87, 2002. 130

[183] G. Coskuner. *J. Can. Petrol. Technol.*, 43:13, 2004. 131

[184] R. S. Lestz, L. Wilson, R. S. Taylor, G. P. Funkhouser, H. Watkins, and D. Attaway. *J. Can. Petrol. Technol.*, 46:68, 2004. 131

[185] M. Mazzotti, R. Pini, and G. Storti. *J. Supercrit. Fluids*, 47:619, 2009. 131

[186] A. Georgiadis, F. Llovell, A. Bismarck, F. J. Blas, A. Galindo, G. C. Maitland, J. P. M. Trusler, and G. Jackson. *J. Supercrit. Fluids*, 55:743, 2010. 131, 205, 232

[187] D. Bessières, S. L. Randzio, M. M. Piñeiro, T. Lafitte, and J. L. Daridon. *J. Phys. Chem. B*, 110:5659, 2006. 133, 207

[188] M. M. Piñeiro, C. A. Cerdeiriña, and M. Medeiros. *J. Chem. Phys.*, 129:014511, 2008. 133, 207

[189] P. Ungerer, C. Nieto-Draghi, V. Lachet, A. Wender, A. Di Lella, A. Boutin, B. Rousseau, and A. H. Fuchs. *Mol. Sim.*, 33:287, 2007. 133

[190] G. O. Berim and E. Ruckesntein. *J. Phys. Chem. B*, 111:2514, 2007. 133, 143

[191] B. Sweatman. *Phys. Rev. E*, 63:031102, 2001. 133, 134, 138

[192] E. A. Müller and L. D. Gelb. *Ind. Eng. Chem. Res.*, 42:4123, 2003. 133, 135

[193] G. Galliero, C. Nieto-Draghi, C. Boned, J. B. Avalos, A. D. Mackie, A. Baylaucq, and F. Montel. *Ind. Eng. Chem. Res.*, 46:5238, 2007. 133, 135

[194] L.-J. Chen. *J. Chem. phys.*, 103:10214, 1995. 137

[195] R. Evans, U. Marini, B. Marconi, and P. Tarazona. *J. Chem. phys.*, 84:2376, 1986. 138

[196] A. Trokhymchuk and J. Alejandre. *J. Chem. phys.*, 18:111, 1999. 140

[197] NIST Chemistry WebBook. Technical report. 141

[198] J. W. Schmoker. *AAPG Bull.*, 86:1993, 2002. 154

[199] T. Ahmed and P.D. McKinney. *Advanced Reservoir Engineering*. Gulf Professional Publishing, 2005. 154

[200] J. Dubessy, S. Buschaert, W. Lamb, J. Pironon, and R. Thiéry. *Chem. Geol.*, 173:193, 2001. 155

[201] N Goel. *J. Petrol. Sci. Eng.*, 51:169, 2006. 155

[202] A. Galindo, L. A. Davies, A. Gil-Villegas, and G. Jackson. *Mol. Phys.*, 93:241, 1998. 156, 161, 162, 163, 232, 237

[203] M. C. dos Ramos, F. J. Blas, and A. Galindo. *Fluid Phase Equilib.*, 261:359, 2007. 156, 168

[204] M. C. dos Ramos, F. J. Blas, and A. Galindo. *J. Phys. Chem. C*, 111:15924, 2007. 156, 168

[205] F. J. Blas and A. Galindo. *Fluid Phase Equilib.*, 194:501, 2002. 156, 160, 165, 166, 167

[206] A. Galindo and F. J. Blas. *J. Phys. Chem. B*, 106:4503, 2002. 156, 157, 160, 165, 167

[207] G. N. I. Clark, A. Haslam, A. Galindo, and G. Jackson. *Mol. Phys.*, 104:3561, 2006. 156, 160, 165, 166, 167

[208] R. L. Scott and P. H. van Konynenburg. *Discuss. Farad. Soc.*, 49:87, 1970. 156

[209] P. H. van Konynenburg and R. L. Scott. *Philos. Trans. A*, 298:495, 1980. 156, 243

[210] N. Spycher, K. Pruess, and J. Ennis-King. *Geochim. Cosmochim. Acta*, 67:3015, 2003. 156

[211] G. Pappa, C. Perakis, I. N. Tsimpanogiannis, and E. Voutsas. *Fluid Phase Equilib.*, 284:56, 2009. 157

[212] R. Sun and J. Dubessy. *Geochim. Cosmochim. Acta*, 74:1982, 2010. 157

[213] T. Lafitte, M. M. Piñeiro, J. L. Daridon, and D. Bessières. *J. Phys. Chem. B*, 111:3447, 2007. 157, 213

[214] A. Galindo, P. J. Whitehead, G. Jackson, and A. N. Burgess. *J. Phys. Chem.*, 100:6781, 1996. 157, 169

[215] A. Dhima, J.C. de Hemptinne, and J. Jose. *Ind. Eng. Chem. Res.*, 38:3144, 1999. 158

[216] C. Jarne, S. T. Blanco, M. A. Gallardo, E. Rauzy, S. Otín, and I. Velasco. *Energy Fuels*, 18:396, 2004. 158

[217] Y.-T. Seo and H. Lee. *J. Chem. Eng. Data*, 46:381, 2001. 158

[218] Z. Duan, N. Möller, and J. H. Weare. *Geochim. Cosmochim. Acta*, 56:2619, 1992. 158

[219] A. Austegard, E. Solbraa, G. de Koeijer, and M. J. Molnvik. *Chem. Eng. Res. and Des.*, 84:781, 2006. 158

[220] G. Soave. *Chem. Eng. Sci.*, 27:1197, 1972. 158

[221] G. M. Kontogeorgis, E. Voutsas, I. V. Yakoumis, and D. P. Tassios. *Ind. Eng. Chem. Res.*, 35:4310, 1996. 158

[222] W. Bol. *Mol. Phys.*, 45:605, 1982. 159

[223] I. Nezbeda, J. Kolafa, and Y.V. Kalyuzhnyi. *Mol. Phys.*, 68:143, 1989. 159

[224] B. H. Patel, P. Paricaud, A. Galindo, and G. C. Maitland. *Ind. Eng. Chem. Res.*, 42:3809, 2003. 160, 165, 167

[225] X. Ji, S. P. Tan, H. Adhidarma, and M. Radosz. *Ind. Eng. Chem. Res.*, 44:8419, 2005. 160

[226] J. P. Hansen and I. R. McDonald. *Theory of simple liquids*. Academic Press: London, 1990. 161

[227] J. A. Barker and D. J. Henderson. *J. Chem. Phys.*, 47:2856, 1967. 162

[228] J. A. Barker and D. J. Henderson. *J. Chem. Phys.*, 47:4714, 1967.

[229] J. A. Barker and D. J. Henderson. *Rev. Mod. Phys.*, 48:587, 1976. 162

[230] T. Boublik. *J. Chem. Phys.*, 53:471, 1970. 162

[231] J. A. Barker and D. J. Henderson. *Rev. Mod. Phys.*, 54:1523, 1971. 162

[232] W. G. Chapman. *J. Chem. Phys.*, 93:4299, 1990. 162

[233] M. S. Wertheim. *J. Stat. Phys.*, 35:19, 1984. 163

[234] M. S. Wertheim. *J. Stat. Phys.*, 35:35, 1984.

[235] M. S. Wertheim. *J. Stat. Phys.*, 42:459, 1986.

[236] M. S. Wertheim. *J. Stat. Phys.*, 42:477, 1986. 163

[237] G. Jackson, W. G. Chapman, and K. E. Gubbins. *Mol. Phys.*, 65:1, 1988. 163

[238] W. G. Chapman, K. E. Gubbins, G. Jackson, and M. Radosz. *Ind. Eng. Chem. Res.*, 29:1709, 1990. 163

[239] W. G. Chapman, G. Jackson, and K. E. Gubbins. *Mol. Phys.*, 65:1057, 1988. 165

[240] E. Forte, F. Llovell, L. F. Vega, J. P. M. Trusler, and A. Galindo. *J. Chem. Phys.*, 134:154102, 2011. 166

[241] A. L. Archer, M. D. Amos, G. Jackson, and I. A. McLure. *Int. J. Thermophys.*, 17:201, 1996. 170

[242] R. Amin and T. N. Smith. *Fluid Phase Equilib.*, 142:231, 1998. 202, 232

[243] A. Firoozabadi and H. J. J. Ramey. *J. Can. Pet. Technol.*, 27:41, 1988. 202, 232

[244] K. A. G. Schmidt, G. K. Folas, and B. Kvamme. *Fluid Phase Equilib.*, 261:230, 2007. 202, 203, 214

[245] A. Ghoufi and P. Malfreyt. *Phys. Chem. Chem. Phys.*, 12:5203, 2010. 202, 217, 235

[246] D. B. MacLeod. *Trans. Faraday Soc.*, 19:38, 1923. 203

[247] C. F. Weinaug and D. L. Katz. *Ind. Eng. Chem.*, 35:239, 1943.

[248] C. Miqueu, J. Satherley, B. Mendiboure, J. Lachaise, and A. Graciaa. *Fluid Phase Equilib.*, 180:327, 2001. 203

[249] E. A. Guggenheim. *J. Chem. Phys.*, 13:253, 1945. 203

[250] Y. X. Zuo and E. H. Stenby. *Can. J. Chem. Eng.*, 75:1130, 1997. 203

[251] L. A. Girifalco and R. J. Good. *J. Phys. Chem.*, 61:904, 1957. 203

[252] F. M. Fowkes. *J. Phys. Chem.*, 66:1863, 1962.

[253] P. Winterfield, L. E. Scriven, and H. T. Davis. *AIChE J.*, 24:1010, 1978. 203

[254] S. Toxvaerd. *J. Chem. Phys.*, 57:4092, 1972. 204

[255] S. Nordholm and A. D. Haymet. *J. Aust. J. Chem.*, 33:2013, 1980. 204

[256] R. Evans. *Adv. Phys.*, 28:143, 1979.

[257] B. S. Almeida and M. M. Telo da Gama. *J. Phys. Chem.*, 93:4132, 1989.

[258] V. Bongiorno and H. T. Davis. *Phys. Rev. A*, 12:2213, 1975. 210

[259] F. J. Blas, E. M. Del Río, E. de Miguel, and G. Jackson. *Mol. Phys.*, 99:1851, 2001. 205

[260] G. J. Gloor, F. J. Blas, E. M. del Río, E. de Miguel, and G. Jackson. *Fluid Phase Equilib.*, 194:521, 2002.

[261] G. J. Gloor, G. Jackson, F. J. Blas, E. M. del Río, and E. de Miguel. *J. Chem. Phys.*, 121:12740, 2004.

[262] G. J. Gloor, G. Jackson, F. J. Blas, E. M. de lRío, and E. de Miguel. *J. Phys. Chem. C*, 111:15513, 2007. 204, 205

[263] J. S. Rowlinson. *J. Stat. Phys.*, 20:197, 1979. 204

[264] B. S. Carey, L. E. Scriven, and H. T. Davis. *AIChE J.*, 24:1076, 1978. 204

[265] B. S. Carey. *The gradient theory of fluid interfaces*. University of Minnesota: Mineapolis, 1979. 210, 213

[266] H. T. Davis and L. E. Scriven. *Adv. Chem. Phys.*, 49:357, 1982. 210

[267] A. H. Falls, L. E. Scriven, and H. T. Davis. *J. Chem. Phys.*, 78:7300, 1983.

[268] J. H. Pérez-Lopez, L. J. González-Ortiz, M. A. Leiva, and J. E. Puig. *AIChE J.*, 38:753, 1992.

[269] P. M. W. Cornelisse, C. J. Peters, and J. De Swaan Arons. *Fluid Phase Equilib.*, 82:119, 1993.

[270] P. M. W. Cornelisse, C. J. Peters, and J. De Swaan Arons. *Mol. Phys.*, 80:941, 1993. 204

[271] P. M. W. Cornelisse. *The squared gradient theory applied. Simultaneous modelling of interfacial tension and phase behaviour*. Delft University:Delft, 1997.

[272] M. Sahimi, H. T. Davis, and L. E. Scriven. *Soc. Pet. Eng. J.*, 4:234, 1985.

[273] Y. X. Zuo and E. H. Stenby. *Fluid Phase Equilib.*, 132:139, 1997.

[274] C. Miqueu, B. Mendiboure, A. Graciaa, and J. Lachaise. *Fluid Phase Equilib.*, 207:225, 2003. 211, 214

[275] D. Fu and Y. Wei. *Ind. Eng. Chem. Res.*, 47:4490, 2008.

[276] S. Liu, D. Fu, and J. Lu. *Ind. Eng. Chem. Res.*, 48:10734, 2009. 204

[277] M. I. Guerrero and H. T. Davis. *Ind. Eng. Chem. Fundam.*, 19:309, 1980. 204

[278] H. Kahl and S. Enders. *Fluid Phase Equilib.*, 172:27, 2000.

[279] H. Kahl and J. Winkelmann. *Fluid Phase Equilib.*, 270:50, 2008.

[280] O. G. Nino-Amezquita, S. Enders, P. T. Jaeger, and R. Eggers. *Ind. Eng. Chem. Res.*, 49:592, 2010. 204

[281] C. I. Poser and I. C. Sánchez. *J. Colloid Interface Sci.*, 69:539, 1979. 204

[282] G. T. Dee and B. B. Sauer. *J. Colloid Interface Sci.*, 152:85, 1992.

[283] B. B. Sauer and G. T. Dee. *J. Colloid Interface Sci.*, 162:25, 1994.

[284] H. S. Lee and W. H. Jo. *Polymer*, 39:2489, 1998. 204

[285] S. Fisk and B. Widom. *J. Chem. Phys.*, 50:3219, 1969. 204

[286] A. J. M. Yang, P. D. I. Fleming, and J. H. Gibbs. *J. Chem. Phys.*, 64:3732, 1976. 214

[287] M. K. Gupta and R. L. J. Robinson. *SPE Res. Eng.*, 11:528, 1987.

[288] M. Sahimi and B. N. Taylor. *J. Chem. Phys.*, 95:6749, 1991. 204

[289] S. Enders and K. Quitzsch. *Langmuir*, 14:4606, 1998. 204

[290] D. Dittmar, R. Eggers, H. Kahl, and S. Enders. *Chem. Eng. Sci.*, 57:355, 2002. 204

[291] T. Lafitte, D. Bessières, M. M. Piñeiro, and J. L. Daridon. *J. Chem. Phys.*, 124:024509, 2006. 204, 212, 213, 232

[292] V. Bongiorno, L. E. Scriven, and H. T. Davis. *J. Colloid Interface Sci.*, 57:462, 1976. 210, 211, 214

[293] H. T. Davis, L. E. Scriven, and B. S. Carey. *In Application of gradient theory to fluid interface.* DECHEMA: Frankfurt, 1980. 210

[294] B. F. McCoy and H. T. Davis. *Phys. Rev. A*, 20:1201, 1979. 211

[295] H. Y. Jr. Jennings and G. H. Newman. *Soc. Pet. Eng. J.*, 11:171, 1971. 214

[296] D. Chandler. *Nature*, 437:640, 2005. 217

[297] A. Mejía, J. C. Pàmies, D. Duque, H. Segura, and L. F. Vega. *J. Chem. Phys.*, 123:1, 2005. 218

[298] E. A. Müller and A. Mejía. *Fluid Phase Equilib.*, 282:68, 2009. 218

[299] E. Bertrand, H. Dobbs, D. Broseta, J. Indekeu, D. Bonn, and J. Meunier. *Phys. Rev. Lett.*, 85:1282, 2000. 220, 242

[300] F. Llovell, N. MacDowell, F. J. Blas, A. Galindo, and G. Jackson. *Fluid Phase Eq.*, 336:137, 2012. 232

[301] J. Hu, J. Chen, and J. Mi. *Ind. Eng. Chem. Res.*, 51:1236, 2012. 233

[302] J. M. Míguez, F. J. Blas, and M. M. Piñeiro. *J. Chem. Phys.*, 2013 (aceptado). 233, 241, 242

[303] L. C. Nielsen, I. C. Bourg, and G. Sposito. *Geochim. and Cosmochim. Acta*, 81:28, 2012. 234

[304] J.-C. Neyt, A. Wender, V. Lachet, and P. Malfreyt. *J. Phys. Chem. C*, 116(19):10563, 2012. 234

[305] F. J. Blas, A. I. Moreno-Ventas Bravo, J. M. Míguez, M. M. Piñeiro, and L. G. MacDowell. *J. Chem. Phys.*, 137:084706, 2012. 236

[306] B. Ni and A. Baumketner. *J. Mol. Model.*, 17:2883, 2011. 237

[307] E. Forte, A. Galindo, and J. P. M. Trusler. *J. Phys. Chem. B*, 115(49):14591, 2011. 237

[308] A. J. Haslam, A. Galindo, and G. Jackson. *Fluid Phase Equilib.*, 266:105, 2008. 242